Design of Sensors and Actuators for Totally Implantable Auditory Prostheses

by

Panagiota Kitsopoulos

A dissertation submitted in partial fulfillment
of the requirements for the degree of
Doctor of Philosophy
(Mechanical Engineering)
in The University of Michigan
2025

Doctoral Committee:

Professor Karl Grosh, Chair
Professor Kenn Oldham
Associate Professor Bogdan Popa
Clinical Associate Professor Emily Stucken
Associate Professor Serife Tol
Professor David Wentzloff

Panagiota Kitsopoulos
pkitsop@umich.edu
ORCID iD: 0000-0002-7540-1277

© Panagiota Kitsopoulos 2025

DEDICATION

To my family and friends who made all of this possible.

«Η Κρήτη δεν θέλει νοικοκυραίους, θέλει κουζουλούς.
Αυτοί οι κουζουλοί την κάνουν αθάνατη»
—Νίκος Καζαντζάκης

ACKNOWLEDGEMENTS

This work was supported by the Rackham Merit Fellowship (RMF) Program, the Hearing, Balance, and Chemical Senses institutional training grant (NIH T32 DC00011), and the NIH R01 DC021596 grant.

I could not have achieved what I have without the help, guidance, and support of certain individuals. First, I want to express my gratitude to my advisor, Prof. Karl Grosh, for his unwavering support and for engaging with my ideas, thoughts, and questions both in and out of the lab. I am also thankful to all my committee members. Dr. Emily Stucken - thank you for answering all my questions about the human ear anatomy, teaching me how to perform cadaveric temporal bone surgeries, and letting me attend a cochlear implant surgery (this was really cool!). Prof. Serife Tol, Prof. Bogdan Popa, Prof. Kenn Oldham, and Prof. David Wentzloff - thank you for all the knowledge you have imparted through your classes, lab conversations, meeting discussions, and overall constructive feedback. Your insights and expertise have been invaluable to my academic journey.

Second, I want to thank all the people, past and present, at 3626 G.G. Brown. Working from the office was an absolute delight because I got to be around, talk, and laugh with some of the best office mates one could hope for. I will never forget our office dinners and birthday celebrations. I would like to extend a special thanks to my labmate, Varun Goyal. From tracking down missing posters at train stations in Denmark, to comparing homework and lab notes, to simply venting about anything and everything, thank you for being a wonderful colleague and friend.

Third, I would also be remiss if I did not mention the remarkable people I met through the Mechanical Engineering Graduate Student Council. Especially, I want to thank Mihai

Cimpuieru, who has been such a great friend and who is always available to lend an ear. I also want to highlight Dr. Allison King, who motivated, inspired, supported, and uplifted me in more ways than one.

Fourth, I want to thank my friends from back home: Elissa, Elsa, Georgia, Grace, Jenny, and Katerina. Despite being thousands of miles apart, it feels as though no time has passed since we last saw each other. From celebrating weddings, to graduations, to just enjoying relaxing game nights over Zoom, I would not be where I am today without each of you.

I am also immensely grateful to my parents, Theo and Aria, for their constant love and support. Even when we were seven time zones apart, I always knew I could rely on you. To my sister, Flora, thank you for keeping me motivated and always pushing me to be the best version of myself.

Lastly, to my partner, Sachin, thank you for being the kindest, most supportive, and loving best friend one could ever wish for.

TABLE OF CONTENTS

DEDICATION ii

ACKNOWLEDGEMENTS iii

LIST OF FIGURES viii

LIST OF TABLES xi

LIST OF APPENDICES xii

LIST OF ACRONYMS xiii

LIST OF SYMBOLS xv

ABSTRACT xviii

CHAPTER

1 Introduction 1

1.1 The anatomy of the ear and hearing loss 1
1.1.1 Overview of the human ear 1
1.1.2 Sound transmission through the human ear 4
1.1.3 Hearing loss in humans 6
1.1.4 Loudness and sound perception 8
1.2 Hearing loss treatments and limitations 9
1.2.1 Hearing aids 9
1.2.2 Cochlear Implants 12
1.2.3 Commercial fully implantable auditory prostheses 16
1.2.4 Sensing mechanisms for totally implantable systems 19
1.3 Thesis overview and outline 20

2 Modeling of Piezoelectric MEMS Sensors 22

2.1 Equations of piezoelectricity 23
2.2 Piezoelectric output and combining layers 24
2.3 Multi-bandwidth accelerometer methods 24
2.3.1 Design constraints 24
2.3.2 Accelerometer design layout 25

2.3.3 Full analytical accelerometer model . . . 27
2.3.4 Assumed-mode solution to full analytical model . . . 32
2.3.5 Design optimization problem . . . 35
2.3.6 Design of multi-bandwidth accelerometers . . . 39
2.4 Results . . . 42
2.4.1 N-bandwidth designs with unconstrained proof mass thicknesses . . . 43
2.4.2 Four-bandwidth design with constrained proof mass thicknesses . . . 44
2.5 Discussion and conclusions . . . 47

3 Investigating the Effect of the Piezoelectric Thickness, Loss Tangent, and Piezoelectric Coefficient on Three Canonical MEMS Cantilever Sensors . 51

3.1 General optimization problem . . . 53
3.2 Sensor under uniform pressure . . . 55
3.2.1 Full analytical model . . . 55
3.2.2 Assumed-mode solution to full analytical model . . . 57
3.2.3 Casting the optimization problem . . . 60
3.2.4 Results . . . 61
3.3 Sensor with prescribed displacement . . . 62
3.3.1 Full analytical model . . . 63
3.3.2 Assumed-mode solution to full analytical model . . . 64
3.3.3 Casting the optimization problem . . . 66
3.3.4 Results . . . 67
3.4 Sensor with proof mass - accelerometer . . . 67
3.4.1 Casting the optimization problem . . . 68
3.4.2 Results . . . 69
3.5 Discussion and conclusions . . . 70

4 Modeling of the Middle Ear: Can a Middle Ear Speaker Amplify Sounds at the Stapes? . . . 74

4.1 Modeling and stability analysis . . . 74
4.1.1 Lumped parameter model . . . 75
4.1.2 Middle ear speaker: forcing, feedback, and stability . . . 77
4.2 Results . . . 80
4.2.1 Combined external and internal acoustic stimulation with no feedback and no time delay . . . 81
4.2.2 Stability and gain when the system includes feedback and time delay 83
4.3 Discussion and conclusions . . . 87

5 Conclusions, Contributions, and Future Work . . . 89

5.1 Conclusions . . . 89
5.2 Contributions . . . 92
5.3 Future work . . . 94

APPENDICES 95

BIBLIOGRAPHY 107

LIST OF FIGURES

FIGURE

1.1 Diagram of the human ear anatomy consisting of the outer, middle, and inner ear. The outer ear includes the pinna and the ear canal, bounded at the end by the eardrum. Sound waves are collected by the pinna and travel down the ear canal, causing the eardrum to vibrate. Vibrations are then transmitted to the middle ear, which includes the bones: malleus, incus, and stapes. The three bones amplify the vibrations and transmit them to the inner ear (cochlea) via the footplate of the stapes to the oval window. Not to scale. Figure credit to Brian Townsend. 3

1.2 Diagram of a cochlea cross-section. The scala vestibuli and scala tympani are filled with the fluid perilymph and are connected at the apex of the cochlea. The scala media is separated from the scala tympani by the basilar membrane. On the basilar membrane rests the organ of Corti, which contains the hair cells responsible for transforming sound vibrations into electrical signals. Not to scale. Figure adapted from Deo (2006). 4

1.3 Hearing threshold and 20-phon equal-loudness-level contour estimated or taken directly from BS ISO 226:2003. 8

1.4 Various styles of hearing aids. Figure credit to NIDCD and NIH Medical Arts Branch. 11

1.5 Cochlear implant components in a human ear. Figure credit to NIDCD and NIH Medical Arts Branch. 12

1.6 Cochlear implant surgery steps *©(2025)* Chris Gralapp, used with permission. See text for description of each step. 14

2.1 Example of an accelerometer comprised of one piezoelectric cantilever bimorph plate. (a) Top view, and (b) side view of the sensor assembly (cut plane shown in (a)). The design consists of two AlN layers (piezoelectric material) of length L, single piezoelectric layer thickness t_{piezo}, and width b. Three electrodes are on the bimorph's top, middle, and bottom. The proof mass sits flush against the plate and has length L_M, thickness t_M, width b, mass M, and moment of inertia I_M (Hake et al. (2021)). The entire device is mounted on a PCB that also holds the signal conditioning electronics to extract the output voltage, V_{out}, from the piezoelectric material. W_{bz} is defined as the prescribed base displacement in the z-direction, U_{bx} is defined as the prescribed base displacement in the x-direction, and θ_{by} is defined as the prescribed base rotation about the y-axis. The packaging of the device is not shown. Not to scale. Adapted from Hake et al. (2023). . . . 26

2.2 Example of a multi-bandwidth MEMS die layout with four sensing elements (top view). Each element has a piezoelectric bimorph plate and a proof mass, and each operates over a sub-bandwidth of the full operational bandwidth. 26
2.3 (a) Sensitivity of accelerometer with operational sub-bandwidth of 800 - 3150 Hz. The sensitivity is approximately constant until 3150 Hz, setting the upper frequency bound for this sensor (f_β). The resonance frequency, f_{res}, is 5828 Hz. (b) MDA_z curve of accelerometer plotted alongside 20-phon umbo acceleration values. The accelerometer meets the 20-phon noise floor at frequencies above 800 Hz, setting the lower frequency bound of this sensor (f_α). Here $L = 51$ µm, $L_M = 140$ µm, $t_M = 100$ µm, and $b = 128$ µm. 39
2.4 Discrete cross-over frequency values in Hz selected from the center frequencies of the 1/3 octave band. Cross-over values are labeled from f_2 to f_{19}. f_1 and f_{20} are the fixed lower and upper bounds of the first and last sensing element, respectively. $N_f^{\max} = 20$ in this case. 40
2.5 Overall MEMS dimensions of the unconstrained three-, four-, five-, and eight-bandwidth sensors in prototypical MEMS die layouts accounting for frame width and sensing element spacing using a 10:1 aspect ratio. The dimensions of the four-bandwidth sensor are given in Table 2.1 and the dimensions of the three-, five-, and eight-bandwidth sensors are given in the Appendix in Tables A.2, A.4, and A.5. 44
2.6 (a) Sensitivity response curves of constrained four-bandwidth design with four sensing elements (LFSE, MFSE_1, MFSE_2, and HFSE). (b) MDA_z curves for each sensing element calculated by converting spectral densities to acceleration levels with 1 Hz integration bandwidths. Shaded regions indicate sub-bandwidths of sensing elements. 46

3.1 Side view of a sensor comprised of one piezoelectric cantilever bimorph plate. The design consists of two AlN layers (piezoelectric material) of length L, single piezoelectric layer thickness t_{piezo}, and width b (into the page, not shown). Three electrodes are on the bimorph's top, middle, and bottom. The structure is subjected to either a uniform pressure, P (shown in pink), that extends over the full length of the cantilever, or a displacement, W_z (shown in blue), at the free end of the cantilever ($x = L$). In response to P or W_z, the piezoelectric layers will generate an output voltage, V_{out}. Not to scale. 55
3.2 Relationship between normalized A_S^{P} and t_{piezo} using varied and constant $\tan\delta$ and $\tilde{d}_{31}$. 62
3.3 Relationship between normalized A_S^{D} and t_{piezo} using varied and constant $\tan\delta$ and $\tilde{d}_{31}$. 68
3.4 Relationship between the normalized A_S^{AXL} and t_{piezo} for a bandwidth of 100 Hz – 20 kHz, using varied and constant $\tan\delta$ and $\tilde{d}_{31}$. 70
3.5 Relationship between normalized A_S^{AXL} and t_{piezo} for a bandwidth of 100 Hz – 1 kHz, using varied and constant $\tan\delta$ and $\tilde{d}_{31}$. 71

4.1 Lumped parameter model presented in Han et al. (2023) used to simulate the response of the human ear. Figure credit to Brian Townsend. 76

4.2 Model and experimental data (Gan et al., 2009; O'Connor and Puria, 2006; Aibara et al., 2001): (a) Normalized displacement of the stapes due to an external pressure incident on the tympanic membrane. (b) Phase of stapes. 80
4.3 Model and experimental data (O'Connor and Puria, 2006): (a) Normalized displacement of the stapes due to an internal pressure in the middle ear cavity. (b) Phase of stapes. 81
4.4 Model results: (a) Normalized displacement of the stapes due to an external, internal pressure, and variable γ^* (b) Phase of the stapes. We assume no feedback and no time delay. 82
4.5 Displacement ratio of the stapes. The numerator is the displacement due to an external and internal pressure with $\gamma^* = -1$. The denominator is the displacement only due to an external pressure. We assume no feedback and no time delay. 83
4.6 Eigenvalue solutions for various gains, with a time delay, $\tau = 10$ ms. The system is unstable for $\gamma^* \lesssim -4.6$. 84
4.7 Predicted displacement of the stapes normalized to the external pressure accounting for feedback and a time delay of $\tau = 10$ ms. 85
4.8 Comparing predicted displacements of the stapes normalized to the external pressure. The displacements with delays incorporate feedback, while those without delays assume no feedback. 86
4.9 Displacement ratio of the stapes. The numerator is the displacement due to an external and internal pressure with $\gamma^* = -1$. The denominator is the displacement only due to an external pressure. We assume there is feedback and a time delay of $\tau = 0.1$ ms. 86

A.1 Noise floor in dB SPL of four-bandwidth sensor with constrained proof mass thicknesses in comparison with the 20-phon equal-loudness-level contour from BS ISO 226:2003. 101
A.2 A-weighted noise floor in dBA of four-bandwidth sensor with constrained proof mass thicknesses in comparison with the 20-phon equal-loudness-level contour from BS ISO 226:2003, and with two Knowles® microphones (Knowles, 2025). . 101

B.1 Loss tangent, $\tan\delta$, as a function of t_{piezo}. 104
B.2 Piezoelectric coefficient, $|\tilde{d}_{31}|$, as a function of t_{piezo}. 105

LIST OF TABLES

TABLE

1.1 Levels of hearing loss severity (Salmon et al., 2023) 7

2.1 Four-bandwidth sensor dimensions with unconstrained proof mass thicknesses. The sensor area is 3.94×10^{-8} m^2, and the estimated MEMS die dimensions are 714 µm × 600 µm with a MEMS die area of 4.28×10^{-7} m^2. 44

2.2 Four-bandwidth sensor dimensions with constrained proof mass thicknesses. The sensor area is 5.60×10^{-8} m^2, and the estimated MEMS die dimensions are 825 µm × 575 µm with a MEMS die area of 4.74×10^{-7} m^2. 45

3.1 AlN material properties assuming a plane-strain constitutive hypothesis (Hake et al., 2023) 61

4.1 Lumped parameter model values used in Han et al. (2023) 77

A.1 Dual-bandwidth sensor dimensions with constrained proof mass thicknesses. The sensor area is 1.84×10^{-7} m^2, and the estimated MEMS die dimensions are 763 µm × 1,014 µm with a MEMS die area of 7.74×10^{-7} m^2. 98

A.2 Three-bandwidth sensor dimensions with unconstrained proof mass thicknesses. The sensor area is 7.19×10^{-8} m^2, and the estimated MEMS die dimensions are 691 µm × 645 µm with a MEMS die area of 4.46×10^{-7} m^2. 98

A.3 Three-bandwidth sensor dimensions with constrained proof mass thicknesses. The sensor area is 9.93×10^{-8} m^2, and the estimated MEMS die dimensions are 755 µm × 673 µm with a MEMS die area of 5.08×10^{-7} m^2. 99

A.4 Five-bandwidth sensor dimensions with unconstrained proof mass thicknesses. The sensor area is 3.28×10^{-8} m^2, and the estimated MEMS die dimensions are 742 µm × 582 µm with a MEMS die area of 4.32×10^{-7} m^2. 99

A.5 Eight-bandwidth sensor dimensions with unconstrained proof mass thicknesses. The sensor area is 2.55×10^{-8} m^2, and the estimated MEMS die dimensions are 783 µm × 607 µm with a MEMS die area of 4.75×10^{-7} m^2. 100

LIST OF APPENDICES

A Appendix for Chapter 1 . . . . . **95**

B Appendix for Chapter 2 . . . . . **104**

C Appendix for Chapter 3 . . . . . **106**

LIST OF ACRONYMS

AlN Aluminum Nitride

CI Cochlear Implant

dB Decibels

dBA Decibels A-Weighted

DRIE Deep Reactive Ion Etching

FDA Food and Drug Administration

FMT Floating Mass Transducer

HA Hearing Aid

HFSE High Frequency Sensing Element

HL Hearing Level

LFSE Low Frequency Sensing Element

LNF Lurie Nanofabrication Facility

MDA Minimum Detectable Acceleration

MDD Minimum Detectable Displacement

MDP Minimum Detectable Pressure

MEMS Microelectromechanical Systems

MF Magnification Factor

MFSE Middle Frequency Sensing Element

NIDCD National Institute on Deafness and Other Communication Disorders

NIH National Institutes of Health

PCB Printed Circuit Board

PLD Pulsed Laser Deposition

PVDF Polyvinylidene Difluoride

PZT Lead Zirconate Titanate

RC Resistor-Capacitor

RW Round Window

ScAlN Scandium-Doped Aluminum Nitride

SPL Sound Pressure Level

ST Stapes

TIAP Totally Implantable Auditory Prosthesis

TICI Totally Implantable Cochlear Implant

TM Tympanic Membrane

WHO World Health Organization

YLD Years Lived with Disability

ZnO Zinc Oxide

LIST OF SYMBOLS

A	Cross-section area of beam
$\boldsymbol{A_F}$	Force amplitude vector of lumped parameter model
A_M	Cross-section area of proof mass
A_{MEMS}^{tot}	Overall MEMS die area
A_S^{tot}	Total sensor area
A_S^{AXL}	Sensor area of accelerometer with a proof mass at the free end
A_S^{D}	Sensor area of sensor with a prescribed displacement at the free end
A_S^{P}	Sensor area of sensor under uniform pressure
A_{space}	Added area due to the frame width and spacing
A_{ST}	Surface area of the footplate of the stapes
A_{sur}^i	Surface area corresponding to each ith sensing element
A_{TM}	Surface area of tympanic membrane
$\boldsymbol{A_x}$	Displacement amplitude vector of lumped parameter model
b	Width of piezoelectric plate
C	Capacitance of piezoelectric layers
$[\overline{C}]$	Damping matrix of lumped parameter model
c_i	Damper in lumped parameter model where $i = 1 - 6$
$\boldsymbol{D}$	Electrical displacement vector
$[d]$	Piezoelectric coefficient matrix
$\tilde{d}_{31}$	Piezoelectric coefficient assuming a plane-strain constitutive hypothesis
$\boldsymbol{E}$	Electrical field vector

$\overline{EI}$	Beam bending stiffness
$\mathbf{F}$	Force vector of lumped parameter model
f_α	Lower frequency bound
f_β	Upper frequency bound
$f_{3\text{dB}}$	Frequency at which there is a 3 dB change
f_{res}	Resonant frequency
I_M	Moment of inertia of proof mass
$[\overline{K}]$	Spring matrix of lumped parameter model
k_i	Spring in lumped parameter model where $i = 1 - 6$
k_B	Boltzmann constant
L	Length of piezoelectric plate
L_M	Length of proof mass
M	Mass of proof mass
$[\overline{M}]$	Mass matrix of lumped parameter model
m_i	Mass in lumped parameter model where $i = 1 - 6$
M_e	Electrical moment
m_{L_M}	Number of values of L_M
m_{t_M}	Number of values of t_M
N	Number of sensing elements in a design
n	Number of MFSEs in a design
$N_f^{\max}$	Maximum number of frequencies in the design space
P_E	External pressure
P_I	Internal pressure
Q	Q factor
Q^c	Charge generated due to the piezoelectric layers
$S(f)$	Sensitivity as a function of frequency
$[s^E]$	Piezoelectric elastic compliance matrix measured under a constant electric field

$\tilde{s}_{11}^{E}$	Piezoelectric elastic compliance measured under a constant electric field assuming a plane-strain constitutive hypothesis
$\boldsymbol{T}$	Mechanical stress vector
T^{*}	Temperature in Kelvin
$\tan\delta$	Loss tangent of piezoelectric material
t_M	Thickness of proof mass
t_{piezo}	Single piezoelectric layer thickness
U_{bx}	Prescribed base displacement in the x-direction
$\overline{v_n^2}$	Sensor noise spectral density
V_{out}	Output voltage
W_{bz}	Prescribed base displacement in the z-direction
$\boldsymbol{x}$	Displacement vector of lumped parameter model
Z	Impedance
γ^{*}	Feedback gain of implanted receiver
$\boldsymbol{\varepsilon}$	Total strain vector
ϵ_{33}^{S}	Piezoelectric relative permittivity measured under zero strain
$[\epsilon^{T}]$	Piezoelectric permittivity matrix measured under constant stress
$\tilde{\epsilon}_{33}^{T}$	Piezoelectric permittivity measured under constant stress assuming a plane-strain constitutive hypothesis
θ_{by}	Prescribed base rotation about the y-axis
ρ_{AlN}	Density of AlN
ρ_M	Density of proof mass
ω	Radian frequency

ABSTRACT

Hearing loss is a debilitating condition that affects over 5% of the world's population. Hearing aids and cochlear implants help patients treat their hearing loss, but have limitations impacting their use rates. Totally implantable auditory prostheses would expand the range of activities a prosthesis user could engage in and enable 24/7 use. However, the lack of a completely implantable microphone that is robust, lightweight, and low-noise prevents the widespread adoption of completely implantable auditory prostheses. Current implantable sensors struggle to meet or exceed the performance necessary for this application. Moreover, three active middle ear implants have been developed to address some of the barriers associated with conventional hearing aids. However, all devices rely on transducers mechanically attached to a middle ear structure to deliver amplified stimuli, with no other alternative options. In this work, we aim to provide solutions that help bridge these gaps.

First, we developed a discretized and exhaustive design optimization approach to identify multi-bandwidth transducers that meet the 20-phon noise floor over 100 Hz – 8 kHz, and can replace the external microphones in implantable prostheses. Our design procedure is based on an experimentally validated analytical model that simulates the response of miniature piezoelectric microelectromechanical systems (MEMS) accelerometers. A four-bandwidth accelerometer with constrained proof mass thicknesses is selected as the design that best balances area minimization with ease of manufacturability. The estimated MEMS die dimensions are 825 µm × 575 µm, which is a 23% MEMS die area reduction compared to the previously published dual-bandwidth sensor.

Second, we investigated the effect of the piezoelectric thickness, loss tangent, and piezoelectric coefficient on the sensor area of three canonical sensor designs: a sensor under uniform pressure, a sensor with a prescribed displacement at the free end, and an accelerometer with a proof mass. All three sensor designs have been or are currently used in research for totally implantable auditory prostheses. This study identified the direct relationships between the sensor areas and the piezoelectric thickness. These relationships can be used to predict the sensor area given a particular piezoelectric thickness, noise floor, and operational bandwidth. Specifically, assuming the material properties vary with thickness, the sensor area for a sensor under uniform pressure remains approximately constant regardless of the thickness. In contrast, the sensor areas for a sensor with a prescribed displacement and for an accelerometer decrease with an increasing thickness. However, these results depend on the material properties, and, for the accelerometer design, also on the operational bandwidth.

Lastly, we carried out a new analysis where we investigated the feasibility of using an implanted middle ear speaker to amplify the motion of the stapes. We identified that an implanted middle ear speaker with a negative gain and small time delays can be used to provide amplification at the stapes. Specifically, at high frequencies (> 1 kHz), with a gain of -1, and no feedback or time delays, the amplification can be up to six times compared to the motion of the stapes with no middle ear speaker. Even greater amplification can be achieved with more negative gains. However, accounting for a time delay of 10 ms, we identified that for gains less than -4.5, the system can become unstable. In addition, high time delays introduce oscillations in the displacement of the stapes, but low time delays can significantly reduce this effect.

CHAPTER 1

Introduction

Hearing plays a crucial role in our daily lives. Although it is not essential for participating in society, it can help us communicate with others and recognize potential dangers. When acoustic signals reach our ears, they are converted to structural vibrations and then to electrical signals within the brain. Hearing loss disrupts this auditory pathway, and various intervention options are needed to restore hearing capacity.

In this introduction, we review the anatomy of the ear and how hearing loss impacts it. We explore how hearing loss is defined and measured and discuss commercially available solutions, highlighting their shortcomings that underscore the need for totally implantable hearing systems. Lastly, we present research on various sensing mechanisms and our approach to providing a solution.

1.1 The anatomy of the ear and hearing loss

1.1.1 Overview of the human ear

Figure 1.1 displays the anatomy of the human ear, which is comprised of three functionally related compartments: the outer, middle, and inner ear. The outer ear consists of the pinna and the external auditory canal or ear canal (Kanegaonkar and Whittaker, 2015). The pinna consists of an elastic cartilage over which the skin is tightly adherent, and while relatively immobile, it can, to some extent, assist in distinguishing noises originating in front or behind

the head while providing other types of filtering (Yost, 2000). The ear canal is covered by skin that secretes cerumen, also known as earwax. The lateral (toward the pinna) third of the ear canal consists of cartilage, whereas the rest is bony (Yost, 2000). It has hairs on its surface and is approximately 2.5 cm in length (Møller, 2006; Kanegaonkar and Whittaker, 2015). As the resonance of the ear canal is about 2.5 kHz, and the resonance of the concha, a portion of the pinna, is closer to 5 kHz, the outer ear causes a natural amplification of incoming sounds of 10 to 15 dB between 1.5 to 7 kHz (Yost, 2000). The ear canal is bounded by the tympanic membrane or eardrum at one end, separating the outer from the middle ear (Kanegaonkar and Whittaker, 2015). Sound waves collected by the pinna travel down the ear canal and vibrate the eardrum. The eardrum is a cone-shaped, slightly oval, thin membrane with the apex pointed inward, towards the middle ear cavity (Møller, 2006). The complicated vibratory pattern of the eardrum allows for an efficient transfer of acoustic stimuli between the outer and middle ear (Yost, 2000).

The middle ear cavity is filled with air and opens only to the external environment through the Eustachian tube, which connects to the pharynx (Kanegaonkar and Whittaker, 2015; Møller, 2006). The middle ear function depends on keeping the air pressure within the middle ear cavity close to ambient pressure. This is accomplished by briefly opening the Eustachian tube. Furthermore, the Eustachian tube decreases the transmission of a person's voice within the cavity (Møller, 2006). The middle ear bones comprise the ossicular chain and include the malleus, incus, and stapes. They are suspended within the middle ear cavity by several ligaments and muscles (Yost, 2000). The manubrium of the malleus is embedded in the eardrum, with the tip of the manubrium (umbo) located at the apex of the eardrum. The head of the malleus is connected to the incus in a double saddle joint, which is regarded as rigid (Møller, 2006). The long process of the incus projects downward, bends toward the inner ear, and joins with the stapes. The stapes is the smallest bone and consists of a head, two bony struts, and a flat oval bone called the footplate. The footplate contacts the oval window, a part of the inner ear (Yost, 2000). For reference, the length and weight of the

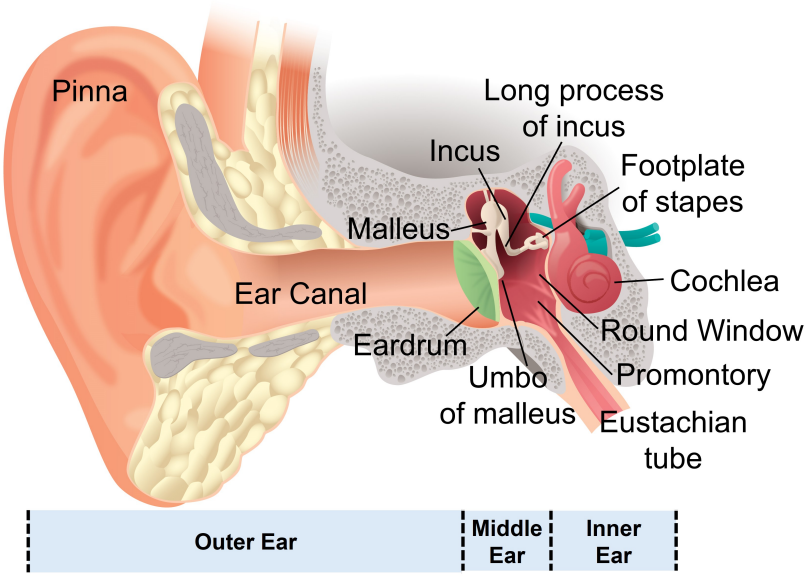

Figure 1.1: Diagram of the human ear anatomy consisting of the outer, middle, and inner ear. The outer ear includes the pinna and the ear canal, bounded at the end by the eardrum. Sound waves are collected by the pinna and travel down the ear canal, causing the eardrum to vibrate. Vibrations are then transmitted to the middle ear, which includes the bones: malleus, incus, and stapes. The three bones amplify the vibrations and transmit them to the inner ear (cochlea) via the footplate of the stapes to the oval window. Not to scale. Figure credit to Brian Townsend.

three middle ear ossicles are: malleus: 8 mm and 23–35 mg, incus: 6 mm and 25–39 mg, and stapes: 3 mm and 2–4 mg (Noussios et al., 2016; Zhao et al., 2009; Chen et al., 2008; Sim and Puria, 2008).

The inner ear consists of two functional units: the vestibular apparatus, consisting of the vestibule and semicircular canals, and the snail-shaped cochlea, which contains the sensory organ of hearing (organ of Corti). The vestibular apparatus is primarily involved in the sense of balance. The cochlea is separated into three distinct chambers, as shown in Fig. 1.2. These chambers include the scala vestibuli and scala tympani, filled with the fluid perilymph and connected at the apex of the cochlea, and the scala media, filled with the fluid endolymph. The base of the scala media comprises the basilar membrane (which separates the scala media from the scala tympani). Resting on the basilar membrane is the organ of Corti, which contains the hair cells that generate nerve signals in response to sound vibrations. The

vibrating motion of the footplate on the oval window creates a coupled pressure wave that propagates through the perilymph of the scala vestibuli toward the apex of the cochlea, then to the scala tympani, and eventually reaches the round window. This motion simultaneously vibrates the basilar membrane, causing the organ of Corti to move, stimulating the hair cells, and generating nerve impulses to the brain. It is also important to note that the round and oval windows lead to the inner ear on opposite sides of the basilar membrane; i.e., positive pressure on each window would move the basilar membrane in opposite directions (Yost, 2000; Kanegaonkar and Whittaker, 2015; Hawkins, 2024).

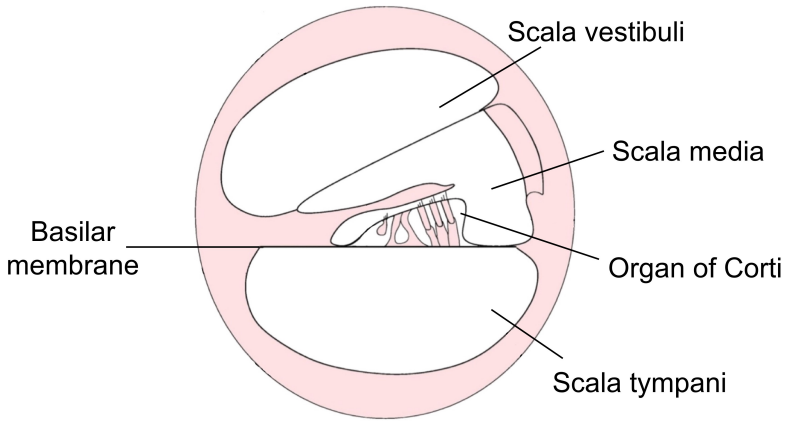

Figure 1.2: Diagram of a cochlea cross-section. The scala vestibuli and scala tympani are filled with the fluid perilymph and are connected at the apex of the cochlea. The scala media is separated from the scala tympani by the basilar membrane. On the basilar membrane rests the organ of Corti, which contains the hair cells responsible for transforming sound vibrations into electrical signals. Not to scale. Figure adapted from Deo (2006).

1.1.2 Sound transmission through the human ear

Once acoustic stimuli reach the outer ear, they are transmitted through the middle ear to the inner ear via three methods: bone conduction, air conduction in the middle ear cavity, and ossicular chain conduction, with the latter method being the most effective. Bone conduction, primarily of the temporal bone, may occur, but it is not an important part of the normal auditory function due to the high impedance mismatch between air (sound waves) and bone. However, applying a direct vibrating unit to the skull can directly stimulate the inner

ear (Yost, 2000). For reference, it is reported in the literature that occluding the cartilaginous part of the ear canal, which prevents some acoustic waves from reaching the eardrum via air conduction, leads to a hearing loss of approximately 37.5 to 48 dB. In contrast, occluding the bony part of the ear canal leads to a hearing loss of 21 to 24.95 dB (Narayanan et al., 2019). This is consistent with the earplug noise reduction rating of approximately 32 dB. In addition, lab measurements with bone conduction stimuli have shown a 10-15 dB sound pressure decrease in the ear canal when the cartilage is removed. This supports the belief that the vibration of the cartilage causes most of the bone conduction in the ear canal. When occluding the ear canal, any sound pressures caused by bone conduction are elevated below 1 kHz. This is commonly experienced as a low-frequency emphasis of one's own voice (Stenfelt and Goode, 2005).

Air conduction in the middle ear cavity is inefficient in moving the fluid in the inner ear, as fluid has a higher impedance than air. Due to this impedance mismatch, more pressure would be required to propagate acoustic stimuli in the inner ear fluid. Furthermore, due to the opposite vibratory directions of the oval and round windows, moving them simultaneously, as in the case of air conduction, would lead to a very inefficient system where the basilar membrane would move less. A possible hearing loss of 60 dB has been found in patients with no ossicles, where only air conduction in the middle ear cavity was possible (Yost, 2000). The ossicular chain has compensated for the air-to-fluid impedance mismatch through the size difference between the areas of the eardrum and the footplate of the stapes (Yost, 2000). In humans, the tympanic-membrane-to-footplate area ratio is about 21 (Wever and Lawrence, 1954) to 26 (Békésy, 1960). This area difference increases the pressure exerted on the footplate. The transfer of pressure from the eardrum to the footplate is further increased by the movement of the ossicles, which act as levers to amplify the transmitted vibrations (Yost, 2000). All of these contributions can lead to a mean gain of about 20 dB in the 500 Hz to 2 kHz range (Aibara et al., 2001; Puria et al., 1997).

1.1.3 Hearing loss in humans

According to the World Health Organization (WHO) (2024), hearing loss is a disabling condition that affects over 5% of the world's population. It not only hampers communication and speech (Cunningham and Tucci, 2017) but it is also linked to other health conditions, including social isolation (WHO, 2024), loneliness (Nachtegaal et al., 2011), stigmatization (Cunningham and Tucci, 2017), depression (Li et al., 2014), cognitive decline (Lin et al., 2013), and dementia (Livingston et al., 2017). Hearing loss is so prevalent that it is ranked as the third-largest contributor to global years lived with a disability (YLD) and designated as the primary cause of YLDs for adults over 70 (Haile et al., 2021).

There are three types of hearing loss: conductive, sensorineural, and mixed, which is a combination of the two (Johns Hopkins Medicine, 2025; Cleveland Clinic, 2023). Conductive hearing loss is the most common cause of hearing loss in young children, and it occurs when sound waves cannot be transmitted to the inner ear due to disruptions in the outer or middle ear. For instance, the ear canal may be blocked by earwax or a foreign object, or the middle ear may be impacted by fluid or infection (Cleveland Clinic, 2024). Sensorineural hearing loss occurs when the hair cells in the cochlea are damaged and typically develops over a prolonged period. This is the most common type of hearing loss in adults and can be caused by aging, exposure to loud noise, head injury, illness, certain drug side effects, or a hereditary condition. Rarely, sensorineural hearing loss may occur very suddenly, known as sudden sensorineural hearing loss or sudden deafness (Johns Hopkins Medicine, 2025; Cleveland Clinic, 2023).

To diagnose and distinguish between conductive and sensorineural hearing loss, a complete audiometric evaluation is performed, including tests such as tuning fork exams and pure-tone audiograms (Tanna et al., 2023; Cleveland Clinic, 2023). The pure-tone audiograms also assess the hearing threshold in patients for air and bone conduction. They are performed in sound-treated rooms to eliminate ambient noise. Air conduction tones are presented through headphones, and bone conduction tones are presented through an oscillating transducer

placed on the mastoid process behind the pinna (Salmon et al., 2023). Although normal human hearing ranges from 20-20,000 Hz (Yost, 2000), a typical audiogram only measures thresholds at 250-8000 Hz (Tanna et al., 2023; Salmon et al., 2023). This range is chosen because it encompasses the primary human speech frequencies (approx. 500-4000 Hz (Walker et al., 2013)). The results of the pure-tone audiogram test are plotted on an audiogram displaying the quietest sound at a given frequency that a patient can discern at least 50% of the time, and it is measured in decibels Hearing Level (dB HL). Hearing Level is a scale based on normal human hearing thresholds, where 0 dB HL is the loudness at which most people can perceive a sound at a particular frequency 50% of the time. If an individual has better hearing than the average, then their threshold would be lower than 0 dB HL. Although variability across the population is expected, hearing thresholds up to 25 dB HL are considered normal. However, it is also important to note that differences in the exam equipment may add to the variability, and thus, a change in the hearing threshold of 5 dB HL is considered within the standard error of these measurements. Based on the audiogram results, hearing loss is classified by severity (Table 1.1) and frequency (Salmon et al., 2023; Yost, 2000).

Table 1.1: Levels of hearing loss severity (Salmon et al., 2023)

Hearing Range	**dB HL**
Normal	-10 to 25
Mild	26 to 40
Moderate	41 to 55
Moderately Severe	56 to 70
Severe	71 to 90
Profound	91+

The work presented in this thesis will primarily focus on sensorineural hearing loss, which will be referred to as hearing loss throughout the document.

1.1.4 Loudness and sound perception

The human ear is sensitive not only to the intensity of sounds (dB SPL) but also to frequency. Figure 1.3 shows two equal-loudness-level contours: the hearing threshold and the 20 phon. These contours show the intensity level required at a particular frequency for a comparison tone to be perceived as equally loud as the standard tone by a listener. The standard tone is measured at 1 kHz for various intensity levels. For instance, in the 20-phon contour, the standard tone is 20 dB SPL at 1 kHz, and a comparison tone presented at 100 Hz with 48.4 dB SPL is perceived as loud as the standard tone (BS ISO 226:2003; Yost, 2000). It is important to note that the 20-phon level is approximately 20 dB greater than the hearing threshold across most of the frequency range. Thus, since hearing loss is measured relative to normal hearing, restoring sound perception to the 20-phon level could enable a patient with moderate to profound hearing loss to attain normal hearing ability or experience only mild hearing loss.

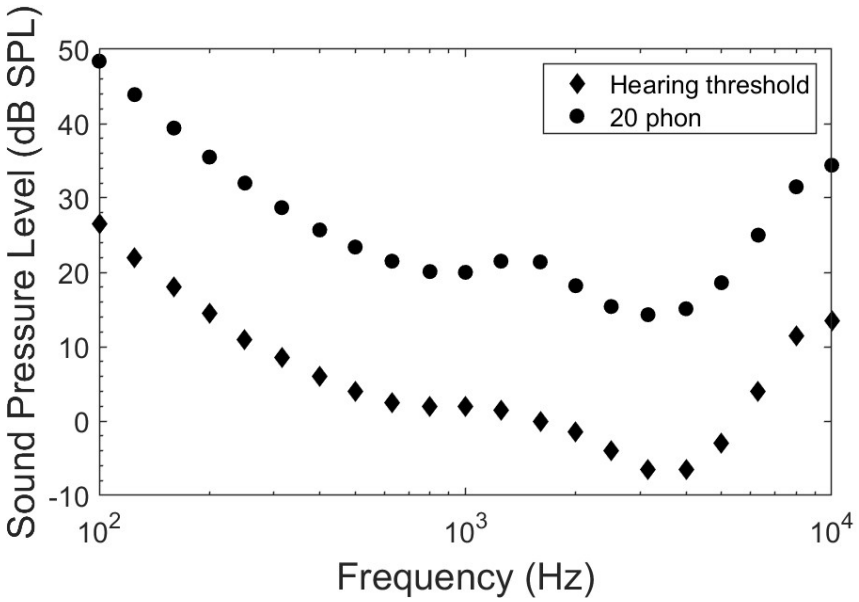

Figure 1.3: Hearing threshold and 20-phon equal-loudness-level contour estimated or taken directly from BS ISO 226:2003.

1.2 Hearing loss treatments and limitations

Hearing prostheses such as hearing aids (HAs) and cochlear implants (CIs) are effective in treating patients with permanent hearing loss (Cunningham and Tucci, 2017). HAs are small electronic devices worn in or behind the outer ear. They are used to amplify incoming sounds and help users primarily with mild to moderate hearing loss (NIDCD, 2022). CIs are small and complex electronic devices that use both external and implanted components, helping users with profound deafness (NIDCD, 2024a). Even though patients using these devices report improved speech perception (Holder et al., 2022; Alhabib et al., 2021), social and psychological functioning (Cunningham and Tucci, 2017), and quality of life (Ferguson et al., 2017), there are longstanding challenges that hinder their adoption. These challenges include but are not limited to perceived ineffectiveness, ongoing maintenance costs, lack of comfort, and cosmetic appearance (The National Academies, 2016; Banakis Hartl and Jenkins, 2020). Moreover, HA and CI users express the inconvenience of the devices' externally worn and detachable parts (e.g., microphones) that limit the range of activities they can partake in while using them, make them self-conscious of their disability, and can easily be lost, damaged, or stolen (Babajanian et al., 2024; Calero et al., 2018); a totally implantable auditory prosthesis (TIAP) would significantly ameliorate these issues. While implantable HAs and CIs have been developed, these devices have not been widely adopted (Banakis Hartl and Jenkins, 2020; Babajanian et al., 2024). The most significant obstacle to the wide adoption of TIAPs has been the development of an implantable low-noise sensor (Trudel and Morris, 2022; Babajanian et al., 2024). Without it, a TIAP is not possible.

1.2.1 Hearing aids

Conventional HAs are non-invasive, i.e., they require no surgery, and can be placed behind the pinna, in the ear canal (acoustic HAs), or anchored to the skull (bone conduction HAs) (Schuster-Bruce and Gosnell, 2022; Stenfelt, 2006). Some of the most commonly used

HAs consist of three main components: a microphone, an amplifier, and a speaker/receiver (NIDCD, 2022). The microphone collects the external acoustic stimuli and converts them to electrical signals, which are amplified by the amplifier (Schuster-Bruce and Gosnell, 2022; NIDCD, 2022). The speaker receives the amplified signals and converts them back to acoustic energy by projecting the sound into the ear canal, thereby vibrating the eardrum (Schuster-Bruce and Gosnell, 2022).

Various HAs exist, as there is no "one-size fits all" (Schuster-Bruce and Gosnell, 2022). Figure 1.4 shows the various styles for some of the most commonly used HAs. These styles differ by size, placement, and the degree to which they can amplify sound. Behind-the-ear HAs are worn by people of all ages with mild to profound hearing loss, and include a hard plastic case that holds the electronic parts and sits behind the ear. The case is connected through a plastic tube to a plastic earmold that fits inside the outer ear. The amplified sound is transmitted to the ear canal through the earmold (NIDCD, 2022). These HAs are robust, cheap, and easy for patients with reduced dexterity (Schuster-Bruce and Gosnell, 2022). The Mini behind-the-ear HA is open-fit, where the receiver, a narrow tube, is inserted into the ear canal. This open-ear-canal fit prevents users from perceiving their voice as plugged up, and it is also beneficial for people with excessive earwax buildup. In-the-ear HAs are used for mild to severe hearing loss, but they are not usually used in young children because the casings would need to be replaced often as the outer ear grows. The entire device casing with all electronic components is made of hard plastic and fits completely inside the outer ear (NIDCD, 2022). These HAs are more discreet and provide an improved aesthetic advantage (Schuster-Bruce and Gosnell, 2022). Canal HAs are used for mild to moderately severe hearing loss and fit into the ear canal. Due to their small size, they are less suitable for people with reduced dexterity, as they may be difficult to adjust and remove. Furthermore, they are not recommended for people with severe to profound hearing loss because their reduced size limits the power and amplifying volume (NIDCD, 2022).

Lastly, it is important to reflect on the statistics associated with the adoption of HAs.

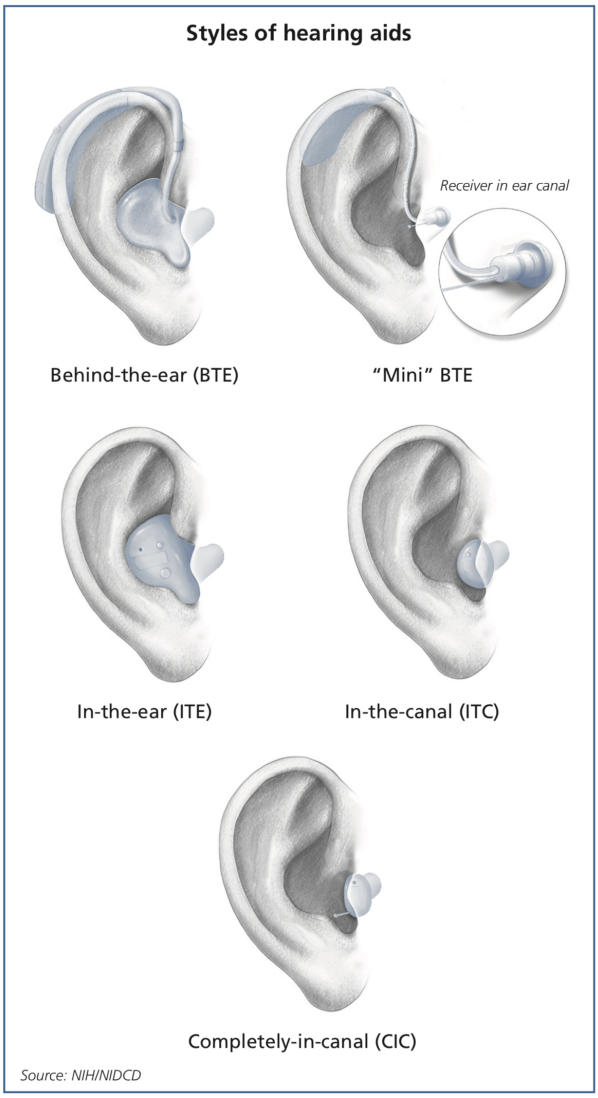

Figure 1.4: Various styles of hearing aids. Figure credit to NIDCD and NIH Medical Arts Branch (NIDCD, 2022).

About 28.8 million adults in the United States could benefit from using HAs but only one out of five people actually use one, and fewer than one out of three adults over 70 have ever used one (NIDCD, 2024b). These numbers help us reflect on the shortcomings of current HA technology and underscore the potential impact that totally implantable hearing prostheses may have on improving these adoption rates.

1.2.2 Cochlear Implants

Unlike HAs, CIs do not amplify sounds; they instead entirely bypass the damaged inner ear and directly stimulate the auditory nerve (NIDCD, 2024a). Figure 1.5 shows the external and internal components of a CI, of which the latter require surgical implantation. The external components include a microphone, a speech processor, and a transmitter, and the internal components include a receiver/stimulator and an electrode array positioned in the cochlea in the scala tympani. The microphone collects the acoustic stimuli and sends this information to the sound processor, which in turn converts it from mechanical vibrations to electrical signals. The transmitter sends these signals through the skin via radio frequency to the implanted receiver/stimulator, aligned together by a magnet. The receiver/stimulator transmits the electrical signals to the electrode array, stimulating different regions of the auditory nerve (Sutton, 2025; NIDCD, 2024a).

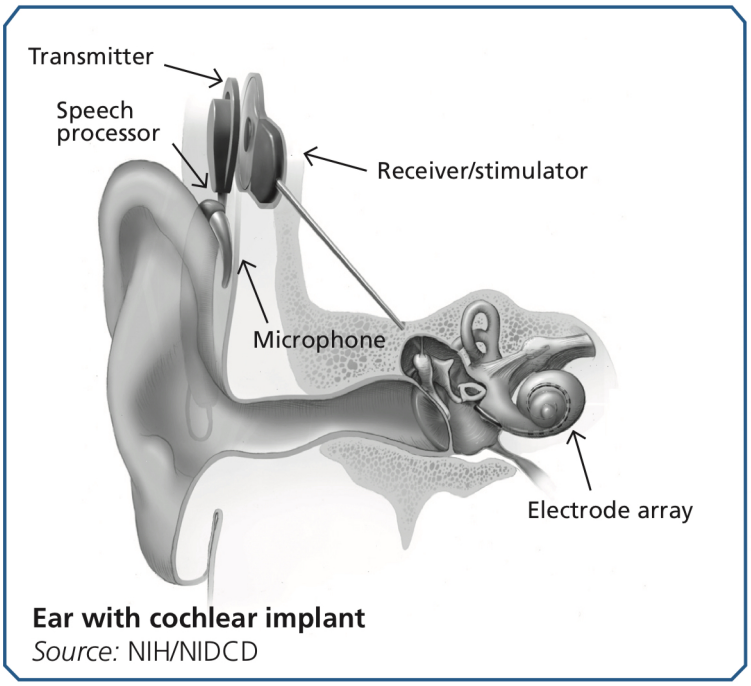

Figure 1.5: Cochlear implant components in a human ear. Figure credit to NIDCD and NIH Medical Arts Branch (NIDCD, 2024a).

Surgery is required to implant the internal components of a CI. A simplified description is provided here. The first step in a typical CI surgery is a skin incision on top of the mastoid bone behind the pinna (Fig. 1.6a). A subperiosteal pocket (under the fibrous sheath of the skull bone) is then created to house the receiver/stimulator (Fig. 1.6b). For some implants, a well may need to be drilled out with a template provided by the implant supplier. The second step is a mastoidectomy, which involves removing the mastoid air cells from the mastoid bone (Sanna et al., 2016). During this step, it is necessary to open the aditus ad antrum to reveal the short process of the incus (Sanna et al., 2012b). The short process is one of the standard landmarks used to identify the location of the facial nerve (Cohen and Roland, 2006; Sanna et al., 2016). The third step is a posterior tympanotomy (facial recess approach), which involves further drilling into the mastoid to create a small opening into the middle ear space. This opening is restricted by the position of the facial nerve and the chorda tympani nerve (Cohen and Roland, 2006; Sanna et al., 2012a). The posterior tympanotomy allows access to the cochlea and the round window (Fig. 1.6c) (Sanna et al., 2016, 2012a). The round window may be covered by a mucosal layer, which is removed (Fig. 1.6d). The round window membrane is opened using a small hooked instrument, with care taken not to open the superior region as the basilar membrane is situated immediately behind. The round window approach gives safe and easy access to the scala tympani and allows for a chance of saving any residual hearing. Just before the actual insertion of the electrode array into the cochlea, the receiver/stimulator is placed in its pocket or well. The electrodes are introduced slowly using the correct insertion angle through the round window in order to avoid intracochlear trauma or misplacement (Fig. 1.6e). A cochleostomy (a drilled opening created inferiorly to the round window) may be used to insert the electrodes instead, depending on the surgeon's preference and anatomical restrictions (Fig. 1.6f). Once implantation is complete, the electrode array is fixated using small pieces of muscle or fascia (thin tissue from temporal muscle) (Fig. 1.6g), and the skin layers from the incision behind the pinna are closed (Sanna et al., 2016).

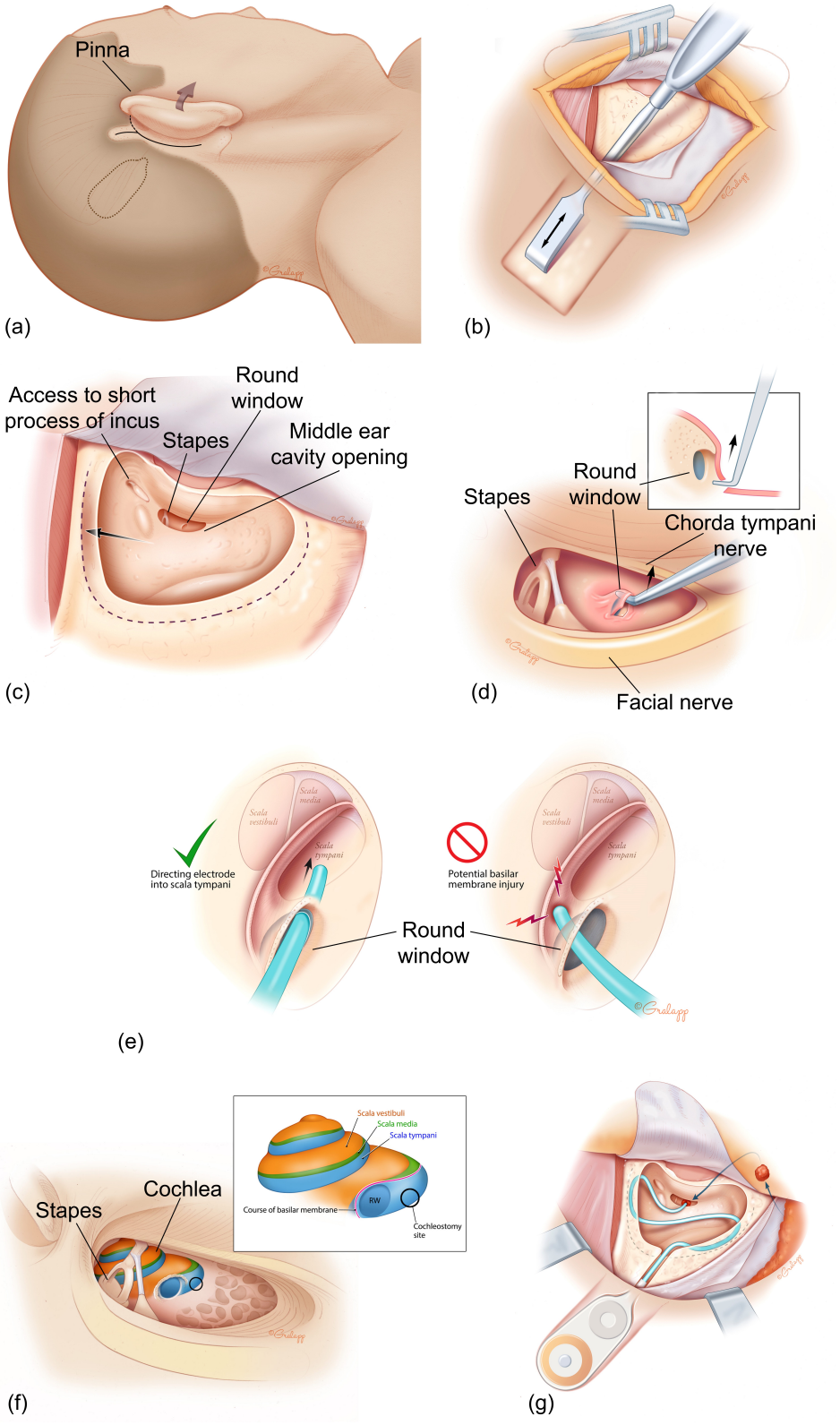

Figure 1.6: Cochlear implant surgery steps *©(2025)* Chris Gralapp, used with permission. See text for description of each step.

CIs do not restore normal hearing, but they allow people with profound deafness to receive useful representations of sounds (NIDCD, 2024a). Furthermore, CI users need time to learn to listen via electrical stimulation and require consistent use even after reaching a plateau in performance 6-12 months following implantation. Studies have found that consistent use of the external processor yields significant improvements in speech recognition (Holder and Gifford, 2021), and without it, the surgically implanted components are rendered useless. The clinical recommendations are to use the processor "all day" or "during all waking hours". However, data logging in CI software suggests that adult users are wearing their devices much less, with an average of 10 hours per day. In a questionnaire study, 100 CI users were asked about their experience with CIs. Among some of the results included that 37% of users simply forgot to use their CI, and 87% removed the external processor while exercising or working outside during the summer (Holder et al., 2022).

Lastly, let's once again reflect on the statistics associated with the adoption of CIs. Nassiri et al. (2022), using data from 2015, estimated the CI adoption rates in the United States. They used the total number of CI recipients as the numerator and an estimate of the total population of individuals who may benefit from CIs as the denominator; the latter was estimated using both traditional and expanded audiometric criteria. The study identified that a total of 170,252 U.S. adult and pediatric patients underwent cochlear implantation, while the number of traditional audiometric CI candidates totaled 1,337,144, resulting in a 12.7% adoption rate. Using the broadened audiometric criteria to include patients with single-sided deafness and asymmetrical hearing loss expanded the potential CI candidate population to approximately 8.05 million individuals, resulting in a 2.1% adoption rate. As of December 2019, the estimation for U.S. adult and pediatric CI recipients has increased to 183,100 (NIDCD, 2024b). These numbers show that CI adoption remains low and highlight the need to address some barriers associated with these low adoption rates, such as the external components.

1.2.3 Commercial fully implantable auditory prostheses

Several factors have been identified as barriers to HA and CI adoption rates, including the use of external components (Babajanian et al., 2024; Calero et al., 2018). Eliminating these components has the potential to address many issues associated with them, including offering protection against external factors like wind noise, earwax blockage, and water exposure. It would also improve the convenience for the user, who would no longer need to remember to wear the device or remove it for protection during activities such as sleep. In addition, an implanted middle ear sensor would automatically provide middle ear gain and pinna directionality cues, thereby enhancing acoustic performance over an external microphone (Denk et al., 2018). Due to these and many more advantages, some fully implantable auditory prostheses have already been developed and commercialized (Babajanian et al., 2024; Banakis Hartl and Jenkins, 2020).

To address some of the barriers associated with conventional HAs, middle ear implants have been introduced to the market. The primary devices that have received approval from the U.S. Food and Drug Administration (FDA) include the Med-El Vibrant SoundBridge, the Ototronix MAXUM system, and the Envoy Esteem (Babajanian et al., 2024; Banakis Hartl and Jenkins, 2020; Mankekar, 2014). The Med-El Vibrant SoundBridge is a semi-implantable device that utilizes a floating mass transducer (FMT) coupled to the incus (short or long process), stapes, round window, or oval window. The FMT converts electrical signals to mechanical vibrations, directly vibrating the anatomical feature it is coupled to (Labassi et al., 2017; Graf et al., 2022). However, the device relies on an external microphone and sound processor (Banakis Hartl and Jenkins, 2020; Labassi et al., 2017). The Ototronix MAXUM system is another semi-implantable device that uses an implanted magnet attached to the incudostapedial joint, mechanically vibrating it (Pelosi et al., 2014), and includes an external microphone and sound processor worn in the ear canal (Banakis Hartl and Jenkins, 2020). The Envoy Esteem is a non-rechargeable, battery-powered, completely implantable device that utilizes a piezoelectric sensor coupled to the incus, an implanted amplifying sound

processor, and a piezoelectric driver coupled to the head of the stapes (Banakis Hartl and Jenkins, 2020). The driver mechanically vibrates the stapes (Marzo et al., 2014). However, the device requires that the ossicular chain be disarticulated (the incus separated from the stapes) to prevent any feedback between the sensor and driver. This results in a new conductive hearing loss on top of the sensorineural hearing loss the patient is already experiencing (Banakis Hartl and Jenkins, 2020). Furthermore, some studies have reported that although the device provides a functional gain, it has a limited benefit on frequencies above 3 kHz (Gerard et al., 2012; Chen et al., 2004). Only the Envoy Esteem provides a fully implantable option with a middle ear sensor replacing the external microphone (Babajanian et al., 2024), but all three devices use implanted mechanical attachments to vibrate and relay the amplified signals to the inner ear. Studies have shown that these middle ear implants can improve audiologic outcomes and patient satisfaction (McRackan et al., 2018; Monini et al., 2016), but they have not gained significant market penetrance, and their adoption rates remain low (Babajanian et al., 2024; Banakis Hartl and Jenkins, 2020).

One possible reason for the low adoption rate is the invasive surgical procedure associated with these implants. Implanting a mechanical driver can be invasive, especially when an external hearing aid device is a viable alternative option and surgery is not required. Of the three devices, the Ototronix MAXUM system offers the least invasive procedure, using a transcanal stapedectomy-like approach that involves creating an ear canal incision approximately 6 mm from the eardrum and elevating the tympanomeatal flap to access the middle ear space. Care needs to be taken during this procedure to avoid injuring the chorda tympani nerve (Pelosi et al., 2014). The Envoy Esteem and the Med-El Vibrant SoundBridge both require a mastoidectomy with posterior tympanotomy, revealing the facial nerve, similar to a cochlear implant surgery (Graf et al., 2022; Marzo et al., 2014). For both implants, the size of the implanted device requires a wider facial recess opening than in standard cochlear implant surgery in order to fit the device into the middle ear space (Mlynski et al., 2015; Marzo et al., 2014; McKinnon, 2010). A wide facial recess opening increases the risks of

facial paralysis and/or taste dysfunction (Mlynski et al., 2015; McKinnon, 2010).

An alternative approach to using an implanted vibrating driver is to use an implanted middle ear speaker. A speaker would require a smaller opening to the middle ear space in order to inject the amplified acoustic signals, and the device could be anchored to the patient's mastoid process in the skull (Miller, 2004). This approach has been introduced in the literature; however, to our knowledge, there has been limited research exploring its potential use. O'Connor and Puria (2006) presented experimental data using human cadaveric temporal bone measurements where they directly injected acoustic pressures into the middle ear cavity and recorded the response at the stapes. For comparison, they also conducted measurements by injecting acoustic pressures into the ear canal. They found that both cases performed approximately the same below 8 kHz, provided that the ear canal remained unplugged. While the authors included a block diagram to represent the experimental setup, they did not analyze how the injected middle ear pressure can be used to amplify sounds at the stapes. In addition, a few patents have been filed that describe the use of an implanted speaker for hearing aid applications. For instance, in Zilberman and Schulman (2003), they outlined a system comprising a pair of middle ear transducers that would be individually responsive to phase offset electric drive signals. The first transducer would be used to deliver the amplified sounds, and the second transducer was introduced for its phase offset capability, which would help minimize signal cancellation that can occur when in-phase sound energy also enters the round window. Furthermore, in Miller (2004), they outlined a design of a speaker mounted within a patient's mastoid process that would be used to amplify the vibration of the eardrum. However, neither patent offered an analysis of what amplified results a user might expect.

Fully implantable cochlear implants have been in development for many years (Briggs et al., 2008), but there is no commercially available device ready for implantation and FDA-approved (Babajanian et al., 2024). However, clinical study trials are underway. In Europe, it was reported in September 2020 that a clinical study of a totally implantable cochlear implant

(TICI) by Med-El had begun (D'Haese, 2020), and in the U.S., the FDA recently (November 2024) approved the investigational device exemption application by Envoy Medical for its study of the Acclaim fully implanted cochlear implant (Envoy, 2024). Researchers have stated that the main barrier to the wider adoption of fully implantable cochlear implants is the lack of a robust, broadband, fully implantable acoustic sensor capable of replacing the external microphone (Babajanian et al., 2024; Trudel and Morris, 2022). The same challenge is faced by the FDA-approved middle ear implants, two of which still rely on external components.

1.2.4 Sensing mechanisms for totally implantable systems

Developing an implantable sensor that can rival external commercial microphones has proven to be a substantial undertaking (Trudel and Morris, 2022). Because of this gap, many researchers have developed prototype implantable sensors. Subcutaneous microphones have been utilized and reduced to practice (Bruschini et al., 2009; Pulcherio et al., 2014). However, their performance has been adversely impacted by surrounding tissue and internal body noise (Trudel and Morris, 2022; Calero et al., 2018). As mentioned previously, a middle ear microphone would avoid these deficiencies and provide pinna cues, wind noise reduction, and middle-ear gain (Babajanian et al., 2024; Trudel and Morris, 2022), each of which would improve the acoustic performance of the device. Hence, there is an expanding literature on implantable middle ear sensors for prosthesis use. For example, in Jia et al. (2016), a floating piezoelectric microphone with a total size of 5.91 mm $\times$ 2.4 mm $\times$ 2.02 mm and a mass of 67.0 mg was developed. However, this sensor is as long as the long process of the incus (the intended attachment location) and more than twice the mass of the incus (Noussios et al., 2016; Zhao et al., 2009). In İlik et al. (2018), a pulsed laser technique was used to deposit a lead zirconate titanate (PLD-PZT) thin film as part of a piezoelectric acoustic transducer that utilized eight cantilever beams, each resonating at a specific sub-bandwidth range within the full bandwidth of 250 Hz - 5 kHz. However, allowing the beams to resonate within the full bandwidth may require additional complex filtering as the

sensitivity responses would not be constant throughout that range. In Yeiser et al. (2024), a 3 mm × 3 mm × 200 µm polyvinylidene difluoride (PVDF) piezoelectric cantilever sensor that measures the motion at the umbo was presented. The sensor has a comparable noise floor to a commercial Knowles microphone; however, in order for the sensor to operate as intended, a large external 3D-printed clamp is used to hold it under the umbo. The authors also mention that biocompatibility may be an issue. In Sachse et al. (2013), a capacitive accelerometer of small size (2.1 mm × 2.1 mm × ∼350 µm) capable of meeting the 40-phon noise floor (BS ISO 226:2003) over a 0.1 kHz bandwidth was designed and developed. However, this sensor does not cover the operational frequency range of commercial microphones from 100 Hz – 8 kHz (Calero et al., 2018; Zeng et al., 2008). Other sensors were reviewed in Puria (2013), Calero et al. (2018), and Trudel and Morris (2022), which show that progress is being made in the field. However, to our knowledge, none of the prototypes presented in the literature meet the criteria of bandwidth (100 Hz – 8 kHz), low noise floor, and sufficiently small volume necessary for implantation.

1.3 Thesis overview and outline

To simultaneously address the three criteria of frequency bandwidth, noise floor, and small size for a middle ear sensor, we developed a discretized and exhaustive design optimization approach for multi-bandwidth microelectromechanical systems (MEMS) accelerometers that includes the bandwidth, noise floor, and sensor geometry as part of the cost function. We use multi-bandwidth proof-mass-loaded piezoelectric cantilever bimorph accelerometers and select aluminum nitride (AlN) as the piezoelectric material because of its low dielectric losses, aiding in the low-noise requirement. Our previous work used an experimentally validated analytical model (Hake et al., 2021) to show that a 20-phon noise floor design could be met with a dual-bandwidth sensor (Hake et al., 2023). This dual-bandwidth sensor was comprised of two piezoelectric cantilever bimorph plates (sensing elements), each operating

over different sub-bandwidths (together adding up to the full operational bandwidth). Each sensing element was designed for a nearly constant sensitivity response over the designated sub-bandwidth. The dual-bandwidth design was significantly better than a single-bandwidth design. The natural question then is: what is the number of sensing elements (i.e., number of sub-bandwidths) that continue to meet the full operational bandwidth with constant sensitivity and low-noise floor, but will also further minimize the size of the sensor? The work presented in Chapter 2 aims to answer this question by investigating multi-bandwidth accelerometer designs. In addition, the work presented in Chapter 3 investigates the effect of the piezoelectric thickness and material properties on the sensor area of three single-bandwidth piezoelectric sensors. Although this study is set up to investigate sensors for general applications with broader operational bandwidths than in Chapter 2, all three designs have been or are currently used in research for totally implantable auditory prostheses (Bruschini et al., 2009; Hake et al., 2023; Yeiser et al., 2024). Thus, the work presented in this chapter can inform future sensor designs for prosthesis applications.

Furthermore, we outlined in Section 1.2.3 that all three commercial middle ear implants utilize direct mechanical attachments (e.g., transducer on the stapes) to deliver amplified electrical signals to the inner ear. In the work presented in Chapter 4, we explore an analysis of an alternative approach, where acoustic stimuli are delivered to the middle ear using an implanted acoustic middle ear speaker rather than a vibrating driver. We utilize a lumped parameter model of the middle ear presented in Han et al. (2023) to conduct our investigation. We excite the model with an external pressure on the eardrum and with an internal pressure within the middle ear cavity acting on the eardrum and the stapes.

Finally, in Chapter 5, we will summarize the conclusions from each chapter and highlight this author's contributions. The chapter will conclude with suggestions for potential future research directions.

CHAPTER 2

Modeling of Piezoelectric MEMS Sensors

MEMS sensors prevail in consumer electronics such as smartphones, computers, and automobiles (Zheng et al., 2024). Specifically, piezoelectric MEMS sensors have many applications, including acoustic sensors, force sensors, accelerometers, and pressure sensors (Kumar et al., 2022). These sensors are well-suited for portable and lightweight applications as they do not require input power and can be less susceptible to external environmental conditions with robust designs (Zheng et al., 2024). Their performance is typically evaluated using a number of metrics, with two notable metrics being sensitivity and input-referred noise. Sensitivity is the ratio of the magnitudes of the output sensor signal to the input stimulus (Liu, 2012). Input-referred noise is the intrinsic sensor noise spectral density due to the dielectric losses in the piezoelectric material, divided by the sensitivity. This value determines the minimum input signal detectable above the noise floor of the sensor (Hake, 2021).

In this chapter, we explore the phenomenon of piezoelectricity, discovered in the late nineteenth century, and provide an overview of its mathematical descriptions. Next, we detail the design investigation of piezoelectric multi-bandwidth accelerometers for totally implantable auditory prostheses. We outline the constraints (full operational bandwidth, noise floor, and size) that limit the design space and describe the accelerometer design layout. Lastly, we show how the design optimization approach identifies and selects the multi-bandwidth configuration that minimizes the sensor size.

2.1 Equations of piezoelectricity

Piezoelectric materials are crystals that exhibit piezoelectricity due to the displacement of positive and negative ions within the crystal lattice, which results in depolarization and, hence, an electric field. When a mechanical stress is applied to the crystal, it changes the spacing between the positive and negative ions, generating a measurable voltage on the surface of the crystal. This phenomenon is known as the direct piezoelectric effect. Conversely, if an electric field or voltage is applied to the same material, it undergoes mechanical deformation. This is known as the inverse piezoelectric effect. In 1880, the direct piezoelectric effect was first experimentally discovered in naturally-occurring substances such as quartz and Rochelle salt, and the term piezoelectricity was adopted from the Greek "piezo", which means "to press" (Liu, 2012). A piezoelectric sensor utilizes the direct piezoelectric effect, whereas a piezoelectric actuator utilizes the inverse piezoelectric effect (Littrell, 2010).

Two constitutive equations can be used to model piezoelectric material (Hake, 2021; Liu, 2012; Littrell, 2010; Berlincourt et al., 1964). The first equation relates the 3×1 electrical displacement vector $\boldsymbol{D}$ and the 6×1 applied mechanical stress vector $\boldsymbol{T}$:

$$\boldsymbol{D} = [d]\boldsymbol{T} + [\epsilon^T]\boldsymbol{E} \ , \tag{2.1}$$

where $[d]$ is the 3×6 piezoelectric coefficient matrix, $[\epsilon^T]$ is the 3×3 piezoelectric permittivity matrix measured under constant stress, and $\boldsymbol{E}$ is the 3×1 electrical field vector.

The second equation relates the 6×1 total strain vector $\boldsymbol{\varepsilon}$ to the applied electrical field vector $\boldsymbol{E}$:

$$\boldsymbol{\varepsilon} = [s^E]\boldsymbol{T} + [d^t]\boldsymbol{E} \ , \tag{2.2}$$

where $[s^E]$ is the 6×6 piezoelectric elastic compliance matrix measured under a constant electric field and $[d^t]$ is the transpose of the piezoelectric coefficient matrix.

The simplification of these equations depends on the specific piezoelectric material being modeled. Aluminum nitride (AlN) is one piezoelectric material of interest that belongs to

the dihexagonal polar class of crystals and has a reduced number of non-zero terms in the material matrices ($[s^E]$ and $[d]$) (Hake, 2021; Littrell, 2010). In Section 2.3.3, we will further explore how these piezoelectric equations are used to model sensors.

2.2 Piezoelectric output and combining layers

To effectively measure voltage from a bending piezoelectric material or to enable transverse (z-axis in Fig. 2.1) mechanical deformation using a voltage stimulus, the neutral axis of the piezoelectric material must lie either above or below the neutral axis of the overall structure. This necessitates that the piezoelectric element be a part of a layered structure. A layered structure can be achieved either by stacking a support layer with the piezoelectric layer (unimorph) or by stacking two or more piezoelectric layers (bimorph or multimorph) (Hake, 2021). Generally, a bimorph design improves the performance of piezoelectric transducers compared to a unimorph design (Lou et al., 2016; Littrell, 2010; Wang and Cross, 1998). Therefore, the piezoelectric sensors presented in this thesis use a bimorph design.

Each piezoelectric layer in the bimorph design is modeled as a parallel resistor-capacitor (RC) pair. Depending on the desired output, two piezoelectric layers can be connected either in series or in parallel. The in-series connection of two identical piezoelectric layers will double the intrinsic noise of the sensor (Littrell, 2010). Thus, in the sensor designs presented in this work, all piezoelectric layers are connected in parallel.

2.3 Multi-bandwidth accelerometer methods

2.3.1 Design constraints

Three main constraints limit the design of a multi-bandwidth accelerometer. First, the full operational bandwidth is specified to 100 Hz – 8 kHz, which is based on the bandwidth used by commercial HAs and CIs (Calero et al., 2018; Zeng et al., 2008). Second, the starting

target low-noise floor is 20-phon because it nearly encompasses the entire conversational speech range (Mueller et al., 2014; BS ISO 226:2003, 2003). Last, as space is limited within the middle ear cavity, the total device's size, which includes the MEMS sensor, accompanying circuitry, and packaging, should be as small as possible to reduce the mass loading on the ossicles and account for limitations during surgical implantation. Due to the 3-D nature of the middle ear (Figure 1.1), distances are difficult to identify directly. Two notable middle ear space constraints are the distances between the long process of the incus and the promontory (3.6 mm) and between the umbo of the malleus and the promontory (2.1 mm). These are average values determined by Stieger et al. (2006) using a mix of male and female temporal bones. The latter distance serves as a space constraint for umbo sensors.

2.3.2 Accelerometer design layout

The accelerometer design concept used in this work is shown in Fig. 2.1. It consists of a piezoelectric bimorph cantilever plate tip-loaded by a silicon proof mass that produces an output voltage (V_{out}) when deflected due to sound-induced ossicular vibrations. The piezoelectric plate consists of two AlN layers intermixed with three electrode layers (on the top, in the middle, and on the bottom). In Fig. 2.1(a), we display a top-view schematic of the MEMS die that sits on top of a printed circuit board (PCB), showing the necessary electronics to extract and amplify the output voltage, and in Fig. 2.1(b) we show a side view of that schematic. The variables associated with the dimensions of the sensor are labeled in both Figs. 2.1(a) and (b).

Figure 2.2 exemplifies a MEMS die layout of a multi-bandwidth design with four cantilever bimorph plates. Each plate is designed to operate over a sub-bandwidth of the full operational bandwidth. Necessary amplification and further filtering are needed to manage the transition between these sensing elements and to equalize sensitivities over that full operational bandwidth, as described in Hake et al. (2023).

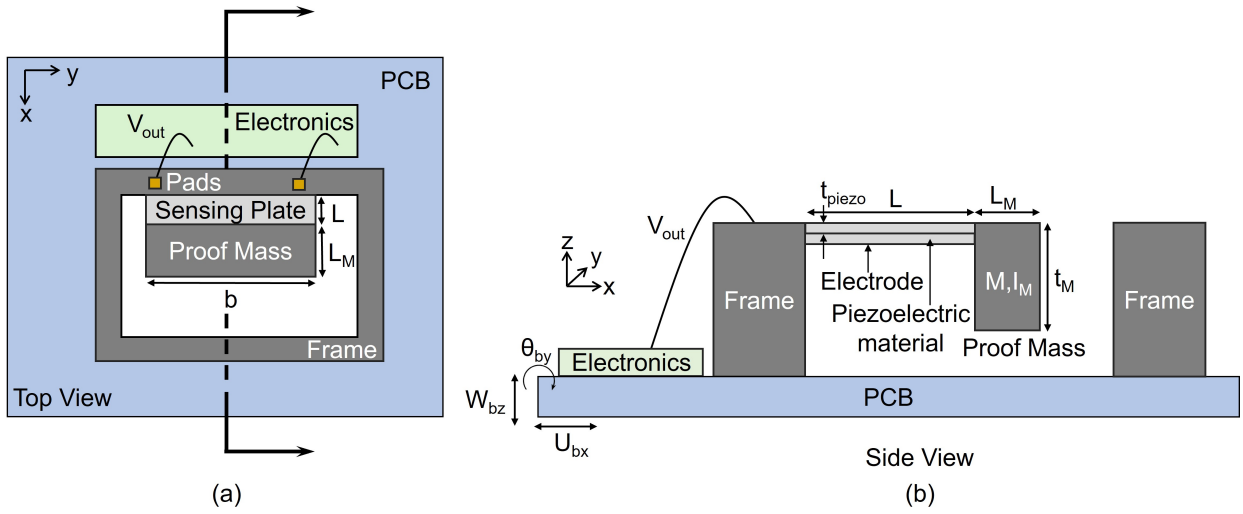

Figure 2.1: Example of an accelerometer comprised of one piezoelectric cantilever bimorph plate. (a) Top view, and (b) side view of the sensor assembly (cut plane shown in (a)). The design consists of two AlN layers (piezoelectric material) of length L, single piezoelectric layer thickness t_{piezo}, and width b. Three electrodes are on the bimorph's top, middle, and bottom. The proof mass sits flush against the plate and has length L_M, thickness t_M, width b, mass M, and moment of inertia I_M (Hake et al., 2021). The entire device is mounted on a PCB that also holds the signal conditioning electronics to extract the output voltage, V_{out}, from the piezoelectric material. W_{bz} is defined as the prescribed base displacement in the z-direction, U_{bx} is defined as the prescribed based displacement in the x-direction, and θ_{by} is defined as the prescribed base rotation about the y-axis. The packaging of the device is not shown. Not to scale. Adapted from Hake et al. (2023).

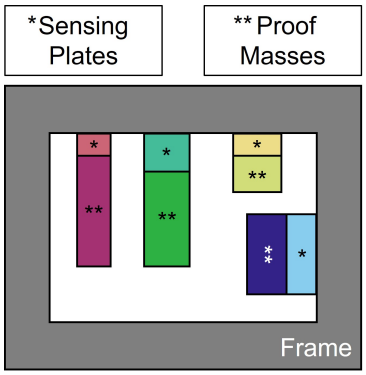

Figure 2.2: Example of a multi-bandwidth MEMS die layout with four sensing elements (top view). Each element has a piezoelectric bimorph plate and a proof mass, and each operates over a sub-bandwidth of the full operational bandwidth.

2.3.3 Full analytical accelerometer model

The full analytical model used to simulate the response of a vibrating sensing element is presented here (updated from Hake (2021) and Hake et al. (2021)). The accelerometer can be subjected to either transverse displacement (W_{bz}), longitudinal displacement (U_{bx}), rotation (θ_{by}), or a combination of all (as exemplified in Fig. 2.1(b)). The model accounts for the cross-axis sensitivity of the accelerometer by incorporating the transverse (z-axis) and longitudinal (x-axis) coupling in the boundary conditions (Eqs. 2.7–2.12). We also add hysteretic damping to this model to match experimental results found in similar fabricated accelerometer designs (Hake, 2021). Damping is included through the beam bending stiffness (EI) by defining a complex modulus as $EI^* = EI(1 + j\eta)$, where we choose a loss factor, $\eta = 0.06$ (Cremer and Heckl, 1988). For this hysteritic damping model, it can be shown that the Q factor is $Q = 1/\eta$ (Cremer and Heckl, 1988), where, Q is defined as $f_p/(f_2 - f_1)$, f_p is the frequency of peak velocity response, and f_1 and f_2 are the frequencies for which the velocity squared is one-half the velocity squared at f_p (i.e., $v^2(f_p)/2 = v^2(f_1) = v^2(f_2)$, where $v(f)$ is the magnitude of the velocity at f). Thus, as we assume the same loss factor, η, for all designs in this investigation, the Q factor is approximately 16.5 for all designs. Furthermore, the effect of the electrode layers on the mechanics is neglected as they are thin compared to the piezoelectric layers. However, if the electrode thickness is non-negligible, then this effect can be included in the calculation of the bending stiffness (Krommer, 2001; Littrell and Grosh, 2012).

The model assumes the Bernoulli-Euler beam hypothesis and an $e^{j\omega t}$ time dependence, which results in the following governing equations for transverse and longitudinal deflection:

$$\overline{EI}\frac{d^4W(x)}{dx^4} - \omega^2\rho_{AlN}AW(x) = 0 \ , \tag{2.3}$$

$$\frac{A}{s_{11}^E}\frac{d^2U(x)}{dx^2} + \omega^2\rho_{AlN}AU(x) = 0 \ , \tag{2.4}$$

where $\omega = 2\pi f$ is the radian frequency, f is the frequency of vibration, $A = 2t_{piezo}b$ is

the cross-section area of the beam, and ρ_{AlN} is the density of the piezoelectric material. $\overline{EI}$ is the effective beam bending stiffness that accounts for the piezoelectricity calculated as $\overline{EI} = \frac{bt_{piezo}^3}{s_{11}^E}(\frac{2}{3} + \frac{1}{6}\frac{d_{31}^2}{\epsilon_{33}^S s_{11}^E})$ (Krommer, 2001; Littrell and Grosh, 2012), where d_{31} is the piezoelectric coefficient, s_{11}^E is the piezoelectric elastic compliance measured under a constant electric field, and ϵ_{33}^S is the piezoelectric relative permittivity measured under zero strain, where $\epsilon_{33}^S = \epsilon_{33}^T - d_{31}^2/s_{11}^E$ and ϵ_{33}^T is the permittivity measured under constant stress.

The solutions to Eq. 2.3 and Eq. 2.4 are:

$$W(x) = C_1 \sin(\gamma x) + C_2 \cos(\gamma x) + C_3 \sinh(\gamma x) + C_4 \cosh(\gamma x) \ , \tag{2.5}$$

$$U(x) = C_5 \sin(\beta x) + C_6 \cos(\beta x) \ , \tag{2.6}$$

where $\gamma = (\rho_{AlN} A\omega^2/\overline{EI})^{\frac{1}{4}}$ and $\beta = \omega\sqrt{\rho_{AlN} s_{11}^E}$. The coefficients $C_1 - C_6$ are determined using the boundary conditions defined for this vibrating accelerometer system. At $x = 0$, where the piezoelectric beam connects to the silicon frame (Fig. 2.1(b)), the prescribed displacement in the z-direction and the slope condition are equal to W_{bz} and θ_{by}:

$$W(0) = W_{bz} \ , \tag{2.7}$$

$$\tfrac{dW(0)}{dx} = \theta_{by} \ , \tag{2.8}$$

and the prescribed displacement in the x-direction is U_{bx}:

$$U(0) = U_{bx} \ . \tag{2.9}$$

At $x = L$, where the piezoelectric beam connects to the proof mass, bending moment and force boundary conditions are generated:

$$\overline{EI}\frac{d^2W(L)}{dx^2} = \frac{1}{2}ML_M\omega^2 W(L) + I_M\omega^2\frac{dW(L)}{dx} + M\omega^2\left(\frac{t_M}{2} - t_{piezo}\right)U(L) + M_e \ , \tag{2.10}$$

$$\overline{EI}\frac{d^3W(L)}{dx^3} = -M\omega^2 W(L) - \frac{1}{2}ML_M\omega^2\frac{dW(L)}{dx} \ , \tag{2.11}$$

$$\frac{A}{s_{11}^E}\frac{dU(L)}{dx} = M\omega^2 U(L) + M\omega^2\left(\frac{t_M}{2} - t_{piezo}\right)\frac{dW(L)}{dx} \ , \tag{2.12}$$

where $I_M = \frac{\rho_M L_M A_M}{3}(L_M^2 + t_M^2 - 3t_{piezo}t_M + 3t_{piezo}^2)$ is the moment of inertia of the proof mass, ρ_M is the density of the proof mass, A_M is the cross-section area of the proof mass, and M_e is the electrical moment due to the stacked identical piezoelectric layers connected in parallel. The derivation of M_e is provided in Krommer (2001) and Littrell and Grosh (2012):

$$M_e = -\frac{bd_{31}t_{piezo}}{s_{11}^E}V_{out} \ . \tag{2.13}$$

We can solve for V_{out} using the piezoelectric equations presented in Section 2.1 (Eqs. 2.1 and 2.2). As the piezoelectric plates are much wider than they are thick, we use the plane-strain constitutive relationship instead of the uniaxial stress assumption associated with the Bernoulli-Euler beam theory (Hake, 2021). Thus, we assume that T_z, ε_z, and all shear stress and strain components are zero, whereas T_x and T_y are non-zero. Note that the subscripts of x, y, and z correspond to the traditional axis labels of 1, 2, and 3. As the only electrodes on the piezoelectric layers are on the top, middle, and bottom surfaces (see Fig. 2.1(b)), only the electrical displacement and field in the z-direction are non-zero ($D_z, E_z \neq 0$). These assumptions simplify Eqs. 2.1 and 2.2:

$$D_z = d_{31}T_x + d_{32}T_y + \epsilon_{33}^T E_z \ , \tag{2.14}$$

$$\varepsilon_x = s_{11}^E T_x + s_{12}^E T_y + d_{31}E_z \ , \tag{2.15}$$

$$\varepsilon_y = s_{21}^E T_x + s_{22}^E T_y + d_{32}E_z \ . \tag{2.16}$$

We assume that ε_y becomes zero as the piezoelectric width increases. Thus, we can use Eq. 2.16 to solve for T_y and plug the result into Eqs. 2.14 and 2.15. Furthermore, due to the piezoelectric material symmetry considered in this thesis (AlN), we have that $s_{11}^E = s_{22}^E$,

$s_{12}^E = s_{21}^E$, and $d_{31} = d_{32}$ (Littrell, 2010). Equations 2.14 and 2.15 are updated as follows:

$$D_z = \tilde{d}_{31} T_x + \tilde{\epsilon}_{33}^T E_z \ , \tag{2.17}$$

$$\varepsilon_x = \tilde{s}_{11}^E T_x + \tilde{d}_{31} E_z \ , \tag{2.18}$$

where $\tilde{d}_{31} = d_{31}(1 - (s_{12}^E/s_{11}^E))$, $\tilde{\epsilon}_{33}^T = \epsilon_{33}^T - (d_{31}^2/s_{11}^E)$, and $\tilde{s}_{11}^E = s_{11}^E(1 - (s_{12}^E/s_{11}^E)^2)$ (Hake et al., 2023; Hake, 2021). We use these plane-strain material property equivalents for all calculations presented in this thesis.

Now, using Eqs. 2.17 and 2.18, we can solve for the total charge generated from both piezoelectric layers (Q^c) and, subsequently, V_{out}. Krommer (2001) presents the detailed derivation for Q^c, with three key assumptions being that the stacked piezoelectric layers are identical, the middle electrode is grounded, and the total Q^c for a parallel piezoelectric connection is the difference between the charge output of the top and bottom layers:

$$Q^c = CV_{out} + \frac{\tilde{d}_{31} b t_{piezo}}{\tilde{s}_{11}^E} \left(\frac{dW(L)}{dx} - \frac{dW(0)}{dx} \right) , \tag{2.19}$$

where C is the parallel capacitance of the piezoelectric layers calculated as $C = 2\tilde{\epsilon}_{33}^S bL/t_{piezo}$.

2.3.3.1 Sensitivity

The sensitivity of the accelerometer ($S(f)$) as a function of frequency is the transfer function between the output voltage and the base excitation acceleration. In this thesis, only transverse base excitation is considered, and thus, the base acceleration is $\ddot{W}_{bz} = -\omega^2 W_{bz}$ and $S(f) = V_{out}(f)/(\omega^2 W_{bz}(f))$ in units of V/(m/s^2), where both V_{out} and W_{bz} are also functions of frequency.

The full analytical model can be used to determine the open-circuit sensitivity ($Q^c = 0$). All boundary conditions from Eqs. 2.7–2.12 and the charge output equation (Eq. 2.19) are assembled in a matrix format with V_{out} and the corresponding coefficients $C_1 - C_6$ from Eqs. 2.5 and 2.6:

$$
\left[\begin{array}{cccccc|c|c}
0 & 1 & 0 & 1 & 0 & 0 & \begin{bmatrix} 0 \\ 0 \\ 0 \\ 0 \\ 0 \\ 0 \end{bmatrix} & \begin{bmatrix} C_1 \\ C_2 \\ C_3 \\ C_4 \\ V_{out} \\ C_5 \\ C_6 \end{bmatrix} = \begin{bmatrix} W_{bz} \\ \theta_{by} \\ 0 \\ 0 \\ 0 \\ U_{bx} \\ 0 \end{bmatrix} \\
\gamma & 0 & \gamma & 0 & 0 & 0 & & \\
X_1 & X_2 & X_3 & X_4 & \alpha & X_5 & X_6 & \\
X_7 & X_8 & X_9 & X_{10} & 0 & 0 & 0 & \\
\alpha \cdot \gamma(\cos(\gamma L) - 1^*) & -\alpha \cdot \gamma \sin(\gamma L) & \alpha \cdot \gamma(\cosh(\gamma L) - 1^*) & \alpha \cdot \gamma \sinh(\gamma L) & C & 0 & 0 & \\
0 & 0 & 0 & 0 & 0 & 0 & 1 & \\
X_{11} & X_{12} & X_{13} & X_{14} & 0 & X_{15} & X_{16} &
\end{array}\right] \tag{2.20}
$$

where $\alpha = b\tilde{d}_{31}t_{piezo}/\tilde{s}_{11}^{E}$. The expressions for X_1–X_{16} are given in Appendix A.1. Any values can be chosen for W_{bz}, θ_{by}, and U_{bx}. It is important to note that the (-1^*) term in Eq. 2.20 is included only if $\theta_{by} \neq 0$. As mentioned earlier, in this thesis, only transverse base excitation is considered ($W_{bz} \neq 0$, $\theta_{by} = 0$, and $U_{bx} = 0$), and thus the (-1^*) is removed. We normalize the results to W_{bz}.

2.3.4 Assumed-mode solution to full analytical model

2.3.4.1 Closed-form expression for the sensitivity

As outlined in Hake (2021), although the full analytical model provides a good approach to modeling the $S(f)$ of a piezoelectric sensor, it does not readily allow for the investigation of how various geometric parameters affect $S(f)$. An assumed-mode solution can allow for this investigation and provide a closed-form expression of $S(f)$ for low frequencies. Once again, as in this thesis, only transverse base excitation is considered; we assume that any longitudinal displacement ($U(x)$) and rotation are negligible for deriving the assumed-mode solution.

The assumed-mode solution to a statically bending beam with transverse displacement is given by:

$$W(x) = \tilde{C}_1 x^3 + \tilde{C}_2 x^2 + \tilde{C}_3 x + \tilde{C}_4 \ . \tag{2.21}$$

Using the boundary conditions in Eqs. 2.7–2.8, 2.10–2.11, and 2.19, we can assemble a new matrix with V_{out} and coefficients $\tilde{C}_1$–$\tilde{C}_4$:

$$\begin{bmatrix} 0 & 0 & 0 & 1 & 0 \\ 0 & 0 & 1 & 0 & 0 \\ \tilde{X}_1 & \tilde{X}_2 & \tilde{X}_3 & \tilde{X}_4 & -\alpha \\ \tilde{X}_5 & \tilde{X}_6 & \tilde{X}_7 & \tilde{X}_8 & 0 \\ \alpha(3L^2) & \alpha(2L) & \alpha & 0 & C \end{bmatrix} \begin{bmatrix} \tilde{C}_1 \\ \tilde{C}_2 \\ \tilde{C}_3 \\ \tilde{C}_4 \\ V_{out} \end{bmatrix} = \begin{bmatrix} W_{bz} \\ 0 \\ 0 \\ 0 \\ 0 \end{bmatrix} \tag{2.22}$$

The expressions for $\tilde{X}_1$–$\tilde{X}_8$ are given in Appendix A.2 and we normalize to W_{bz}.

To derive the closed-form expression for $S(f)$, we solve for V_{out} in Eq. 2.22 and divide it by the base excitation acceleration (recall that $\ddot{W}_{bz} = -\omega^2 W_{bz}$). As $S(f)$ is still a function of frequency, in order to investigate the low-frequency behavior of the vibrating system, we take the limit of $S(f) = V_{out}(f)/(\omega^2 W_{bz}(f))$ as ω approaches zero. This results in the following low-frequency sensitivity approximation:

$$\lim_{\omega \to 0} S(f) = \left| -\frac{3}{4} \frac{M\tilde{d}_{31}\tilde{s}_{11}^{E}(L_M + L)}{bt_{piezo}(\tilde{d}_{31}^2 - 2\tilde{\epsilon}_{33}^{S}\tilde{s}_{11}^{E})} \right| , \tag{2.23}$$

where $M = \rho_M L_M b t_M$ is the mass of the proof mass. This equation shows the dependence of $S(f)$ on the geometric and material properties of a piezoelectric sensor.

2.3.4.2 Noise floor and minimum detectable acceleration

The noise floor of this vibrating system is defined as the minimum detectable signal that an accelerometer can detect. For the piezoelectric cantilever bimorph plate, the theoretical value of the minimum detectable acceleration (MDA) is calculated as $MDA = |\sqrt{\overline{v_n^2}}/S(f)|$ with units of $(\mathrm{m/s^2})/\sqrt{\mathrm{Hz}}$, where $\overline{v_n^2}$ is the sensor noise spectral density due to the dielectric losses in the piezoelectric material in 1 Hz bandwidths. It is calculated using the Johnson noise equation as:

$$\overline{v_n^2} = 4k_B T^* |Re(Z)| , \tag{2.24}$$

with units of $\mathrm{V^2/Hz}$ and where k_B is the Boltzmann constant, T^* is the temperature in Kelvin, and $|Re(Z)|$ is the real part of the electrical impedance of the piezoelectric layer. We represent the piezoelectric layer as a parallel resistor-capacitor (RC) pair and connect the two piezoelectric layers in parallel to define the impedance Z, where $|Re(Z)| = \tan\delta/(\omega C)$ with $\tan\delta$ being the loss tangent of the piezoelectric material (AlN).

Using the closed-form expression for $S(f)$ calculated in the previous section (Eq. 2.23) and the calculated $\overline{v_n^2}$, we derive an approximate expression for the theoretical MDA_z with

a transverse base excitation (z-axis) (updated from Hake (2021) and Hake et al. (2021)):

$$MDA_z = \left| \sqrt{\frac{8k_BT}{9}} \underbrace{\frac{1}{\sqrt{\omega}}}_{\text{Frequency}} \underbrace{\frac{(2\tilde{d}_{31}^2 - 4\tilde{\epsilon}_{33}^S \tilde{s}_{11}^E)\sqrt{\tan\delta}}{\tilde{d}_{31}\tilde{s}_{11}^E \rho_M \sqrt{\tilde{\epsilon}_{33}^S}}}_{\text{Material properties}} \underbrace{\frac{\sqrt{t_{piezo}^3}}{L_M t_M \sqrt{bL}(L + L_M)}}_{\text{Sensing plate and proof mass dimensions}} \right|. \quad (2.25)$$

Equation 2.25 can be used to derive an explicit expression for the piezoelectric width, b, which we will show in Section 2.3.5.

2.3.4.3 Resonant frequency approximation

We recall from Sections 2.3.1 and 2.3.2 that a multi-bandwidth sensor must meet the full operational bandwidth of 100 Hz to 8 kHz, and each sensing element within the multi-bandwidth sensor operates over a sub-bandwidth of that full operational bandwidth (Fig. 2.2). Each sub-bandwidth has a lower (f_α) and an upper (f_β) frequency bound. The resonant frequency (f_{res}) of a sensing element defines the f_β of its sub-bandwidth, over which sub-bandwidth the sensing element maintains approximately constant sensitivity. Constant sensitivity is advantageous as it simplifies the sensor output and requires less filtering.

We set f_β as the frequency at which there is a 3 dB increase compared to the low-frequency asymptote ($f_\beta = f_{3\text{dB}}$). We can estimate $f_{3\text{dB}}$ using f_{res}, where $f_{3\text{dB}} \approx f_{\text{res}}/1.85$. This relationship was derived using the magnification factor equation (MF), where $MF \approx 1/(1 - (f_{3\text{dB}}/f_{\text{res}})^2)$ and $MF = 10^{3/20}$ for a 3 dB increase. Therefore, the constant sensitivity constraint depends on f_{res}.

The first resonance frequency for a vibrating sensing element can be found by simplifying the matrix shown in Eq. 2.22 to a 2×2 matrix using homogeneous boundary conditions, where $\tilde{C}_3 = 0$ from Eq. 2.8 when $\theta_{by} = 0$, $\tilde{C}_4 = 0$ from Eq. 2.7 when $W_{bz} = 0$, and $V_{out} = -\frac{\alpha}{C}\frac{dW(L)}{dx}$ from Eq. 2.19 when $Q^c = 0$. We can take the determinant of this 2×2

matrix to identify the first resonance frequency (updated from Hake (2021)):

$$\det \begin{bmatrix} 6\overline{EI}L - \frac{1}{2}ML_M\omega^2L^3 - L^2(3I_M\omega^2 + \frac{3\alpha^2}{C}) & 2\overline{EI} - \frac{1}{2}ML_M\omega^2L^2 - L(2I_M\omega^2 + \frac{2\alpha^2}{C}) \\ 6\overline{EI} + ML^2\omega^2(L + \frac{3}{2}L_M) & ML\omega^2(L + L_M) \end{bmatrix} = 0. \tag{2.26}$$

From this operation, we have the following approximate characteristic relation:

$$\tilde{A}(\omega_{\text{res}}^2)^2 + \tilde{B}(\omega_{\text{res}}^2) + \tilde{C} = 0 \ , \tag{2.27}$$

where $\tilde{A}$, $\tilde{B}$, and $\tilde{C}$ are provided in Appendix A.3.

The solution to Eq. 2.27 can be used to find ω_{res}^2, where $\omega_{\text{res}} = 2\pi f_{\text{res}}$. It is important to note that the width, b, can be entirely canceled out in Eq. 2.27, and it does not influence f_{res}. This equation shows that for any frequency sub-bandwidth, L, L_M, and t_M are related by the constraint of constant sensitivity, which depends on the upper frequency bound, f_β, of the corresponding sub-bandwidth. This relation becomes important when casting the optimization problem for designing multi-bandwidth accelerometers, which will be discussed in the next section.

2.3.5 Design optimization problem

We seek to design multi-bandwidth sensors that meet the full operational bandwidth with constant sensitivity and low-noise (20-phon) floor and minimize the total sensor area, A_S^{tot}, where $A_S^{tot} = \sum_{i=1}^{N} A_{sur}^i$, N is the total number of sensing elements in a multi-bandwidth design, and A_{sur}^i is the surface area corresponding to each ith sensing element in that design. The surface area, A_{sur}^i, is defined as the total length multiplied by the width ($A_{sur}^i = (L_i + L_{M_i}) \cdot b_i$). The overall MEMS die area, A_{MEMS}^{tot}, of a multi-bandwidth design with N sensing elements is computed as the sensor area, A_S^{tot}, plus the added area due to the frame width and spacing in between sensing elements necessary for fabrication, A_{space}, so that $A_{MEMS}^{tot} = A_S^{tot} + A_{space}$. We do not include A_{space} in the optimization because

it depends on the sensor topology (shown in Fig. 2.2 where $N = 4$), as well as on processing and manufacturing factors such as limits to the sensing element spacing due to etching of high-aspect ratios (Tadigadapa and Lärmer, 2011). The material properties of the system are fixed, and hence, the optimization problem becomes one of geometry and frequency sub-bandwidth selection subject to certain constraints.

Thus, the optimization problem for an Nth-bandwidth design is:

$$\min(A_S^{tot}(\mathbf{L}, \mathbf{L_M}, \mathbf{b}, \mathbf{f})) \tag{2.28}$$

$$\text{subject to } \begin{cases} N \text{ contiguous sub-bandwidths defined by } \mathbf{f} \\ \text{constant sensitivity over each sub-bandwidth} \\ \text{meet 20-phon noise floor over each sub-bandwidth} \end{cases}$$

where $\mathbf{L}$, $\mathbf{L_M}$, and $\mathbf{b}$ are vectors corresponding to the geometric dimensions of each sensing element within an Nth-bandwidth design, and $\mathbf{f}$ is a vector corresponding to the lower (f_{α_i}) and upper (f_{β_i}) frequency bounds for each ith sub-bandwidth in the Nth-bandwidth design. In addition, $\mathbf{L}$, $\mathbf{L_M}$, and $\mathbf{b}$ implicitly depend on the piezoelectric thickness of each bimorph layer, t_{piezo}, and the proof mass thickness, t_{M_i}, through the constraints of bandwidth, constant sensitivity, and noise-floor. In this chapter, t_{piezo} is fixed to $t_{piezo} = 0.5$ µm (total sensing plate thickness is 1 µm), based on literature evidence and experience in depositing high-quality AlN films (Littrell and Grosh, 2012; Martin et al., 2004). In Chapter 3, we will investigate the effect of the piezoelectric thickness and material properties ($\tilde{d}_{31}$ and $\tan\delta$). Next, we show how we can reduce the complexity of the optimization via the approximate enforcement of the constraints.

First, we showed in Section 2.3.4.3 that there exists an implicit relation between L_i, L_{M_i}, t_{M_i}, and f_{β_i} (since $f_{\beta_i} \approx f_{\text{res}_i}/1.85$) for each ith sub-bandwidth that constrains the design space (Eq. 2.28).

Second, for each ith sub-bandwidth, we can derive an explicit expression for b_i using

the noise-floor constraint presented in Section 2.3.4.2. From Eq. 2.25 we observe that the MDA_z monotonically decreases over each ith sub-bandwidth (shown in Fig. 2.3(b)). Hence, we can approximate the enforcement of the 20-phon noise floor over an ith sub-bandwidth by ensuring that the 20-phon noise target ($MDA_z^{\text{20-phon}}$) is met at the lower frequency bound of that ith sub-bandwidth (f_{α_i}) (BS ISO 226:2003). The 20-phon noise target, $MDA_z^{\text{20-phon}}$, is computed by determining the ossicular accelerations due to 20-phon sound levels across the full operational frequency range (100 Hz – 8 kHz). The 20-phon contours from Fig. 1.3 are converted to umbo acceleration values using data from Sachse et al. (2013) and Goode et al. (1996), as described in Hake et al. (2023). A more detailed description of this operation is provided in Appendix A.4. It is important to note that the BS ISO 226:2003 uses a 1-2 second duration of a tone to investigate the normal equal-loudness-level contours, which is consistent with our use of a 1 Hz bandwidth for the sensor noise spectral density (Eq. 2.24). The umbo is chosen because of the extensive data available at this location (Goode et al., 1996), and while other locations are possible, they typically exhibit lower accelerations than at the umbo (Gan et al., 2004). These umbo acceleration values are used throughout the design optimization process.

Thus, using Eq. 2.25 and the target $MDA_z^{\text{20-phon}}$ at f_{α_i}, we can write b_i as an explicit function of f_{α_i}, L_i, L_{M_i}, and t_{M_i} for each ith sub-bandwidth as:

$$b_i = \left(\left| \sqrt{\frac{8k_BT}{9}} \quad \underbrace{\frac{1}{\sqrt{2\pi f_{\alpha_i}}}}_{\text{Lower frequency bound}} \quad \frac{(2\tilde{d}_{31}^2 - \tilde{\epsilon}_{33}^S \tilde{s}_{11}^E)\sqrt{\tan\delta}}{\tilde{d}_{31}\tilde{s}_{11}^E \rho_M \sqrt{\tilde{\epsilon}_{33}^S}} \right.\right.$$
$$\left.\left. \times \frac{\sqrt{t_{piezo}^3}}{L_{M_i} t_{M_i} \sqrt{L_i}(L_i + L_{M_i})} \quad \underbrace{\frac{1}{MDA_z^{\text{20-phon}}}}_{\text{Target noise floor at } f_{\alpha_i}} \right| \right)^2. \quad (2.29)$$

Once L_i and b_i are expressed as functions of the other variables for all sensing elements within a multi-bandwidth design, subject to the design constraints described previously, we can determine the sensor area, A_S^{tot}, of any multi-bandwidth design. Thus, now we can

re-cast our optimization problem from Eq. 2.28 to account for the geometric and frequency constraints on L_i and b_i as:

$$\min(A_S^{tot}(\mathbf{f}, \mathbf{L_M}, \mathbf{t_M})) \tag{2.30}$$

$$\text{subject to } \begin{cases} N \text{ contiguous sub-bandwidths defined by } \mathbf{f}, \text{ where } f_{\beta_i} > f_{\alpha_i} \\ \text{sensitivity changes less than 3 dB over each } i\text{th sub-bandwidth} \\ \text{meet 20-phon noise floor } (MDA_z^{\text{20-phon}}) \text{ at each } i\text{th sub-bandwidth} \end{cases}$$

where $\mathbf{L_M} \in \mathbb{R}^{\mathbf{N}}$, $\mathbf{t_M} \in \mathbb{R}^{\mathbf{N}}$, and $\mathbf{f} \in \mathbb{R}^{\mathbf{N}}$. Note that these constraints are now explicitly enforced, and the design space is reduced by one variable.

As an example, we show the computation for a single design sensor operating over a single bandwidth of 800 - 3150 Hz, a sub-bandwidth of the full operational bandwidth where the lower frequency bound is $f_\alpha = 800$ Hz and the upper bound is $f_\beta = 3150$ Hz. In this example, $L_M = 140$ µm and $t_M = 100$ µm, and L is calculated using Eq. 2.27 enforcing the constant sensitivity constraint over that bandwidth as shown in Fig. 2.3(a). Then, b is calculated using Eq. 2.29 to meet the 20-phon noise floor at f_α. Figure 2.3(b) compares the target 20-phon umbo acceleration values, $MDA_z^{\text{20-phon}}$ (black circles), with the theoretical noise floor of the designed sensor, MDA_z, calculated from Eq. 2.25. We note that in this example, although the accelerometer has a constant sensitivity below 800 Hz (less than 3 dB variation), it does not meet the 20-phon noise floor at those frequencies. Conversely, while the accelerometer meets the 20-phon noise floor above 3150 Hz, its sensitivity is not constant and would require complex filtering. Thus, the accelerometer's sub-bandwidth is constrained to 800 - 3150 Hz to meet both the constant sensitivity requirement and the 20-phon noise floor.

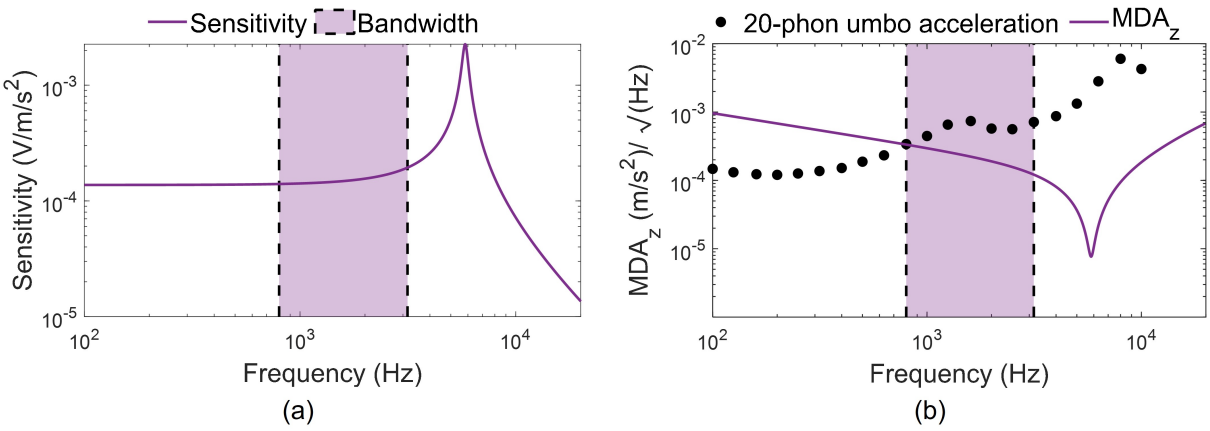

Figure 2.3: (a) Sensitivity of accelerometer with operational sub-bandwidth of 800 - 3150 Hz. The sensitivity is approximately constant until 3150 Hz, setting the upper frequency bound for this sensor (f_β). The resonance frequency, f_{res}, is 5828 Hz. (b) MDA_z curve of accelerometer plotted alongside 20-phon umbo acceleration values. The accelerometer meets the 20-phon noise floor at frequencies above 800 Hz, setting the lower frequency bound of this sensor (f_α). Here $L = 51$ µm, $L_M = 140$ µm, $t_M = 100$ µm, and $b = 128$ µm.

2.3.6 Design of multi-bandwidth accelerometers

In this section, we describe two optimization approaches to identifying multi-bandwidth designs that minimize the sensor area, A_S^{tot}, while meeting the 20-phon noise floor with constant sensitivity over the full operational bandwidth. In the first approach, the proof mass thickness, t_{M_i}, is freely varied within a multi-bandwidth design, whereas in the second approach, t_{M_i} is constrained to a single free value for all sensing elements in a multi-bandwidth design. The reason for the second approach is that prescribing multiple proof mass thicknesses adds process complexity and failure modes due to the limitations of deep reactive ion etching (DRIE) used in fabrication. The etch rate of DRIE has a strong dependence on the gap-to-height aspect ratio (Tadigadapa and Lärmer, 2011), which depends on the proof mass thicknesses. Nevertheless, the first approach provides a lower bound on the total sensor area for a given N, and it informs what designs to focus on and investigate for the second approach. For both approaches, the full operational bandwidth is split into N sub-bandwidths, corresponding to the number of sensing elements within a multi-bandwidth design.

2.3.6.1 Design of N-sensing elements with unconstrained proof mass thicknesses

In general multi-bandwidth designs, there are $N-1$ cross-over frequencies, and these frequencies are continuous variables. Cross-over frequencies correspond to the frequencies at which there is a transition from the operation of one sensing element to another. In order to limit the number of possible cross-over frequencies in this investigation, we limit the possible lower and upper bounds of each sub-bandwidth to correspond to the 20 center frequencies of the 1/3 octave band between 100 Hz – 8 kHz, as shown in Fig. 2.4 (i.e. the maximum number of frequencies we choose for our design space is $N_f^{\max} = 20$). Each cross-over value is labeled appropriately from f_2 to f_{19}. Note that f_1 and f_{20} are the fixed lower and upper bounds of the first and last sensing element in all designs. In general, the value of N is restricted to be between 2 and $N_f^{\max} - 1$ (i.e., $2 \leq N \leq N_f^{\max} - 1$).

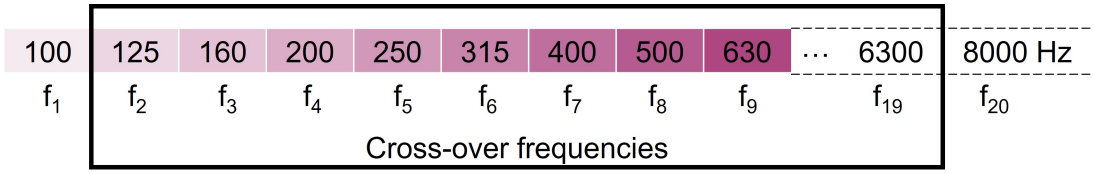

Figure 2.4: Discrete cross-over frequency values in Hz selected from the center frequencies of the 1/3 octave band. Cross-over values are labeled from f_2 to f_{19}. f_1 and f_{20} are the fixed lower and upper bounds of the first and last sensing element, respectively. $N_f^{\max} = 20$ in this case.

Adjacent frequency bounds must share the same cross-over frequency (i.e., $f_{\beta_i} = f_{\alpha_{i+1}}$) to ensure continuous operation over the full operational bandwidth. The first sensing element within a design is known as the lower frequency sensing element (LFSE). An LFSE must have a lower bound of 100 Hz ($f_{\alpha_1} = f_1$) and an upper bound chosen from the cross-over frequencies, f_{β_1}, where $2 \leq \beta_1 \leq N_f^{\max} - (N-1)$. Similarly, the last sensing element is known as the high frequency sensing element (HFSE), which will always have an upper bound of 8 kHz ($f_{\beta_N} = f_{20}$) and a lower bound, f_{α_N}, equal to the previous sensing element's upper bound, $f_{\beta_{N-1}}$, where $N \leq \alpha_N \leq N_f^{\max} - 1$. In the case of $N \geq 3$, all other sensing elements are known as middle frequency sensing elements (MFSE$_n$), where n is the number

of MFSEs within a design restricted by $1 \leq n \leq N-2$. The nth MFSE has varying lower ($f_{\alpha_{n+1}}$) and upper bounds ($f_{\beta_{n+1}}$), where $n+1 \leq \alpha_{n+1} \leq N_f^{\max} - (N-n)$ and $\alpha_{n+1}+1 \leq \beta_{n+1} \leq N_f^{\max} - (N-n)+1$. For example, in $N=3$, MFSE_1 has the lower bound $f_{\alpha_2} = f_{\beta_1}$ where $2 \leq \alpha_2 \leq 18$, and the upper bound f_{β_2} where $3 \leq \beta_2 \leq 19$ and $\beta_2 \geq \alpha_2$. In our design procedure, we seek to find the values of N and the combinations of cross-over frequencies that result in the smallest sensor area.

Our design optimization starts with investigating different lower and upper bound frequency combinations for all sensing elements (LFSE, MFSE_n, and HFSE). For every bandwidth combination, each sensing element's proof mass dimensions (thickness, t_{M_i}, and length, L_{M_i}) are varied from 10 µm to 300 µm each in 10 µm increments. As described in Sections 2.3.4.3 and 2.3.5, the plate length, L_i, required to meet the desired f_{res_i} that sets the upper frequency bound, is calculated using Eq. 2.27, and the width, b_i, is calculated using Eq. 2.29 so that each sensing element meets the 20-phon noise floor at the lower frequency bound. The sensing element design with the smallest surface area (A_{sur}^i) and associated dimensions t_{M_i}, L_{M_i}, L_i, and b_i is stored. The process is repeated for all sensing elements within a multi-bandwidth design, and the dependence of the sensor area (A_S^{tot}) on N is investigated, and the smallest sensor area design is selected.

2.3.6.2 Design of N-Sensing elements with constrained proof mass thicknesses

Next, we explore multi-bandwidth designs with the proof mass thicknesses constrained to a single free value for all sensing elements within a design. Similar to the previous section, this investigation starts with combining lower and upper frequency bounds for all sensing elements (LFSE, MFSE_n, and HFSE). We vary the proof mass thickness, t_{M_i}, and length, L_{M_i}, from 10 µm to 300 µm, and calculate plate length, L_i, and width, b_i. To determine the smallest sensor area design with single-proof-mass thicknesses, we have to identify all possible sensing element combinations that meet the single-proof-mass constraint before making the selection. This is unlike in the first approach, where we needed only to select

the smallest surface area for each sensing element individually because we were free to use different values of t_{M_i} for each sensing element. Thus, for each sensing element, we store all t_{M_i} and L_{M_i} combinations and other associated geometric dimensions for each f_{α_i} and f_{β_i} combinations. We use a matrix-within-matrix format to store all dimensions. This format includes an outer and an inner matrix. The outer-matrix dimensions are defined by the lower and upper frequency bounds (f_{α_i}, f_{β_i}) associated with a particular sensing element, and its size varies with the number of combinations of cross-over frequencies possible. The inner-matrix dimensions are defined by the combinations of t_{M_i} and L_{M_i} as $m_{t_{M_i}} \times m_{L_{M_i}}$, where $m_{t_{M_i}}$ is the number of values of t_{M_i}, and $m_{L_{M_i}}$ is the number of values of L_{M_i}. The sensor area (A_S^{tot}) for each geometry that meets the proof mass constraint and the 20-phon criterion is stored in the inner matrix. Finally, we analyze each inner matrix, and we store the lowest sensor area design for each t_{M_i}. Then, we search all possible combinations of sub-bandwidths to find the smallest sensor area N-bandwidth design with constrained proof mass thicknesses.

2.4 Results

All results presented in this section are calculated assuming a plane-strain constitutive hypothesis for the piezoelectric plate as outlined in Section 2.3.3. The AlN material properties used are $\rho_{AlN} = 3.26 \times 10^3$ (kg/m^3), $\tilde{s}_{11}^E = 2.6 \times 10^{-12}$ (m^2/N), $\tilde{d}_{31} = -2.5 \times 10^{-12}$ (C/N), $\tilde{\epsilon}_{33}^T = 10.0 \cdot 8.854 \times 10^{-12}$ (F/m) and $\tan(\delta) = 0.0015$ (measured experimentally for similar accelerometer designs in Hake et al. (2021) at 1 kHz) (Hake et al., 2023). To estimate the total MEMS die area of multi-bandwidth designs, A_{MEMS}^{tot}, previously mentioned in Section 2.3.5, we assume a frame width of 150 µm and a frame thickness of ∼500 µm that depends on the wafer size. For the spacing between sensing elements and between sensing elements and the frame, we estimate an etching aspect ratio of 10:1 to ensure smooth sidewall etching (Samco, 2024) and to avoid etching issues observed at higher aspect ratios (over 20:1) (Tadigadapa

and Lärmer, 2011). We use the 10:1 aspect ratio of the highest proof mass thickness within a design for all inter-sensing element spacing in that design to maintain uniformity. For the spacing between sensing elements and the frame, we use 50 µm because of the ∼500 µm frame thickness.

2.4.1 N-bandwidth designs with unconstrained proof mass thicknesses

Performing the unconstrained design investigation outlined in Section 2.3.6.1, we found that $N = 8$ sensing elements yield the smallest sensor area with an 84% reduction compared to the dual-bandwidth sensor presented in Hake et al. (2023). In Fig. 2.5, we show the prototypical MEMS die layouts for $N = 3, 4, 5,$ and 8. We observe that after $N = 5$, there is an increase in the predicted MEMS die area (A^{tot}_{MEMS}) due to the inter-sensing element and frame separation spacing (which is computed as outlined previously). The MEMS die areas of the three-bandwidth and four-bandwidth sensors achieve a 28% and 31% reduction compared to the dual-bandwidth sensor, whereas the MEMS die area of the five-bandwidth sensor is 1% greater than the four-bandwidth sensor, and the eight-bandwidth sensor is 11% greater. The dimensions of the four-bandwidth sensor are given in Table 2.1. The three-, five-, and eight-bandwidth sensor dimensions are given in Appendix A.5 in Tables A.2, A.4, and A.5. From these results, we identify that the number of sensing elements to best balance area minimization with the smallest estimated A^{tot}_{MEMS} is $N = 4$. Hence, we will explore the $N \leq 4$ design under the constrained t_M approach (second approach).

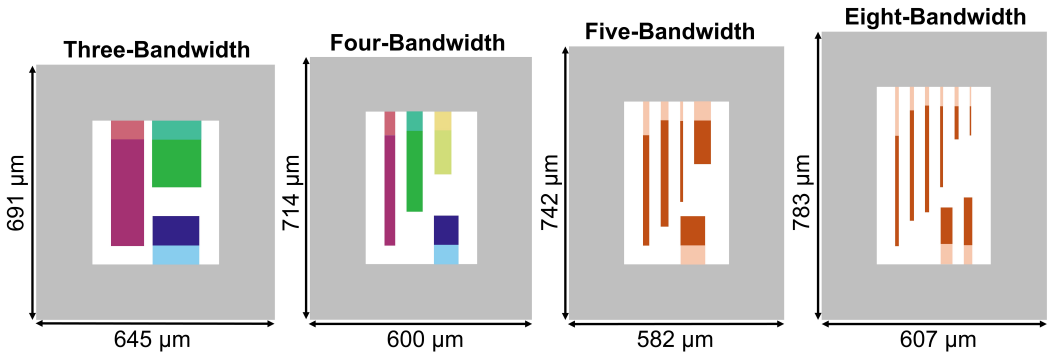

Figure 2.5: Overall MEMS dimensions of the unconstrained three-, four-, five-, and eight-bandwidth sensors in prototypical MEMS die layouts accounting for frame width and sensing element spacing using a 10:1 aspect ratio. The dimensions of the four-bandwidth sensor are given in Table 2.1 and the dimensions of the three-, five-, and eight-bandwidth sensors are given in the Appendix in Tables A.2, A.4, and A.5.

Table 2.1: Four-bandwidth sensor dimensions with unconstrained proof mass thicknesses. The sensor area is 3.94×10^{-8} m^2, and the estimated MEMS die dimensions are 714 µm × 600 µm with a MEMS die area of 4.28×10^{-7} m^2.

	LFSE	$MFSE_1$	$MFSE_2$	HFSE
t_M (µm)	300	170	90	60
L_M (µm)	300	220	120	80
L (µm)	64	53	51	53
b (µm)	29	44	46	67
Sub-Bandwidth Frequencies (kHz)	0.1 - 0.5	0.5 - 1.25	1.25 - 4	4 - 8

2.4.2 Four-bandwidth design with constrained proof mass thicknesses

The dimensions of the constrained four-bandwidth sensor are given in Table 2.2. We find that the constrained four-bandwidth design has a 42% increase in sensor area compared to the unconstrained design but only an 11% increase in MEMS die area. The constrained design is still smaller than the dual-bandwidth design that has two proof mass thicknesses (Hake et al., 2023), with a reduction of 64% in the sensor area and 23% in the MEMS die area. The total MEMS die mass of the constrained four-bandwidth design is estimated to be approximately 0.4 mg.

Table 2.2: Four-bandwidth sensor dimensions with constrained proof mass thicknesses. The sensor area is 5.60×10^{-8} m^2, and the estimated MEMS die dimensions are 825 µm × 575 µm with a MEMS die area of 4.74×10^{-7} m^2.

	LFSE	$MFSE_1$	$MFSE_2$	HFSE
t_M (µm)	110	110	110	110
L_M (µm)	300	290	80	40
L (µm)	175	50	51	55
b (µm)	46	41	118	50
Sub-Bandwidth Frequencies (kHz)	0.1 - 0.5	0.5 - 1.25	1.25 - 5	5 - 8

Fig. 2.6(a) shows the sensitivity curves of the constrained four-bandwidth sensor for its four sensing elements (LFSE, $MFSE_1$, $MFSE_2$, and HFSE), and Fig. 2.6(b) shows the MDA_z curves. A comparison of the noise floor in dB SPL and dBA is shown in Appendix A.6. These results are qualitatively similar to the other sensor designs identified through our design investigation. The shaded regions indicate the frequency bandwidths of each sensing element defined by the lower and upper bounds. Accompanying electronics will be needed to filter signals outside the operational bandwidth of each sensing element and appropriately amplify signals to equalize sensitivities. All sensing elements meet the 20-phon noise floor over the sub-bandwidths (shown in Fig. 2.6(b)).

We estimate that all sensors identified through our design investigation procedure will be robust to loud sounds. For a pure tone acoustic input, according to the umbo motion data from Sachse et al. (2013) and Goode et al. (1996), 120 dB SPL causes approximate accelerations of 12.2 m/s^2 at 0.5 kHz, 51.6 m/s^2 at 1.25 kHz, 147.4 m/s^2 at 5 kHz, and 160 m/s^2 at 8 kHz. We select these frequencies because they are the upper frequency bounds of our constrained four-bandwidth sensor. Using the full analytical model from Section 2.3.3, we calculate the bending stresses experienced by each sensing element within the corresponding sub-bandwidth and under the above accelerations. We find that for the constrained four-bandwidth sensor, the maximum bending stresses occur as follows: the LFSE experiences 2.6 MPa at 0.5 kHz, the $MFSE_1$ experiences 6.4 MPa at 1.25 kHz, the

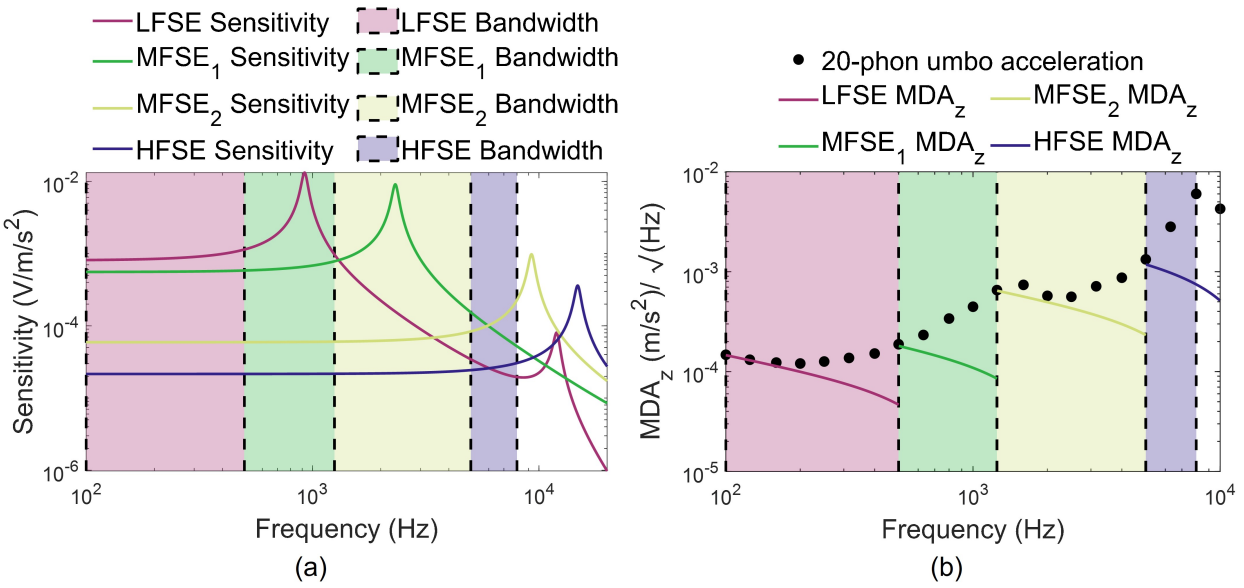

Figure 2.6: (a) Sensitivity response curves of constrained four-bandwidth design with four sensing elements (LFSE, MFSE_1, MFSE_2, and HFSE). (b) MDA_z curves for each sensing element calculated by converting spectral densities to acceleration levels with 1 Hz integration bandwidths. Shaded regions indicate sub-bandwidths of sensing elements.

MFSE_2 experiences 2.3 MPa at 5 kHz, and the HFSE experiences 1.0 MPa at 8 kHz. A similar trend is observed on all other sensor designs. All stresses are less than the tensile strength of the AlN piezoelectric material (approximately 230 MPa (Katz et al., 1993)). To avoid magnification of stresses at resonance, we can introduce mechanical stops in the final fabricated MEMs die to limit the motion of the sensing elements at frequencies greater than the upper frequency bounds. However, the effect of these mechanical stops on the A^{tot}_{MEMS} will need to be investigated. Furthermore, robustness to other loading cases, such as high-amplitude head impact and fatigue loading, would also need to be investigated for the final product design.

It is also important to note that the capacitive nature of these piezoelectric sensors will produce a high output impedance. In order to extract the sensor signal output, circuitry will be needed to facilitate impedance matching between the sensor and the data acquisition system. An alternative approach that eliminates the high impedance output is to use the

closed-circuit sensitivity where $V_{out} = 0$, and the sensitivity is calculated based on the current instead of the voltage. Appendix A.7 provides more details on the updated calculations for this approach.

2.5 Discussion and conclusions

To our knowledge, the unconstrained four-bandwidth design presented in this work (Table 2.1) is the smallest accelerometer in the literature that can meet the 20-phon noise floor over the 100 Hz – 8 kHz frequency bandwidth. To account for the manufacturability limitations, we constrain the four-bandwidth design to a single proof mass thickness (Table 2.2), which results in a larger MEMS die area compared to the unconstrained design but a still smaller area than the previously published dual-bandwidth two-proof-mass thickness design (Hake et al., 2023). Moreover, we show that for the material selection used in this study, the $N = 4$ design provides a lower bound on the total MEMS die area.

The MEMS form factor of the constrained four-bandwidth design would allow for the fabrication of a small packaged PCB with integrated circuitry and packaging included. Using the same specifications for PCB thickness, copper layers, and component spacing from PCB Universe (2024) as presented in Hake et al. (2023), we estimate that the new MEMS die along with a 1 mm $\times$ 1 mm integrated circuitry to process the output voltage signals (estimated from Yip et al. (2015)), will fit on a 2.2 mm $\times$ 2.5 mm $\times$ 1 mm PCB. We expect that the total mass of the packaged sensor, including a titanium cover (0.7 mm tall with 0.1 mm thick sidewalls), will be approximately 14 mg. For reference, we find that our size estimations and mass are comparable to a current commercial implantable transducer, the Vibrant Soundbridge, that is 2.3 mm long with a 1.8 mm diameter and with a mass of 25 mg (Schraven et al., 2016; Grégoire et al., 2018). However, for any middle ear sensor, smaller designs that allow for more ease during implantation and less loading to the ossicular chain are best.

As briefly mentioned in Section 2.3.5, topology optimization is beyond the scope of this thesis. The MEMS die dimensions presented in Fig. 2.5 were determined manually based on the calculation restrictions for A_{MEMS}^{tot} outlined in Section 2.4. Topology optimization is useful; however, the fabrication process of the multi-bandwidth designs needs to be studied first to better understand any thickness and aspect ratio limitations of the fabrication tools. With this knowledge, a better topology optimization can be carried out by accounting for these limitations.

We acknowledge that the complexity of the integrated circuitry increases with the number of frequency sub-bandwidths due to the filtering and amplification needed for each. Because of this increased complexity, we also investigated designs with fewer sensing elements ($N = 2$ and 3) using the single-proof-mass thickness constraint (Section 2.3.6.2). We found that the constrained dual bandwidth design has a 63% increase in MEMS die area compared to the constrained four-bandwidth design; however, the constrained three-bandwidth design only has a modest 7% increase. Hence, the three-bandwidth design is an attractive alternative option. The full dimensions of the constrained dual- and three-bandwidth designs can be found in Appendix A.5 in Tables A.1 and A.3.

Our design optimization approach includes a discretized and exhaustive search within our constrained design space, which would be classified as a brute-force optimization. For our goal of identifying MEMS sensor designs that minimize the sensor area, this design approach is sufficient with relatively fast computational times (e.g., unconstrained investigation: $N = 4$: 2 seconds, and the slowest $N = 11$: 6 minutes, and constrained investigation: $N = 3$: 25 minutes, and $N = 4$: 1 hour). These computational times are estimated by running the investigation on a laptop computer with an 11th Gen Intel Core i7 @ 2.80 GHz and 16 GB RAM. However, should faster timings be desired, alternative approaches to this investigation may be considered (Nocedal and Wright, 2006). Furthermore, in our design approach, we strategically limited our discretized parameters (t_{M_i}, L_{M_i}, and cross-over frequency values) which allowed us to use our discretized and exhaustive search approach with

relatively low computational cost (10µ m increments in t_{M_i} and L_{M_i}, and $N_f^{\max} = 20$ for the cross-over frequency values). However, we have investigated the use of 1µ m increments in t_{M_i} and L_{M_i} (approx. manufacturing limit) and $N_f^{\max} = 159$ (every 50 Hz between 100 Hz – 8 kHz). What we found using these finer resolutions in our parameters is that the resulting $N = 4$ design has a 3.75×10^{-8} m^2 sensor area (compared to the 3.94×10^{-8} m^2 reported in Table 2.1) and a 4.17×10^{-7} m^2 estimated MEMS die area (compared to the 4.28×10^{-7} m^2 reported in Table 2.1). Given the approximately 5% area difference between these two designs and that manufacturing tolerances (± 1 µm) may likely render these differences negligible, we consider the original discretization of the parameters satisfactory. Hence, our original discretized and exhaustive search satisfies the goal of our investigation in identifying multi-bandwidth designs without the need for finer resolution in the design parameters.

Furthermore, we assumed that the accelerometer would be placed on the umbo of the malleus, which is not readily accessible through standard CI surgery, requiring a wider opening of the facial recess (Cohen and Roland, 2006; Sanna et al., 2012a). Alternative attachment locations along the ossicular chain may provide significant advantages in decreasing the complexity of the surgical implantation and removing unnecessary risk. These locations could be explored.

In the case of a middle ear infection, fluid and inflammation are present in the middle ear and can lead to temporary conductive hearing loss, where the eardrum and ossicular chain vibrations are decreased. This hearing loss can range from 10 to 40 dB (Jamal et al., 2022). Decreased vibrations of the ossicular chain will result in a decrease in the sensitivity of the sensor. The sensitivity may be amplified to compensate for these decreased vibrations. However, this will also amplify the noise of the sensor. If a patient often experiences decreased ossicular vibrations, then it may be advantageous to redesign the sensor. This redesign would involve redefining the 20-phon noise target, $MDA_z^{\text{20-phon}}$, to account for the now decreased displacements experienced at the umbo. For a user with no conductive hearing loss, this

new redesigned sensor would exceed the 20-phon noise floor, but for a user with conductive hearing loss, the sensor would meet the 20-phon noise floor.

Lastly, there are other factors that may affect the overall packaged device volume, including outside noise sources, the piezoelectric material properties, and the piezoelectric bimorph thickness. Additional noise sources, such as the accompanying circuitry, will add noise to the system, which will increase the overall sensor MDA_z. This increase will require a redesign of the MEMS die to ensure that the 20-phon noise floor is met, which would increase the die size. Improvements in the piezoelectric material properties such as d_{31} and $\tan(\delta)$ will lead to a decrease in the area needed to meet a phon noise level (see Eq. 2.25) and thus, will lead to a decrease in the MDA_z as was shown in calculations by Hake et al. (2023) in the case of scandium-doped AlN (ScAlN). This decrease may balance with the MDA_z increase due to the integrated circuitry noise sources. We also anticipate that changes in the piezoelectric bimorph thickness (t_{piezo}) will affect the sensor design. We chose 0.5 µm because of our experience in depositing AlN films and achieving a particular d_{31} and $\tan(\delta)$ (Hake et al., 2021); however, a design investigation that further explores the effects of t_{piezo} may uncover smaller designs with equivalent or better performance.

CHAPTER 3

Investigating the Effect of the Piezoelectric Thickness, Loss Tangent, and Piezoelectric Coefficient on Three Canonical MEMS Cantilever Sensors

In the previous chapter, we explored the design of multi-bandwidth piezoelectric accelerometers for totally implantable auditory prostheses. One important assumption in that work was the use of fixed piezoelectric thickness ($t_{piezo} = 0.5$ µm) and fixed material properties ($\tan\delta$ and $\tilde{d}_{31}$). However, these parameters can impact the performance of a sensor (Kanno et al., 2023; Kumar et al., 2022), as we also noted in Section 2.5, and their effect has not been extensively explored in the literature. Specifically, understanding the effect of the piezoelectric thickness on the performance of a sensor can provide great insight into designing sensors that meet a desired sensitivity and noise floor while maintaining small form factors. The deposition of high-quality piezoelectric layers with a specific thickness depends on the fabrication tool, the thickness itself, and the substrate used. Thus, converging upon that specific piezoelectric thickness early in the sensor design process is crucial to prevent significant delays in manufacturing.

In the literature, we see examples of how the piezoelectric thickness of a design can affect performance. Fan et al. (2022) showed that there is a zinc oxide (ZnO) thickness that achieves

maximum sensitivity for a MEMS directional sound sensor with four cantilever beams. Wang et al. (2004) found that there is a lead zirconate titanate (PZT) thickness that maximizes the sensitivity in a microaccelerometer with a central proof mass and four suspended symmetric beams. Zhao et al. (2020) showed that the sensitivity increased proportionally with the piezoelectric thickness in a cantilever mass sensor with one piezoelectric layer bonded to an elastic rectangular layer. However, in these papers, the authors did not investigate how the noise and the final device size were impacted by altering the piezoelectric thickness. These metrics are of equal importance to the sensitivity when designing a sensor. Littrell (2010) presented an output energy optimization of an AlN bimorph cantilever sensor under uniform pressure that accounted for the device area and the noise floor. Littrell (2010) found the AlN and electrode thickness that maximized the output energy and advised that this thickness value depended on the material properties, especially $\tan\delta$ and $\tilde{d}_{31}$. In the same work, the author recommended that thinner AlN films led to better sensor performance. While Littrell (2010) presented the output energy optimization for a bimorph cantilever sensor under uniform pressure, they did not explicitly provide results on how the piezoelectric thickness and material properties affect the sensor area. Furthermore, other sensor designs could be investigated in a similar manner. Thus, we aim to bridge this gap by expanding on this analysis for different sensor designs and showing how the results vary depending on each design.

In this chapter, we develop an approach to investigate the effect of the piezoelectric thickness, $\tan\delta$, and $\tilde{d}_{31}$ on the sensor area of three single-bandwidth canonical AlN bimorph cantilever sensors: a cantilever under uniform pressure, a cantilever with a prescribed displacement at the free end, and a cantilever with a proof mass at the free end. The sensitivity and input-referred noise will serve as the primary performance metrics, and the sensor area will be the cost function to be minimized. The same constraints will apply in all sensor designs, including a target broadband full operational bandwidth of 100 Hz – 20 kHz and a set target noise floor. These constraints will be used to determine all other sensor dimen-

sions (cantilever length and width) while the piezoelectric thickness, $\tan\delta$, and $\tilde{d}_{31}$ of each design are varied. Please note that the frequency bandwidth of interest in this chapter is broader than what was discussed in Chapter 2. This is because here we focus on the effect of geometry and material properties on sensors for general applications, extending beyond the implantable auditory prosthesis applications. However, it is important to mention that all sensors explored in this chapter have or are currently being used as potential implantable sensors for totally implantable auditory prostheses (Yeiser et al., 2024; Hake et al., 2023; Bruschini et al., 2009). Thus, the results of this chapter can inform future sensor designs for auditory prostheses.

3.1 General optimization problem

In the following sections, we seek to investigate the effect of the piezoelectric thickness, $\tan\delta$, and $\tilde{d}_{31}$ on three single-bandwidth canonical sensor designs and minimize each sensor area, A_S: (1) cantilever under uniform pressure, (2) cantilever with a prescribed displacement at the free end, and (3) cantilever with a proof mass at the free end. Similar to the last chapter, all designs are comprised of a cantilever plate with two identical AlN layers intermixed with three electrode layers (on the top, in the middle, and on the bottom). We neglect the effect of the electrode layers on the mechanics as they are thin compared to the piezoelectric layers. Once again, if the electrode thickness is non-negligible, then this effect can be included in the calculation of the bending stiffness (Krommer, 2001; Littrell and Grosh, 2012). Furthermore, the electrode lengths may be optimized for each sensor design to achieve a minimum noise floor, as was presented in Littrell (2010) for a sensor under uniform pressure. However, this electrode-length optimization does not impact the effect of the piezoelectric layer thickness, $\tan\delta$, or $\tilde{d}_{31}$ on the sensor area of any design, and thus, it is not presented in this work. Lastly, we assume that the piezoelectric material is in-plane isotropic, and we use the plane-strain material property equivalents for all calculations.

In our investigation, we vary the piezoelectric plate thickness of each layer, t_{piezo}, from 0.25 µm to 2 µm in 0.25 µm increments. We chose these particular dimensions because there is evidence in the literature that thin (0.25 µm) AlN layers are possible (Fiedler et al., 2021), and any thicker (>2 µm) layers are costly and require longer deposition times. For reference, the University of Michigan Lurie Nanofabrication Facility charges $179 per hour to use the Endeavor M1 for sputter-deposition of high-quality AlN (LNF, 2025b). The deposition rate is approximately 10 Å thickness per second, and thus, a single layer thickness of 2 µm requires approximately 35 minutes (LNF, 2025a). In addition, since both $\tan\delta$ and $\tilde{d}_{31}$ degrade as the piezoelectric thickness decreases (Littrell, 2010), we also adjust these material properties based on the varied piezoelectric thickness using data presented in Martin et al. (2004). For more information on the $\tan\delta$ and $\tilde{d}_{31}$ values see Appendix B.1 and Littrell (2010).

For our target sensor performance, all designs are constrained to operate with approximately constant sensitivity under the same full operational bandwidth of 100 Hz – 20 kHz, where each sensor has a lower ($f_\alpha = 100$ Hz) and an upper ($f_\beta = 20$ kHz) frequency bound. In addition, for all results presented in this chapter, we normalize to the target input-referred noise or the minimum detectable signal of each system, as we will describe in the following sections. The minimum detectable signal is a lower limit of the sensor noise floor, and any additional circuitry will add noise to the overall system. Therefore, for each sensor design, we will formally state the optimization problem, which includes minimizing the sensor area subject to maintaining constant sensitivity over the target operational bandwidth and meeting a desired target noise floor. The sensor area will be shown to be a function of geometry and material properties.

3.2 Sensor under uniform pressure

In this section, we recapitulate and extend upon the analysis presented in Littrell (2010). The design layout of the sensor under uniform pressure is shown in Fig. 3.1. An output voltage (V_{out}) is generated when the structure is subjected to a uniform pressure (P, shown in pink). All variables associated with this sensor's dimensions are labeled. The sensor area of this design is defined as $A_S^{\mathrm{P}} = L \cdot b$, where L is the piezoelectric length and b is the width. We also assume that the bottom of the sensor is shielded from the acoustic field (e.g., by the package). Next, we show how enforcing the optimization constraints allows us to determine L and b and investigate the effect of the piezoelectric thickness, $\tan\delta$, and $\tilde{d}_{31}$ on the sensor area.

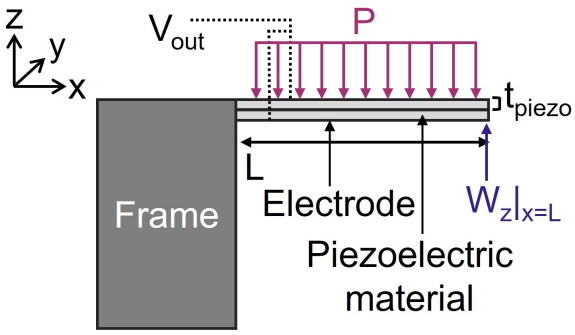

Figure 3.1: Side view of a sensor comprised of one piezoelectric cantilever bimorph plate. The design consists of two AlN layers (piezoelectric material) of length L, single piezoelectric layer thickness t_{piezo}, and width b (into the page, not shown). Three electrodes are on the bimorph's top, middle, and bottom. The structure is subjected to either a uniform pressure, P (shown in pink), that extends over the full length of the cantilever, or a displacement, W_z (shown in blue), at the free end of the cantilever ($x = L$). In response to P or W_z, the piezoelectric layers will generate an output voltage, V_{out}. Not to scale.

3.2.1 Full analytical model

The full analytical model used to simulate the response of the vibrating sensor under uniform pressure is presented in Littrell (2010) and has the following non-homogeneous

governing equation for transverse deflection:

$$\overline{EI}\frac{d^4W(x)}{dx^4} - \omega^2\rho_{AlN}AW(x) = -Pb \ . \tag{3.1}$$

The solution to Eq. 3.1 will have a homogeneous and a particular solution: $W(x) = W_H(x) + W_P(x)$. The homogeneous solution is the same as Eq. 2.5, whereas the particular solution is $W_P(x) = \frac{Pb}{\overline{EI}\gamma^4}$. Hence, the solution to Eq. 3.1 can be written as:

$$W(x) = C_1\sin(\gamma x) + C_2\cos(\gamma x) + C_3\sinh(\gamma x) + C_4\cosh(\gamma x) + \tfrac{Pb}{\overline{EI}\gamma^4} \ , \tag{3.2}$$

where the coefficients $C_1 - C_4$ are determined using the boundary conditions defined for this vibrating system. At $x = 0$, where the piezoelectric beam connects to the silicon frame (Fig. 3.1), the prescribed displacement in the z-direction and the slope condition are:

$$W(0) = 0 \ , \tag{3.3}$$

$$\tfrac{dW(0)}{dx} = 0 \ . \tag{3.4}$$

At the free end of the cantilever ($x = L$), the bending moment and force boundary conditions are:

$$\overline{EI}\tfrac{d^2W(L)}{dx^2} = M_e \ , \tag{3.5}$$

$$\overline{EI}\tfrac{d^3W(L)}{dx^3} = 0 \ , \tag{3.6}$$

where M_e is the electrical moment due to the stacked identical piezoelectric layers connected in parallel, and the derivation is provided in Krommer (2001) and Littrell and Grosh (2012) (Eq. 2.13).

3.2.1.1 Sensitivity

The sensitivity of the sensor ($S_{\mathrm{P}}(f)$) as a function of frequency is the transfer function between the output voltage and the input uniform pressure, where $S_{\mathrm{P}}(f) = V_{out}(f)/P$ in units of V/Pa, and V_{out} is also a function of frequency.

The full analytical model can be used to determine the open-circuit sensitivity (where the total charge generated from the piezoelectric layers is zero, $Q^c = 0$). All boundary conditions from Eqs. 3.3–3.6 and the charge output equation (Eq. 2.19) are assembled in a matrix format with V_{out} and the corresponding coefficients $C_1 - C_4$ from Eq. 3.2:

$$\begin{bmatrix} 0 & 1 & 0 & 1 & 0 \\ \gamma & 0 & \gamma & 0 & 0 \\ -\gamma^2\overline{EI}\sin(\gamma L) & -\gamma^2\overline{EI}\cos(\gamma L) & \gamma^2\overline{EI}\sinh(\gamma L) & \gamma^2\overline{EI}\cosh(\gamma L) & \alpha \\ -\gamma^3\overline{EI}\cos(\gamma L) & \gamma^3\overline{EI}\sin(\gamma L) & \gamma^3\overline{EI}\cosh(\gamma L) & \gamma^3\overline{EI}\sinh(\gamma L) & 0 \\ \alpha\gamma\cos(\gamma L) & -\alpha\gamma\sin(\gamma L) & \alpha\gamma\cosh(\gamma L) & \alpha\gamma\sinh(\gamma L) & C \end{bmatrix} \begin{bmatrix} C_1 \\ C_2 \\ C_3 \\ C_4 \\ V_{out} \end{bmatrix} = \begin{bmatrix} -\frac{Pb}{\overline{EI}\gamma^4} \\ 0 \\ 0 \\ 0 \\ 0 \end{bmatrix} \tag{3.7}$$

where $\alpha = b\tilde{d}_{31}t_{piezo}/\tilde{s_{11}}^E$. We normalize the solution to P.

3.2.2 Assumed-mode solution to full analytical model

Although the full analytical model provides a good approach to modeling $S_{\mathrm{P}}(f)$, it does not readily allow for the investigation of the effect of piezoelectric thickness, $\tan\delta$, and $\tilde{d}_{31}$. An assumed-mode solution can allow for this investigation and provide a closed-form expression of $S_{\mathrm{P}}(f)$ for low frequencies.

The assumed-mode solution to a statically bending beam under uniform pressure with transverse displacement is given by (Gere and Goodno, 2012):

$$W(x) = \tilde{C}_1x^3 + \tilde{C}_2x^2 + \tilde{C}_3x + \tilde{C}_4 - \frac{Pb}{24\overline{EI}}x^4 \ . \tag{3.8}$$

Using the boundary conditions in Eqs. 3.3–3.6 and 2.19, we can assemble a new matrix with

V_{out} and coefficients $\tilde{C}_1$–$\tilde{C}_4$:

$$\begin{bmatrix} 0 & 0 & 0 & 1 & 0 \\ 0 & 0 & 1 & 0 & 0 \\ 6\overline{EI}L & 2\overline{EI} & 0 & 0 & \alpha \\ 6\overline{EI} & 0 & 0 & 0 & 0 \\ \alpha(3L^2) & \alpha(2L) & \alpha & 0 & C \end{bmatrix} \begin{bmatrix} \tilde{C}_1 \\ \tilde{C}_2 \\ \tilde{C}_3 \\ \tilde{C}_4 \\ V_{out} \end{bmatrix} = \begin{bmatrix} 0 \\ 0 \\ \frac{PbL^2}{2} \\ PbL \\ \frac{PbL^3\alpha}{6\overline{EI}} \end{bmatrix} \tag{3.9}$$

and once again, we normalize to P.

To derive the closed-form expression for $S_{\mathrm{P}}(f)$ at low frequencies, we solve for V_{out} in Eq. 3.9 and divide it by the uniform pressure, P, to obtain the following low-frequency sensitivity approximation:

$$\lim_{\omega \to 0} S_P(f) = \left| -\frac{1}{4} \frac{L^2 \tilde{d}_{31} \tilde{s}_{11}^E}{t_{piezo}(\tilde{d}_{31}^2 - 2\tilde{\epsilon}_{33}^S \tilde{s}_{11}^E)} \right|, \tag{3.10}$$

This equation shows the dependence of $S_{\mathrm{P}}(f)$ on the geometric and material properties, including t_{piezo} and $\tilde{d}_{31}$.

3.2.2.1 Input-referred noise: minimum detectable pressure

The noise floor of this vibrating system is defined as the minimum detectable signal that the sensor can detect. For this piezoelectric sensor, the theoretical value of the minimum detectable pressure (MDP) is calculated as $MDP = |\sqrt{\overline{v_n^2}}/S_{\mathrm{P}}(f)|$ with units of Pa/$\sqrt{\mathrm{Hz}}$, where $\overline{v_n^2}$ is the sensor noise spectral density due to the dielectric losses in the piezoelectric material in 1 Hz bandwidths; calculated using the Johnson noise equation (Eq. 2.24). Using the closed-form expression for $S_{\mathrm{P}}(f)$ from Eq. 3.10 and the calculated $\overline{v_n^2}$, we derive an approximate expression for the theoretical MDP due to an applied uniform pressure:

$$MDP = \left| \sqrt{8k_BT} \quad \underbrace{\frac{1}{\sqrt{\omega}}}_{\text{Frequency}} \quad \underbrace{\frac{(2\tilde{d}_{31}^2 - 4\tilde{\epsilon}_{33}^S \tilde{s}_{11}^E)\sqrt{\tan\delta}}{\tilde{d}_{31}\tilde{s}_{11}^E\sqrt{\tilde{\epsilon}_{33}^S}}}_{\text{Material properties}} \quad \underbrace{\frac{\sqrt{t_{piezo}^3}}{\sqrt{bLL^2}}}_{\text{Sensing plate dimensions}} \right| . \tag{3.11}$$

Equation 3.11 shows the dependence of the input-referred noise on the piezoelectric thickness, $\tan\delta$, and $\tilde{d}_{31}$. It can also be used to derive an explicit expression for the piezoelectric width, b, which we will show in Section 3.2.3.

3.2.2.2 Resonant frequency approximation

We recall from Section 3.1 that each sensor must meet the full operational bandwidth of 100 Hz to 20 kHz and have constant sensitivity over that bandwidth. As in Section 2.3.4.3, we can use the resonant frequency (f_{res}) of the sensor to define the upper frequency bound, f_β, and maintain approximately constant sensitivity over the operational bandwidth.

We set f_β as the frequency at which there is a 3 dB increase compared to the low-frequency asymptote ($f_\beta = f_{3\text{dB}}$). We can estimate $f_{3\text{dB}}$ using f_{res}, where $f_{3\text{dB}} \approx f_{\text{res}}/1.85$. This relationship was derived using the magnification factor equation (MF), where $MF \approx 1/(1-(f_{3\text{dB}}/f_{\text{res}})^2)$ and $MF = 10^{3/20}$ for a 3 dB increase. Therefore, the constant sensitivity constraint depends on f_{res}.

The first resonance frequency for the vibrating sensor can be found from the following equation (Graff, 1975):

$$f_{\text{res}} = \frac{1.875^2}{2\pi L^2}\sqrt{\frac{\overline{EI}}{\rho_{AlN}A}} , \tag{3.12}$$

where recall $A = 2t_{piezo}b$ is the cross-section area of the beam and $\overline{EI}$ is the effective beam bending stiffness that accounts for the piezoelectricity calculated as $\overline{EI} = \frac{bt_{piezo}^3}{\tilde{s}_{11}^E}(\frac{2}{3} + \frac{1}{6}\frac{\tilde{d}_{31}^2}{\tilde{\epsilon}_{33}^S\tilde{s}_{11}^E})$ (Krommer, 2001; Littrell and Grosh, 2012). It is important to note that the width, b, can be entirely canceled out in Eq. 3.12, and it does not influence f_{res}.

This equation provides an explicit expression of the piezoelectric length, L, using the constraint of constant sensitivity, which depends on the upper frequency bound, f_β. Fur-

thermore, it shows that L, t_{piezo}, and $\tilde{d}_{31}$ are related by the same constraint. This relation becomes important when casting the optimization problem to investigate the piezoelectric thickness effect, which will be discussed in the next section.

3.2.3 Casting the optimization problem

Using the relations presented in the previous sections, we can formally state the optimization problem for this sensor design to reflect the effect of the piezoelectric thickness, $\tan\delta$, and $\tilde{d}_{31}$ on the sensor area. First, in Section 3.2.2.2 we showed that there exists an explicit relation between L, t_{piezo}, $\tilde{d}_{31}$, and f_β (since $f_\beta \approx f_{\text{res}}/1.85$) that constrains the design space. Second, we can use the noise-floor constraint presented in Section 3.2.2.1 to derive an explicit expression for b. As MDP monotonically decreases over the frequency bandwidth (Eq. 3.11), we can approximate the enforcement of the noise-floor constraint by ensuring that the target noise floor (MDP^{Target} in Pa/$\sqrt{\text{Hz}}$) is met at the lower frequency bound (f_α =100 Hz). Hence, using Eq. 3.11 and the target noise floor at f_α, we can write b as an explicit function of f_α, L, t_{piezo}, $\tan\delta$, and $\tilde{d}_{31}$:

$$b = \left(\left| \sqrt{8k_BT} \quad \underbrace{\frac{1}{\sqrt{2\pi f_\alpha}}}_{\text{Lower frequency bound}} \quad \frac{(2\tilde{d}_{31}^2 - 4\tilde{\epsilon}_{33}^S \tilde{s_{11}}^E)\sqrt{\tan\delta}}{\tilde{d}_{31}\tilde{s}_{11}^E\sqrt{\tilde{\epsilon}_{33}^S}} \right. \right. \\ \left. \left. \times \frac{\sqrt{t_{piezo}^3}}{\sqrt{L}L^2} \quad \underbrace{\frac{1}{MDP^{\text{Target}}}}_{\text{Target noise floor at } f_\alpha} \right| \right)^2. \quad (3.13)$$

To normalize for the target noise floor, we rearrange Eq. 3.13 to eliminate the term $(MDP^{\text{Target}})^2$. We introduce a normalized width variable, b^*, where $b^* = b \times (MDP^{\text{Target}})^2$ in units of mPa^2/Hz. Thus, the normalized sensor area is defined as $A_S^{\text{P}} = L \cdot b^*$ in units of m^{2}Pa^2/Hz.

Now that L and b^* are expressed as functions of the other variables subject to the design constraints discussed previously, and the sensor area, A_S^{P} is defined, we can cast our

optimization problem as:

$$\min(A_S^{\mathrm{P}}(\mathbf{t_{piezo}}, \tan\delta, \tilde{d}_{31})) \tag{3.14}$$

$$\text{subject to } \begin{cases} \text{constant sensitivity over 100 Hz – 20 kHz} \\ \text{meet } MDP^{\text{Target}} \text{ over 100 Hz – 20 kHz} \end{cases}$$

where $\mathbf{t_{piezo}}$ is the vector corresponding to the piezoelectric thickness, and $\tan\delta$ and $\tilde{d}_{31}$ are varied based on the piezoelectric thickness.

3.2.4 Results

All results presented in this section are calculated assuming a plane-strain constitutive hypothesis. The AlN material properties used are shown in Table 3.1 and will be used for all results presented in this chapter. Furthermore, as mentioned in Section 3.1, t_{piezo} is varied from 0.25 µm to 2 µm in 0.25 µm increments, and $\tan\delta$ and $\tilde{d}_{31}$ are varied based on the piezoelectric thickness using data from Martin et al. (2004).

Table 3.1: AlN material properties assuming a plane-strain constitutive hypothesis (Hake et al., 2023)

Property	**Value**
ρ_{AlN}	3.26×10^3 (kg/m^3)
$\tilde{s}_{11}^E$	2.6×10^{-12} (m^2/N)
$\tilde{\epsilon}_{33}^T$	$10.0 \cdot 8.854 \times 10^{-12}$ (F/m)
Varied $\tan\delta$ and $\tilde{d}_{31}$	Extracted from Martin et al. (2004)
Constant $\tilde{d}_{31}$	-2.5×10^{-12} (C/N)
Constant $\tan\delta$	0.0015 (Hake et al., 2021)

Figure 3.2 shows the relationship between the normalized sensor area, A_S^{P}, and t_{piezo} using varied $\tan\delta$ and $\tilde{d}_{31}$ properties (solid line). For comparison, we also present the relationship if constant $\tan\delta$ and $\tilde{d_{31}}$ were used instead (dashed line), where the property values are given in Table 3.1. We observe that if we assume constant material properties, A_S^{P} increases linearly

with t_{piezo} (approx. $A_S^{\mathrm{P}} \propto t_{piezo}$), whereas when we account for the thickness-dependence of $\tan\delta$ and $\tilde{d}_{31}$, we observe that A_S^{P} remains approximately constant. It is important to note that the qualitative behavior between A_S^{P} and t_{piezo} remains the same regardless of the target operational bandwidth. This is evident when examining Eqs. 3.12 and 3.13, where we see that both the upper and lower frequency bounds (f_β and f_α) are used to calculate L and b, respectively. Changing either frequency bound will scale the results by some constant, but will not affect the qualitative behavior.

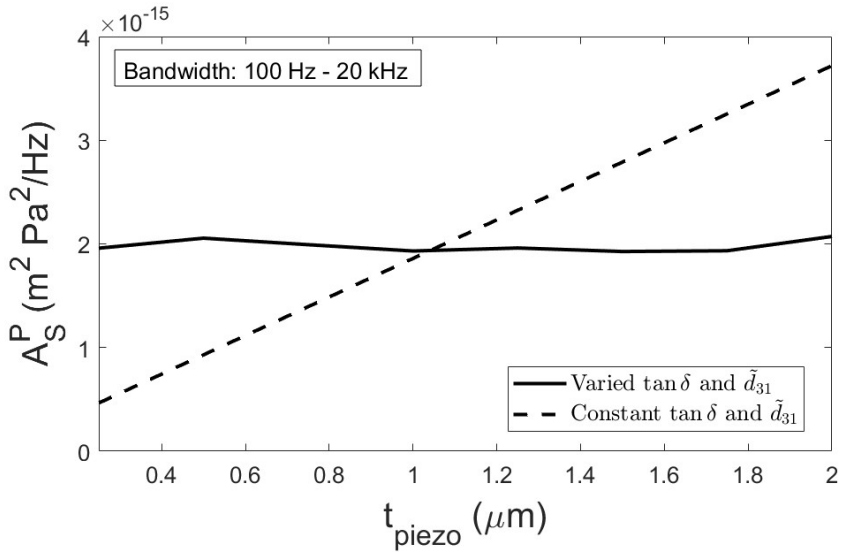

Figure 3.2: Relationship between normalized A_S^{P} and t_{piezo} using varied and constant $\tan\delta$ and $\tilde{d}_{31}$.

3.3 Sensor with prescribed displacement

The design layout of the sensor with a prescribed displacement at the free end is shown in Fig. 3.1. An output voltage (V_{out}) is generated when the structure is subjected to a transverse displacement at $x = L$ (W_x, shown in blue). The sensor area of this design is defined as $A_S^{\mathrm{D}} = L \cdot b$. Next, we will show how to determine L and b to investigate the effect of the piezoelectric thickness, $\tan\delta$, and $\tilde{d}_{31}$ on the sensor area.

3.3.1 Full analytical model

The full analytical model used to simulate the response of the vibrating sensor with a prescribed displacement at $x = L$ uses the same governing equation for transverse deflection as Eq. 2.3 and has the same solution for $W(x)$ as Eq. 2.5. However, the boundary conditions of this sensor are different. We use the fixed condition for $x = 0$ and the pinned condition for $x = L$ as shown below (Graff, 1975):

$$W(0) = 0 \ , \tag{3.15}$$

$$\tfrac{dW(0)}{dx} = 0 \ , \tag{3.16}$$

$$W(L) = W_z \ , \tag{3.17}$$

$$\overline{EI}\tfrac{d^2W(L)}{dx^2} = M_e \ , \tag{3.18}$$

where M_e is provided in Krommer (2001) and Littrell and Grosh (2012) and is the same as Eq. 2.13.

3.3.1.1 Sensitivity

The sensitivity of the sensor ($S_{\mathrm{D}}(f)$) as a function of frequency is the transfer function between the output voltage and the input prescribed displacement at $x = L$, where $S_{\mathrm{D}}(f) = V_{out}(f)/W_z$ in units of V/m, and V_{out} is also a function of frequency.

The full analytical model can be used to determine the open-circuit sensitivity ($Q^c = 0$). All boundary conditions from Eqs. 3.15–3.18 and the charge output equation (Eq. 2.19) are assembled in a matrix format with V_{out} and the corresponding coefficients $C_1 - C_4$ from

$W(x)$:

$$\begin{bmatrix} 0 & 1 & 0 & 1 & 0 \\ \gamma & 0 & \gamma & 0 & 0 \\ -\gamma^2\overline{EI}\sin(\gamma L) & -\gamma^2\overline{EI}\cos(\gamma L) & \gamma^2\overline{EI}\sinh(\gamma L) & \gamma^2\overline{EI}\cosh(\gamma L) & \alpha \\ \sin(\gamma L) & \cos(\gamma L) & \sinh(\gamma L) & \cosh(\gamma L) & 0 \\ \alpha\gamma\cos(\gamma L) & -\alpha\gamma\sin(\gamma L) & \alpha\gamma\cosh(\gamma L) & \alpha\gamma\sinh(\gamma L) & C \end{bmatrix} \begin{bmatrix} C_1 \\ C_2 \\ C_3 \\ C_4 \\ V_{out} \end{bmatrix} = \begin{bmatrix} 0 \\ 0 \\ 0 \\ W_z \\ 0 \end{bmatrix} \tag{3.19}$$

We normalize all results to W_z.

3.3.2 Assumed-mode solution to full analytical model

The assumed-mode solution is used to derive a closed-form expression of $S_{\mathrm{D}}(f)$ for low frequencies. Equation 2.21 provides the solution to a statically bending beam with a prescribed displacement at the free end. Using the boundary conditions in Eqs. 3.15–3.18 and 2.19, we can assemble a new matrix with V_{out} and coefficients $\tilde{C}_1$–$\tilde{C}_4$:

$$\begin{bmatrix} 0 & 0 & 0 & 1 & 0 \\ 0 & 0 & 1 & 0 & 0 \\ 6\overline{EI}L & 2\overline{EI} & 0 & 0 & \alpha \\ L^3 & L^2 & L & 1 & 0 \\ \alpha(3L^2) & \alpha(2L) & \alpha & 0 & C \end{bmatrix} \begin{bmatrix} \tilde{C}_1 \\ \tilde{C}_2 \\ \tilde{C}_3 \\ \tilde{C}_4 \\ V_{out} \end{bmatrix} = \begin{bmatrix} 0 \\ 0 \\ 0 \\ W_z \\ 0 \end{bmatrix} \tag{3.20}$$

and once again, we normalize to W_z.

To derive the closed-form expression for $S_{\mathrm{D}}(f)$ at low frequencies, we solve for V_{out} in Eq. 3.20 and divide it by the prescribed displacement, W_z, to obtain the following low-frequency sensitivity approximation:

$$\lim_{\omega\to 0} S_{\mathrm{D}}(f) = \left| -\frac{3t_{piezo}^2\tilde{d}_{31}(\tilde{d}_{31}^2 + 4\tilde{\epsilon}_{33}^S\tilde{s}_{11}^E)}{L^2(\tilde{d}_{31}^2 + 16\tilde{\epsilon}_{33}^S\tilde{s}_{11}^E)(\tilde{\epsilon}_{33}^S\tilde{s}_{11}^E)} \right|, \tag{3.21}$$

This equation shows the dependence of $S_{\mathrm{D}}(f)$ on the geometric and material properties, including t_{piezo} and $\tilde{d}_{31}$.

3.3.2.1 Input-referred noise: minimum detectable displacement

The noise floor of this vibrating system is the minimum detectable displacement (MDD). For this piezoelectric sensor, the theoretical value of MDD is calculated as $MDD = |\sqrt{\overline{v_n^2}}/S_{\mathrm{D}}(f)|$ with units of $\mathrm{m}/\sqrt{\mathrm{Hz}}$. Using the closed-form expression for $S_{\mathrm{D}}(f)$ from Eq. 3.21 and the calculated $\overline{v_n^2}$ (Eq. 2.24), we derive an approximate expression for the theoretical MDD due to prescribed displacement at $x = L$:

$$MDD = \left| \frac{\sqrt{2k_BT}}{3} \underbrace{\frac{1}{\sqrt{\omega}}}_{\text{Frequency}} \underbrace{\frac{(\tilde{\epsilon}_{33}^S \tilde{s}_{11}^E)(\tilde{d}_{31}^2 + 16\tilde{\epsilon}_{33}^S \tilde{s}_{11}^E)\sqrt{\tan\delta}}{\tilde{d}_{31}(\tilde{d}_{31}^2 + 4\tilde{\epsilon}_{33}^S \tilde{s}_{11}^E)\sqrt{\tilde{\epsilon}_{33}^S}}}_{\text{Material properties}} \underbrace{\frac{\sqrt{L^3}}{\sqrt{t_{piezo}^3}\sqrt{b}}}_{\text{Sensing plate dimensions}} \right|. \tag{3.22}$$

Equation 3.22 shows the dependence of the input-referred noise on t_{piezo}, $\tan\delta$, and $\tilde{d}_{31}$. It can also be used to derive an explicit expression for b, which we will show in Section 3.3.3.

3.3.2.2 Resonant frequency approximation

As in Section 3.2.2.2, we can use the f_{res} of the sensor to define f_β and maintain approximately constant sensitivity over the operational bandwidth (100 Hz – 20 kHz). We set f_β as the frequency at which there is a 3 dB change compared to the low-frequency asymptote ($f_\beta = f_{\mathrm{3dB}}$). We can estimate f_{3dB} using f_{res}, where $f_{\mathrm{3dB}} \approx f_{\mathrm{res}}/2.46$. Note that this approximation is different from what was outlined in Section 3.2.2.2. This is because the sensor experiences anti-resonance before resonance, and thus we utilize the full analytical model (Section 3.3.1) to obtain the relationship between f_{3dB} and f_{res}.

The first resonance frequency for the vibrating sensor can be found from the following

equation (Graff, 1975):

$$f_{\text{res}} = \frac{3.927^2}{2\pi L^2}\sqrt{\frac{\overline{EI}}{\rho_{AlN} A}}\ , \tag{3.23}$$

where recall $A = 2t_{piezo}b$ and $\overline{EI} = \frac{bt_{piezo}^3}{\tilde{s}_{11}^E}(\frac{2}{3} + \frac{1}{6}\frac{\tilde{d}_{31}^2}{\tilde{\epsilon}_{33}^S \tilde{s}_{11}^E})$. It is important to note that once again the width, b, can be entirely canceled out in Eq. 3.23, and it does not influence f_{res}.

This equation provides an explicit expression of L using the constraint of constant sensitivity, which depends on f_β, t_{piezo}, and $\tilde{d}_{31}$. This relation becomes important when casting the optimization problem, which will be discussed in the next section.

3.3.3 Casting the optimization problem

We use the relations presented in the previous sections to cast the optimization problem for this sensor design. First, in Section 3.3.2.2 we showed that there exists an explicit relation between L, t_{piezo}, $\tilde{d}_{31}$, and f_β (since $f_\beta \approx f_{\text{res}}/2.46$) that constrains the design space. Second, we can use the noise-floor constraint presented in Section 3.3.2.1 to derive an explicit expression for b. As MDD monotonically decreases over the frequency bandwidth (Eq. 3.22), we can approximate the enforcement of the noise-floor constraint by ensuring that the target noise floor (MDD^{Target} in m/$\sqrt{\text{Hz}}$) is met at the lower frequency bound (f_α =100 Hz). Hence, using Eq. 3.22 and the target noise floor at f_α, we can write b as an explicit function of f_α, L, t_{piezo}, $\tan\delta$, and $\tilde{d}_{31}$:

$$b = \left(\left| \frac{\sqrt{2k_BT}}{3} \underbrace{\frac{1}{\sqrt{2\pi f_\alpha}}}_{\text{Lower frequency bound}} \frac{(\tilde{\epsilon}_{33}^S \tilde{s}_{11}^E)(\tilde{d}_{31}^2 + 16\tilde{\epsilon}_{33}^S \tilde{s}_{11}^E)\sqrt{\tan\delta}}{\tilde{d}_{31}(\tilde{d}_{31}^2 + 4\tilde{\epsilon}_{33}^S \tilde{s}_{11}^E)\sqrt{\tilde{\epsilon}_{33}^S}} \times \frac{\sqrt{L^3}}{\sqrt{t_{piezo}^3}} \underbrace{\frac{1}{MDD^{\text{Target}}}}_{\text{Target noise floor at } f_\alpha} \right| \right)^2 . \tag{3.24}$$

To normalize for the target noise floor, we rearrange Eq. 3.24 to eliminate the term $(MDD^{\text{Target}})^2$. We introduce the normalized width variable, b^*, where

$b^* = b \times (MDD^{\text{Target}})^2$ in units of m^3/Hz. Thus, the normalized sensor area is defined as $A_S^{\text{D}} = L \cdot b^*$ in units of m^4/Hz and we can, once again, cast our optimization problem to account for the geometric and material constraints on L and b^* as:

$$\min(A_S^{\text{D}}(\mathbf{t_{piezo}}, \tan\delta, \tilde{d}_{31})) \tag{3.25}$$

$$\text{subject to } \begin{cases} \text{constant sensitivity over 100 Hz – 20 kHz} \\ \text{meet } MDD^{\text{Target}} \text{ over 100 Hz – 20 kHz} \end{cases}$$

3.3.4 Results

Figure 3.3 shows the relationship between the normalized sensor area, A_S^{D}, and t_{piezo} using constant and varied $\tan\delta$ and $\tilde{d}_{31}$ properties. We observe that for both constant and varied material properties, A_S^{D} decreases with t_{piezo} (approx. $A_S^{\text{D}} \propto 1/t_{piezo}$), however this decrease occurs at different slopes. For example, assuming the material properties vary according to Martin et al. (2004), we can obtain an 89% reduction in the sensor area by increasing t_{piezo} to 0.75 µm from 0.25 µm. While assuming constant material properties, we obtain a 67% reduction. It is also important to note that the qualitative behavior between A_S^{D} and t_{piezo} remains the same regardless of the target operational bandwidth. This is evident when examining Eq. 3.23 and 3.24, where changing either the upper or lower frequency bound will scale the calculations of L and b by some constant, but will not affect the qualitative behavior.

3.4 Sensor with proof mass - accelerometer

The design layout of the accelerometer with a proof mass is presented in Section 2.3.2. Furthermore, the full analytical model and the assumed-mode solution to that model were also presented in Sections 2.3.3 and 2.3.4. The sensor area of this design is defined as $A_S^{\text{AXL}} = (L + L_M) \cdot b$, where L_M is the length of the proof mass. For this design investigation,

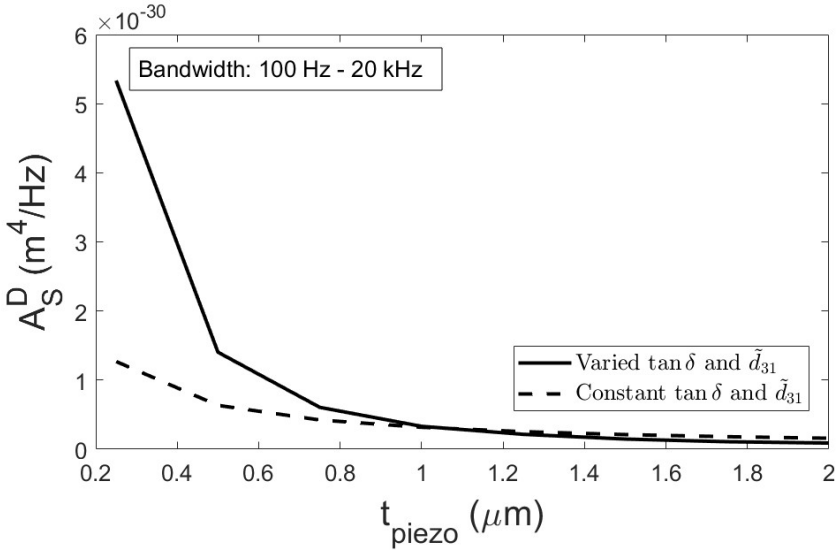

Figure 3.3: Relationship between normalized A_S^{D} and t_{piezo} using varied and constant $\tan\delta$ and $\tilde{d}_{31}$.

we also vary the proof mass thickness, t_M, and L_M from 10 µm to 300 µm each in 10 µm increments. Next, we will revise how we determine L and b to cast the optimization problem and investigate the influence of t_{piezo}, $\tan\delta$, and $\tilde{d}_{31}$.

3.4.1 Casting the optimization problem

In Section 2.3.4.3, we introduced an implicit relation between L, L_M, t_M, f_β (since $f_\beta \approx f_{\mathrm{res}}/1.85$), t_{piezo}, and $\tilde{d}_{31}$ using the constant sensitivity constraint. Note that this is unlike the previous two sensor designs, in which an explicit relation could be derived. In addition, in Section 2.3.5, we derived an explicit expression for b that is adapted as follows:

$$b = \left(\left| \sqrt{\frac{8k_BT}{9}} \underbrace{\frac{1}{\sqrt{2\pi f_\alpha}}}_{\text{Lower frequency bound}} \frac{(2\tilde{d}_{31}^2 - \tilde{\epsilon}_{33}^S \tilde{s}_{11}^E)\sqrt{\tan\delta}}{\tilde{d}_{31}\tilde{s}_{11}^E \rho_M \sqrt{\tilde{\epsilon}_{33}^S}} \times \frac{\sqrt{t_{piezo}^3}}{L_M t_M \sqrt{L}(L+L_M)} \underbrace{\frac{1}{MDA^{\mathrm{Target}}}}_{\text{Target noise floor at } f_\alpha} \right| \right)^2. \quad (3.26)$$

where MDA^{Target} is the target noise floor at the low frequency bound. This equation provides a relation between the target noise floor, b, L_M, t_M, f_α, t_{piezo}, $\tan\delta$, and $\tilde{d}_{31}$.

We can normalize for the target noise floor by rearranging Eq. 3.26 to eliminate the noise term $(MDA^{\text{Target}})^2$. We introduce the b^* variable, where $b^* = b \times (MDA^{\text{Target}})^2$ in units of $(\text{m}^3/\text{s}^4)/\text{Hz}$. Thus, the normalized sensor area is defined as $A_S^{\text{AXL}} = (L + L_M) \cdot b^*$ in units of $(\text{m}^4/\text{s}^4)/\text{Hz}$.

Now that we have expressed L and b^* as functions of other variables, we can cast the optimization problem:

$$\min(A_S^{\text{AXL}}(\mathbf{L_M}, \mathbf{t_M}, \mathbf{t_{piezo}}, \tan\delta, \tilde{d}_{31})) \tag{3.27}$$

$$\text{subject to } \begin{cases} \text{constant sensitivity over 100 Hz - 20 kHz} \\ \text{meet } MDA^{\text{Target}} \text{ over 100 Hz - 20 kHz} \end{cases}$$

where $\mathbf{L_M}$ and $\mathbf{t_M}$ are vectors corresponding to the varied proof mass thickness dimensions.

3.4.2 Results

Figure 3.4 shows the relationship between the normalized A_S^{AXL} and t_{piezo} using constant and varied $\tan\delta$ and $\tilde{d}_{31}$ properties. We note that A_S^{AXL} decreases with t_{piezo} using both constant and varied material properties, but this decrease occurs at different slopes. For instance, assuming variable material properties, A_S^{AXL} is reduced by 96% by increasing t_{piezo} to 1 µm from 0.25 µm; whereas for constant material properties, we obtain an 86% reduction. However, unlike the previous two sensor designs, the qualitative behavior highly depends on the target operational bandwidth. This is evident by Eq. 2.27 that provides an implicit relation between f_β, L, and L_M, where changing the upper frequency bound does not simply scale the calculation for L by some constant. Figure 3.5 shows the relationship between A_S^{AXL} and t_{piezo} when we adjust the target operational bandwidth to 100 Hz – 1 kHz. We observe that although A_S^{AXL} decreases with t_{piezo}, there exists a particular t_{piezo} value that minimizes A_S^{AXL} and any higher thicknesses will lead to an increase in the sensor area. This

particular t_{piezo} value depends on the material properties used. Specifically, in Fig. 3.5 and for varied material properties, A_S^{AXL} is reduced by 93% by increasing t_{piezo} to 1.75 µm from 0.25 µm; while further increasing t_{piezo} to 2 µm leads to a 1% increase. Similarly, for constant material properties, we obtain a 58% reduction by increasing t_{piezo} to 0.75 µm from 0.25 µm; while further increasing to 2 µm leads to a 26% increase.

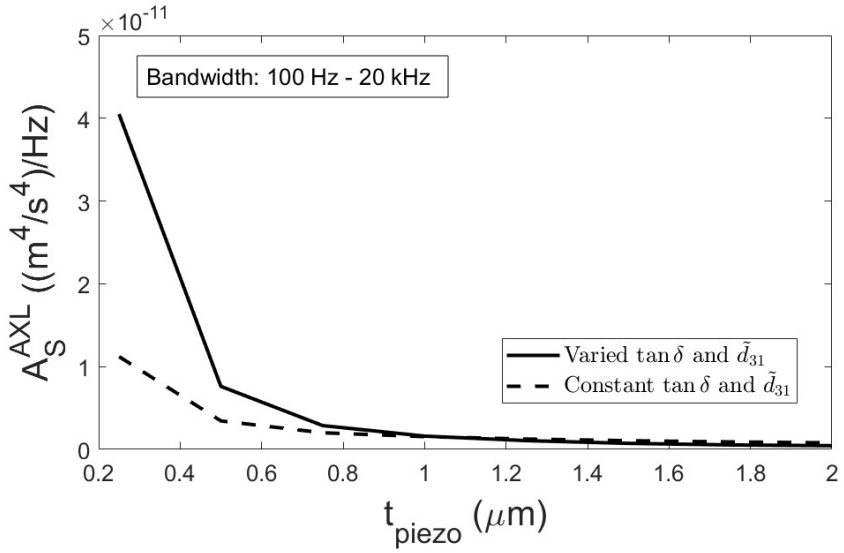

Figure 3.4: Relationship between the normalized A_S^{AXL} and t_{piezo} for a bandwidth of 100 Hz – 20 kHz, using varied and constant $\tan\delta$ and $\tilde{d}_{31}$.

3.5 Discussion and conclusions

To summarize, we developed an approach to investigate the effect of the piezoelectric thickness, $\tan\delta$, and $\tilde{d}_{31}$ on the sensor area of three canonical sensor designs: a sensor under uniform pressure, a sensor with a prescribed displacement at the free end, and an accelerometer with a proof mass at the free end. Gaining insight into these effects can guide the early stages of sensor design and allow for the creation of small and compact sensors that still achieve a desired performance. In addition, using this investigation, one can converge upon what piezoelectric thickness to use early in the sensor design process, which will help in preventing significant delays in manufacturing.

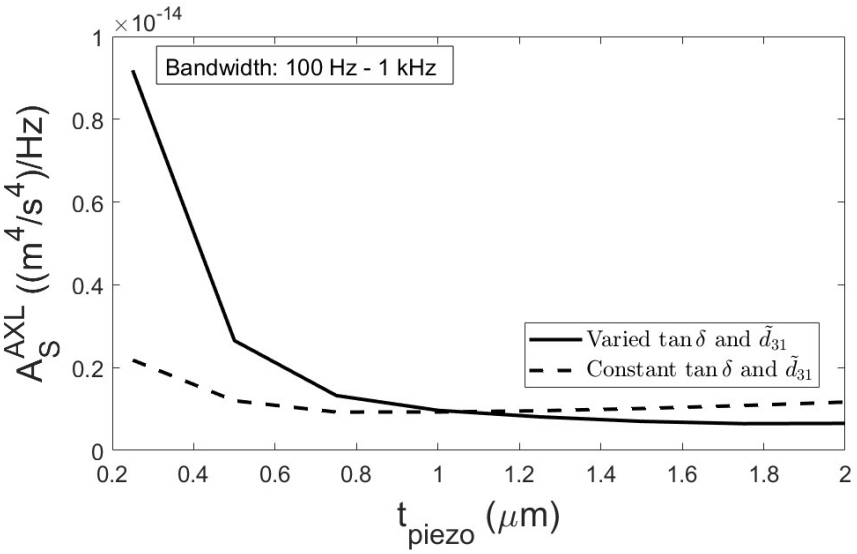

Figure 3.5: Relationship between normalized A_S^{AXL} and t_{piezo} for a bandwidth of 100 Hz – 1 kHz, using varied and constant $\tan\delta$ and $\tilde{d}_{31}$.

We investigated iso-bandwidth designs with constant sensitivity over the operational bandwidth (100 Hz – 20 kHz) and a set target noise floor. We defined the optimization problem for each design, where the sensor area was to be minimized. First, assuming $\tan\delta$, and $\tilde{d}_{31}$ vary as explained in Martin et al. (2004), we identified that for a sensor under uniform pressure, the sensor area remains approximately constant regardless of the piezoelectric thickness. Whereas if we use constant material properties, we find that thinner thicknesses lead to smaller sensor areas. The latter is in agreement with the findings of Littrell (2010), who reported that thinner AlN films resulted in better sensor performance. However, in Littrell (2010), the primary optimization centered around the output energy of the sensor normalized to the sensor area, and the author did not provide the explicit relationship between the sensor area and the piezoelectric thickness, as is shown in this chapter. Furthermore, it is important to note that as the thickness decreases, the difficulty of depositing high-quality films increases and the quality of the film properties decreases, as shown in Martin et al. (2004). Therefore, a more comprehensive study of the piezoelectric-thickness-dependence of $\tan\delta$ and $\tilde{d}_{31}$ is needed, as these parameters are affected by the fabrication tools, the substrate used, and many other factors. We also should be cautious about simply

claiming that thinner thicknesses are better. Setting aside the material properties of thin films, as the thickness decreases, the previously negligible electrode thickness becomes significant and must be accounted for in the calculation of the bending stiffness. This, in turn, will impact all other calculations discussed in this chapter.

Second, for a sensor with a prescribed displacement at the free end and an accelerometer with a proof mass, the sensor areas decrease with an increasing piezoelectric thickness. To our knowledge, these results have not been previously presented in the literature. However, these results highly depend on $\tan\delta$ and $\tilde{d}_{31}$, as can be observed by comparing the results of our investigation when we use constant values for these properties instead. This reaffirms our previous statement that a better understanding of the effect of the piezoelectric thickness on these material properties will help to better model the performance of sensors. In addition, while thicker thicknesses lead to smaller sensor areas, we must consider the trade-off during manufacturing. Thicker films involve longer deposition times and higher costs. For both sensors, it may be more advantageous to increase the thickness slightly, for example from 0.25 µm to 1 µm, rather than opting for the thickest option in order to avoid the cost and longer deposition times. Also, opting for even thicker thicknesses than what is presented in this chapter (>2 µm) could make the sensors stiffer, which would affect the sensor performance.

Third, only the results for the accelerometer design were affected by changing the target operational bandwidth. This is because of the additional feature that this sensor design has: the proof mass. The proof mass dimensions (thickness, t_M, and length, L_M) are used to determine the piezoelectric length, L, and width, b, through the implicit relation for the sensitivity constraint (upper frequency bound) and the explicit relation for the noise floor (low frequency bound). In addition, the sensor area for this design depends not only on L and b, but also on L_M. Due to these relations, the operational bandwidth of the accelerometer design will affect the final results.

Lastly, other sensor configurations beyond the three presented in this work can be explored

using the same investigation steps outlined in the previous sections. It should be noted that the sensor area, as defined in this chapter, does not account for a frame or spacing between a cantilever and a frame. In the case of multi-bandwidth sensors where multiple cantilevers are used within one design, the spacing between cantilevers and the frame will add more area to the overall design, and this is dependent on the limitations of deep reactive ion etching (DRIE) used in fabrication. The relationship between this new area and the piezoelectric thickness should be investigated.

CHAPTER 4

Modeling of the Middle Ear: Can a Middle Ear Speaker Amplify Sounds at the Stapes?

As Section 1.2.3 outlines, all commercial middle ear implants utilize direct mechanical attachments to middle ear features (incus, stapes, etc.) to deliver amplified sound stimuli. However, to our knowledge, there has been limited research exploring the potential use of a middle ear acoustic receiver (speaker) to amplify sounds at the stapes. An implanted middle ear speaker is an attractive alternative option, as the implantation surgery may be less invasive than that of current commercial middle ear implants. However, to our knowledge, there has been limited research exploring its potential use in implantable prostheses. In this chapter, we aim to investigate and analyze the feasibility of using an implanted acoustic speaker to amplify the motion of the stapes without direct mechanical attachment to any of the middle ear structures. The findings of this study can serve as the basis for future temporal bone measurements and testing, potentially leading to in vivo measurements.

4.1 Modeling and stability analysis

In this section, we introduce the lumped parameter model used to simulate the response of the human ear. We will introduce the design parameters and explain how we set up the investigation to account for the effect of an implanted middle ear speaker. We will also discuss the stability of the system and the conditions under which it becomes unstable.

4.1.1 Lumped parameter model

The lumped parameter model used in this work was presented in Han et al. (2023) and is shown in Fig. 4.1. In this model, we use six masses connected to springs and dampers to simulate the response of the human ear. We include the ear canal, the tympanic membrane, the middle ear ossicles (malleus, incus, and stapes), and the cochlea (Fig. 1.1). Specifically, mass m_1 represents the mass of the air in the ear canal coupled to the tympanic membrane (m_2) through spring k_2 and damper c_2, and k_1 and c_1 represent the tympanic annulus ligament. The masses m_3, m_4, and m_5 represent the mass of the malleus, incus, and stapes, where k_3 and c_3 are the tympanic membrane-malleus connection, k_5 and c_5 are the malleus-incus joint, and k_6 and c_6 are the incus-stapes joint. The damper c_4 represents the superior mallear ligament, c_7 represents the superior incudal ligament, and the spring k_7 represents the posterior incudal ligament. Spring k_8 and damper c_8 represent the stapedial annular ligament, and spring k_8^* represents the stapedial tendon. Finally, mass m_6 represents the mass of the cochlear fluid supported by dampers c_9 and c_{10}.

The governing equation of this lumped parameter model is (Feng and Gan, 2004):

$$[\overline{M}]\ddot{\boldsymbol{x}} + [\overline{C}]\dot{\boldsymbol{x}} + [\overline{K}]\boldsymbol{x} = \mathbf{F}, \tag{4.1}$$

where $[\overline{M}]$ is the 6×6 mass matrix, $[\overline{C}]$ is the 6×6 damping matrix, $[\overline{K}]$ is the 6×6 spring matrix, $\mathbf{F}$ is the 6×1 force vector, and $\boldsymbol{x}$ is the 6×1 displacement vector of the six masses. Furthermore, $\ddot{\boldsymbol{x}}$ and $\dot{\boldsymbol{x}}$ are the acceleration and velocity vectors. We assume an $e^{j\omega t}$ time dependence, where ω is the frequency of vibration. Thus, Eq. 4.1 can be re-written as:

$$\Big(-\omega^2[\overline{M}] + j\omega[\overline{C}] + [\overline{K}] \Big) \boldsymbol{A_x} = \boldsymbol{A_F}, \tag{4.2}$$

where $\boldsymbol{A_x}$ and $\boldsymbol{A_F}$ are vectors corresponding to the complex displacement and force amplitudes. We can solve for $\boldsymbol{A_x}$ in Eq. 4.2 to obtain the displacement of any middle ear feature

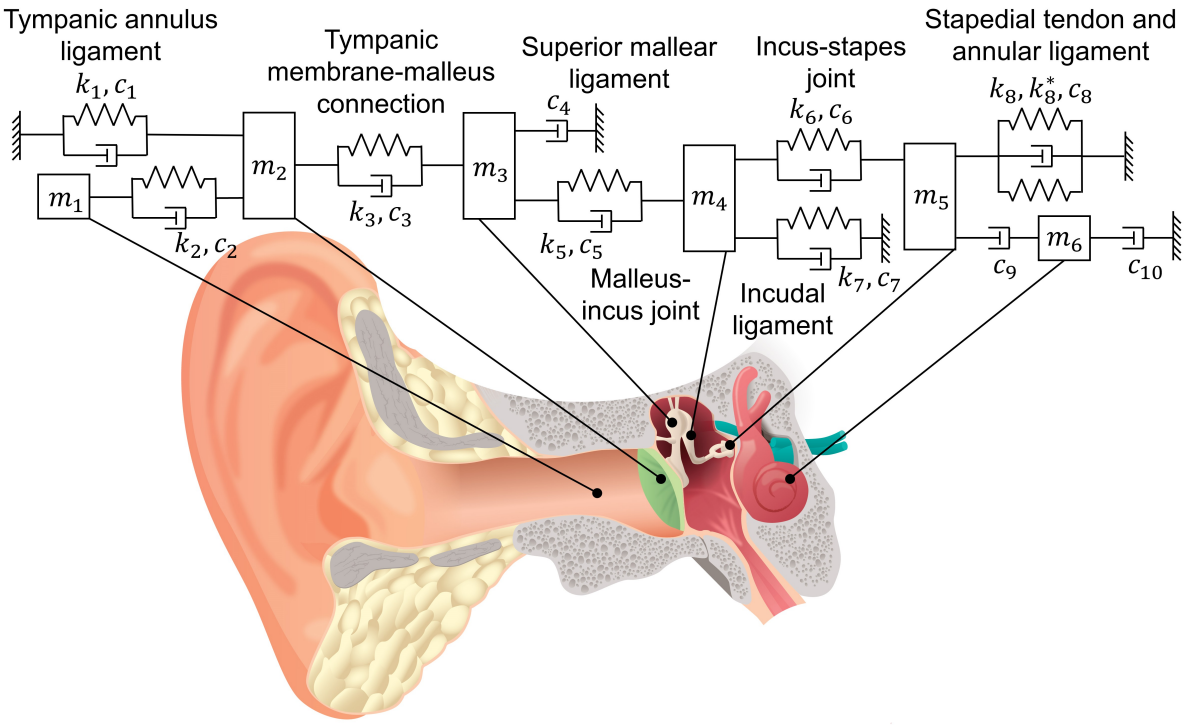

Figure 4.1: Lumped parameter model presented in Han et al. (2023) used to simulate the response of the human ear. Figure credit to Brian Townsend.

within this human ear model. Equations 4.3–4.7 show the detailed expressions for the matrices and vectors in Eqs. 4.1 and 4.2, and Table 4.1 displays all parameter values from Han et al. (2023). Note that the subscripts 1-6 in Eqs. 4.6 and 4.7 represent the displacements of and the forces on the six corresponding masses.

$$[\overline{M}] = \begin{bmatrix} m_1 & 0 & 0 & 0 & 0 & 0 \\ 0 & m_2 & 0 & 0 & 0 & 0 \\ 0 & 0 & m_3 & 0 & 0 & 0 \\ 0 & 0 & 0 & m_4 & 0 & 0 \\ 0 & 0 & 0 & 0 & m_5 & 0 \\ 0 & 0 & 0 & 0 & 0 & m_6 \end{bmatrix} \tag{4.3}$$

$$[\overline{C}] = \begin{bmatrix} c_2 & -c_2 & 0 & 0 & 0 & 0 \\ -c_2 & c_1 + c_2 + c_3 & -c_3 & 0 & 0 & 0 \\ 0 & -c_3 & c_3 + c_4 + c_5 & -c_5 & 0 & 0 \\ 0 & 0 & -c_5 & c_5 + c_6 + c_7 & -c_6 & 0 \\ 0 & 0 & 0 & -c_6 & c_6 + c_8 + c_9 & -c_9 \\ 0 & 0 & 0 & 0 & -c_9 & c_9 + c_{10} \end{bmatrix} \tag{4.4}$$

$$[K] = \begin{bmatrix} k_2 & -k_2 & 0 & 0 & 0 & 0 \\ -k_2 & k_1+k_2+k_3 & -k_3 & 0 & 0 & 0 \\ 0 & -k_3 & k_3+k_5 & -k_5 & 0 & 0 \\ 0 & 0 & -k_5 & k_5+k_6+k_7 & -k_6 & 0 \\ 0 & 0 & 0 & -k_6 & k_6+k_8+k_8^* & 0 \\ 0 & 0 & 0 & 0 & 0 & 0 \end{bmatrix} \tag{4.5}$$

$$\boldsymbol{x} = \underbrace{\begin{bmatrix} x_1 & x_2 & x_3 & x_4 & x_5 & x_6 \end{bmatrix}^T}_{\boldsymbol{A_x}} e^{j\omega t} \tag{4.6}$$

$$\mathbf{F} = \underbrace{\begin{bmatrix} F_1 & F_2 & F_3 & F_4 & F_5 & F_6 \end{bmatrix}^T}_{\boldsymbol{A_F}} e^{j\omega t} \tag{4.7}$$

Table 4.1: Lumped parameter model values used in Han et al. (2023)

	$i=1$	$i=2$	$i=3$	$i=4$	$i=5$	$i=6$	$i=7$	$i=8$	$i=9$	$i=10$
m_i (mg)	1.55	2.70	23.0	25.0	1.78	25.5	–	–	–	–
c_i (mNs/m)	0.07	500	1740	122	359	0.28	20.0	0.04	100	100
k_i (kN/m)	1.20	0.20	0.947	–	1000	1.20	0.20	0.625	–	–
k_8^* (kN/m)	0.05									

4.1.2 Middle ear speaker: forcing, feedback, and stability

To investigate the effect of an implanted acoustic middle ear receiver on the motion of the stapes (x_5 in $\boldsymbol{A_x}$), we consider the excitation of the form of an external pressure, P_E, on the tympanic membrane and an internal pressure within the middle ear cavity acting on the tympanic membrane and the stapes, P_I. The external pressure represents the external acoustic stimulus incident on the tympanic membrane that needs to be amplified. The internal pressure represents the sound stimulus provided by the implanted middle ear receiver. Throughout the middle ear cavity, we assume that the pressure, P_I, is approximately uniform. Thus, the force vector in Eq. 4.7 becomes:

$$\mathbf{F} = \underbrace{\begin{bmatrix} 0 & A_{TM}(P_E - P_I) & 0 & 0 & A_{ST}P_I & 0 \end{bmatrix}^T}_{\boldsymbol{A_F}} e^{j\omega t}, \tag{4.8}$$

where A_{TM} is the surface area of the tympanic membrane (approx. 80 mm^2), and A_{ST} is the surface area of the footplate of the stapes (approx. 3.2 mm^2) (Udagatti and Dinesh Kumar, 2016; Békésy, 1960; Wever and Lawrence, 1954).

If we assume no feedback and no processing delays in the system, the internal pressure, P_I, is defined as the pressure measured at the eardrum from the ear canal side, P_M, adjusted by γ^*, such that $P_I = \gamma^* P_M$, $P_M = P_E$, and γ^* is the gain of the implanted receiver. This no-feedback system is unconditionally stable. To evaluate the feasibility of using an implantable middle ear speaker, we also need to understand the stability of the system as we increase or decrease the gain, γ^*. The system, as defined previously, is unconditionally stable because γ^* does not impact P_M. For the stability analysis, we take into account the feedback caused by the speaker output being detected by the sensing unit, such as a microphone, used in the implantable hearing aid. We redefine the measured pressure, P_M, as the sum of the external pressure and the radiated pressure, $P_M = P_E + P_R$, where P_R represents the radiated feedback pressure leaking from the middle ear (speaker output) into the ear canal, and thereby influencing P_M.

To determine whether the system is stable, we calculate its eigenvalues, λ. However, first we must define P_R. We assume that P_R is equal to the acoustic pressure due to the radiation loading on the tympanic membrane. Hence, P_R is given by: $A_{TM}P_R = -k_2(x_2 - x_1) - c_2(\dot{x}_2 - \dot{x}_1) = -m_1\ddot{x}_1$ (see Fig. 4.1). However, we also allow for some delay, τ, to be introduced to the system by the gain (e.g., due to processing delays). Accounting for the feedback and time delay, we have that $P_I = \overline{\gamma}^* P_M$, where $\overline{\gamma}^*$ is the gain with the time delay. Hence, $P_I = \gamma^*\left(P_E(t-\tau) - \frac{m_1\ddot{x}_1(t-\tau)}{A_{TM}}\right)$ We can use this definition to recast Eq. 4.1 to include the feedback and time delay:

$$[\overline{M}]\ddot{\boldsymbol{x}} + [\overline{C}]\dot{\boldsymbol{x}} + [\overline{K}]\boldsymbol{x} - \overline{U}\ddot{\boldsymbol{x}}(\boldsymbol{t} - \boldsymbol{\tau}) = \mathbf{F}^* \tag{4.9}$$

where $[U]$ is the 6×6 matrix that accounts for P_R:

$$\begin{bmatrix} 0 & 0 & 0 & 0 & 0 & 0 \\ \gamma^* m_1 & 0 & 0 & 0 & 0 & 0 \\ 0 & 0 & 0 & 0 & 0 & 0 \\ 0 & 0 & 0 & 0 & 0 & 0 \\ -\gamma^* m_1 \frac{A_{ST}}{A_{TM}} & 0 & 0 & 0 & 0 & 0 \\ 0 & 0 & 0 & 0 & 0 & 0 \end{bmatrix} \tag{4.10}$$

and $\mathbf{F}^*$ is updated as follows:

$$\mathbf{F}^* = \underbrace{\begin{bmatrix} 0 & A_{TM}(P_E - \gamma^* P_E(t-\tau)) & 0 & 0 & A_{ST}\gamma^* P_E(t-\tau) & 0 \end{bmatrix}^T}_{\boldsymbol{A_F}} e^{j\omega t} \tag{4.11}$$

Next, we take the Laplace transform of Eq. 4.9:

$$\lambda^2[\overline{M} - Ue^{-\lambda\tau}] + \lambda[\overline{C}] + [\overline{K}] = 0 \tag{4.12}$$

Due to the $e^{-\lambda\tau}$ term, we cannot solve the eigenvalue problem through standard methods. Instead, we derive an approximation of this term utilizing the Padé approximation (Baker and Graves-Morris, 1996). We choose a third-order approximation to reduce the error (Khodier, 2000), provided below, and for more information on the derivation of this formula, see Khodier (2000); Baker and Graves-Morris (1996) and Appendix C.

$$e^{-\lambda\tau} \approx \frac{1 - \frac{1}{2}\lambda\tau + \frac{1}{10}(\lambda\tau)^2 - \frac{1}{120}(\lambda\tau)^3}{1 + \frac{1}{2}\lambda\tau + \frac{1}{10}(\lambda\tau)^2 + \frac{1}{120}(\lambda\tau)^3} \tag{4.13}$$

We then take the determinant of Eq. 4.12 and equate it to zero to calculate the eigenvalues of the system.

4.2 Results

Before analyzing the effect of a middle ear speaker on the motion of the stapes, we test the validity of the lumped parameter model by comparing it to three experiments presented in the literature (Gan et al., 2009; O'Connor and Puria, 2006; Aibara et al., 2001). For all experiments, measurements were conducted in human cadaveric temporal bones. An acoustic pressure was introduced at the eardrum ($P_E \neq 0, P_I = 0$), and a laser Doppler vibrometer was used to measure the response at the stapes. Figure 4.2 shows the normalized displacement and phase of the stapes from these experimental data and the predicted response from the model. We observe a good match between the experimental data and the model.

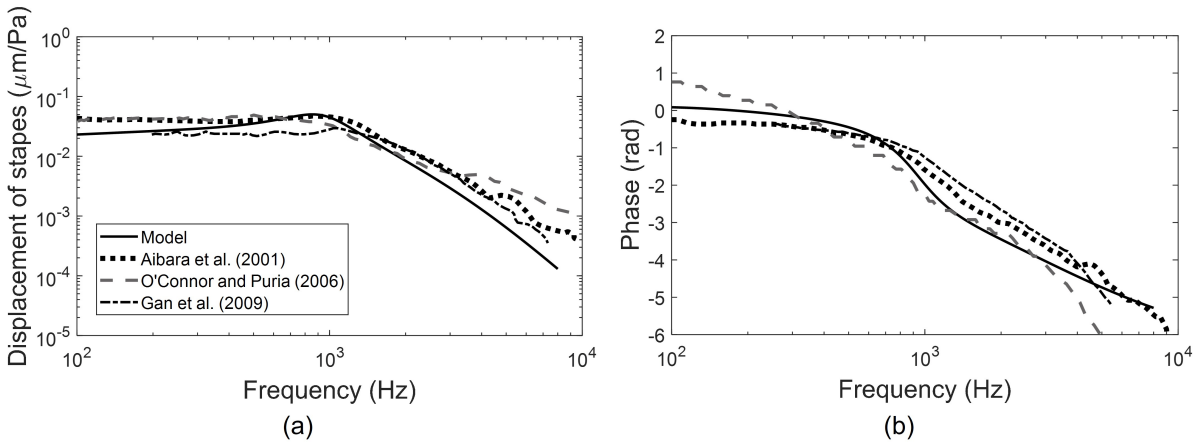

Figure 4.2: Model and experimental data (Gan et al., 2009; O'Connor and Puria, 2006; Aibara et al., 2001): (a) Normalized displacement of the stapes due to an external pressure incident on the tympanic membrane. (b) Phase of the stapes.

Secondly, we investigate the response of the model when an internal pressure is introduced to the middle ear cavity. O'Connor and Puria (2006) presented an experimental study in which they injected sound directly into the middle ear, leaving the ear canal unplugged and without an external pressure incident on the tympanic membrane. Figure 4.3 compares this experimental data with the results from the model, where $P_E = 0$ and the gain of the internal pressure is $\gamma^* = 1$. We assume that there is no time delay in the internal pressure. Once again, we observe a good match in both plots. We note here that the phase of the stapes

due to internal excitation (shown in Fig. 4.3(b)) is approximately π radians lower than the phase in Fig. 4.2(b). This implies that the external pressure and internal pressure with a positive gain move the stapes in opposite directions. In addition, these results reaffirm our assumption that the pressure within the middle ear cavity is approximately uniform.

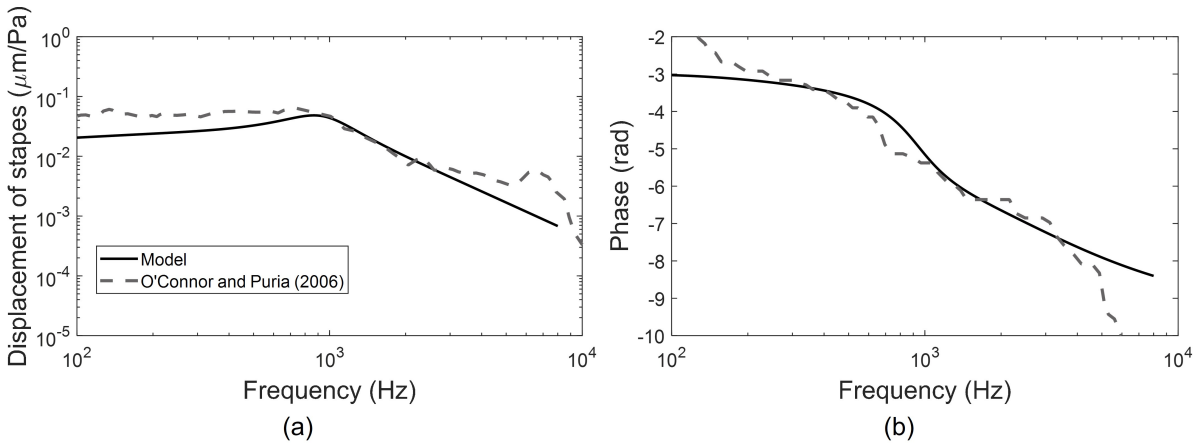

Figure 4.3: Model and experimental data (O'Connor and Puria, 2006): (a) Normalized displacement of the stapes due to an internal pressure in the middle ear cavity. (b) Phase of the stapes. We assume no time delay.

4.2.1 Combined external and internal acoustic stimulation with no feedback and no time delay

Next, we investigate the simultaneous effect of an external and internal pressure on the system. As outlined in Section 4.1.2, we excite the lumped parameter model with an external pressure, P_E, on the tympanic membrane and with an internal pressure, P_I, within the middle ear cavity acting on the tympanic membrane and the stapes (Eq. 4.8). For these initial results, we assume that there is no leakage of the radiated pressure to the microphone and no time delay due to the gain. We then normalize all results to the external pressure, and vary the gain, γ^*, from positive to negative values.

Figure 4.4 shows the modeled normalized displacement of the stapes. We observe that a positive gain ($\gamma^* = 1$) attenuates the displacement. This result is expected, as we noted in

the previous section that an internal pressure with a positive gain and an external pressure move the stapes in opposite directions, thereby attenuating its displacement. Conversely, a negative gain ($\gamma^* = -1$ or -2) amplifies the displacement. This occurs because a negative gain causes a phase shift of π in the internal pressure, which leads to being in-phase with the external pressure. Thus, both pressures move the stapes in the same direction when $\gamma^* < 0$ (c.f. Figs. 4.2(b) and 4.3(b)).

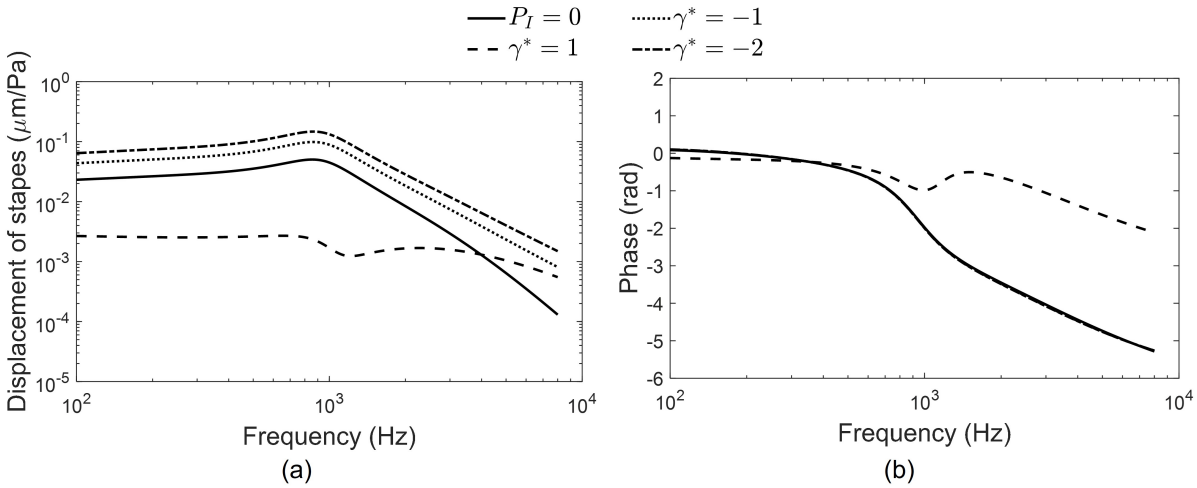

Figure 4.4: Model results: (a) Normalized displacement of the stapes due to an external, internal pressure, and variable γ^* (b) Phase of the stapes. We assume no feedback and no time delay.

To visualize the amplification of the motion at the stapes, we plot the displacement ratio due to the internal and external pressures. Specifically, Fig. 4.5 shows the ratio of the displacement caused by the external and internal pressure with a $\gamma^* = -1$ to that caused solely by the external pressure. We observe that at low frequencies (< 1 kHz), the combination of the external and internal pressures can approximately double the displacement, as also seen in Fig 4.4(a). At higher frequencies, the amplification can increase to as much as six times. Furthermore, even greater amplification can be achieved with higher negative gains.

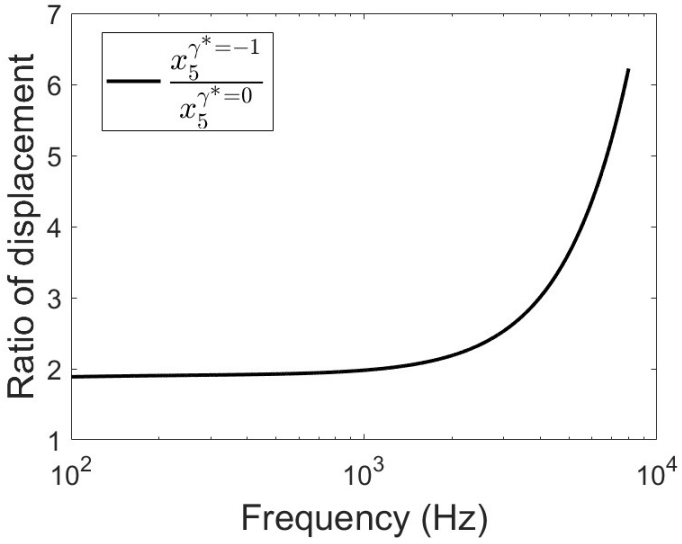

Figure 4.5: Displacement ratio of the stapes. The numerator is the displacement due to an external and internal pressure with $\gamma^* = -1$. The denominator is the displacement only due to an external pressure. We assume no feedback and no time delay.

4.2.2 Stability and gain when the system includes feedback and time delay

To conduct the stability analysis outlined in Section 4.1.2, we calculate the eigenvalues, λ, and identify when the system becomes unstable. Figure 4.6 shows different λ values as we vary γ^*. For these results, we assume that the microphone is contaminated by the radiated pressure and the gain introduces a time delay, τ. Note that we do not include any controller compensation for this feedback. We introduce P_I with a delay of 10 ms ($\tau = 10$ ms) (Lelic et al., 2022). We observe that as we decrease the gain, there exists a point after $\gamma^* \lesssim -4.6$ at which the system becomes unstable (i.e., it has positive real eigenvalues).

In addition, we compare the results of the model that include the delay, τ, and the feedback, P_R, (Eq. 4.9) to the previous results presented in Figure 4.4, where we assumed no feedback and no time delay. Figure 4.7 shows the predicted displacement of the stapes normalized to the external pressure, accounting for $\tau = 10$ ms and P_R. We observe the comb-filter effect, which is a result of the distorted incoming pressure signals having a gain

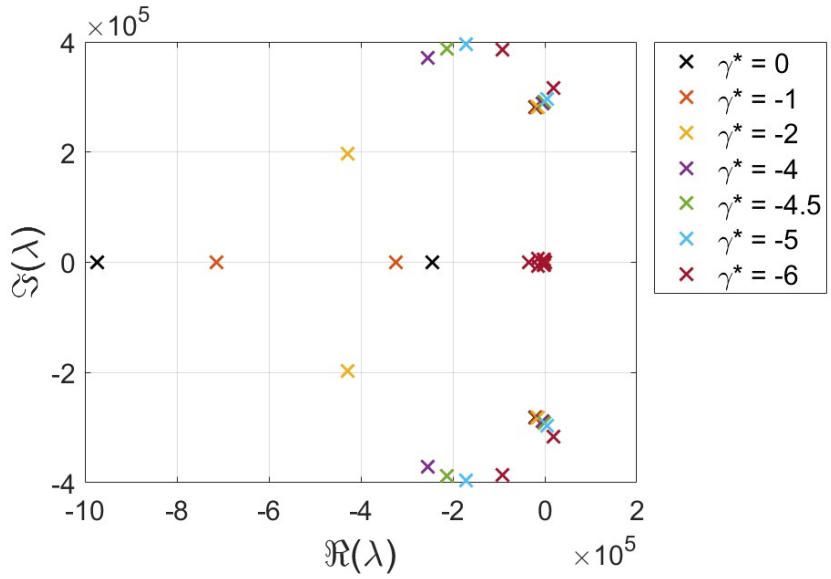

Figure 4.6: Eigenvalue solutions for various gains, with a time delay, $\tau = 10$ ms. The system is unstable for $\gamma^* \lesssim -4.6$.

with a time delay. This is a common side effect seen in hearing aids with open fittings or large vents (Stiefenhofer, 2023), which is similar to our investigation setup with the ear canal unplugged. The observed oscillations have notches spaced approximately $1/\tau$ Hz apart (Bramsløw, 2010). We can calculate these notch and peak intervals by identifying when the forcing term acting on the tympanic membrane (F_2) becomes small or large, which leads to the formation of a notch or a peak. We expect to see peaks when $\omega\tau = n\pi$ and $n = 2, 4, 6$, etc., as $e^{jn\pi} = \cos(n\pi) + j\sin(n\pi)$, $\cos(n\pi) = 1$, and $\sin(n\pi) = 0$. We expect to see notches when $\omega\tau = n\pi$ and $n = 1, 3, 5$, etc., as $\cos(n\pi) = -1$, and $\sin(n\pi) = 0$ (see Eq. 4.11). In the same figure, we also observe that as the gain increases, the oscillations become more compact, indicating that the internal pressure with the time delay starts to dominate the forcing on the tympanic membrane.

Furthermore, we investigate the effect of the time delay on the displacement of the stapes. Figure 4.8 shows that decreasing the time delay can significantly reduce the comb-filter effect. At very low delays, $\tau = 0.1$ ms (Stiefenhofer, 2023), we observe no significant oscillations. However, we note that for $\gamma^* = -1$, we observe a decrease in the displacement at higher

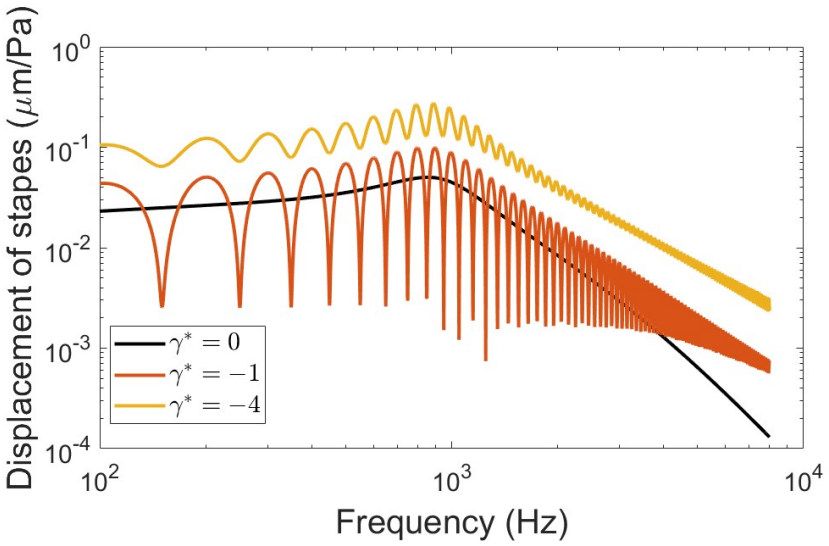

Figure 4.7: Predicted displacement of the stapes normalized to the external pressure accounting for feedback and a time delay of $\tau = 10$ ms.

frequencies (approx. 5 kHz). This decrease is not as prominent in $\gamma^* = -4$. This is related to a notch being formed at $\omega = 2\pi(5 \text{ kHz})$, with a $\tau = 0.1$ ms, such that when the frequency is 5 kHz, $\omega\tau = \pi$, $\cos(n\pi) = -1$, and $\sin(n\pi) = 0$. As $\gamma^* = -1$, this leads to the F_2 term in Eq. 4.11 to approach zero. Thus, the forcing at 5 kHz is dominated only by the force acting on the stapes (F_5), which ultimately leads to a decrease in the displacement. This effect becomes less pronounced at higher negative gains because the F_2 term in Eq. 4.11 turns negative, resulting in a decrease in displacement, although not to the same extent as when the term is zero.

Finally, we compare the displacement ratio due to the internal and external pressures using $\tau = 0.1$ ms with the ratio presented in Fig. 4.5. We observe that with a delay of $\tau = 0.1$ ms, we still achieve double the displacement at low frequencies (< 1 kHz). However, above 1 kHz, we observe a slow decline in the amplification due to the notch formation discussed previously for $\gamma^* = -1$. Above 5 kHz, we again observe an increase in amplification, reaching a fivefold amplification at 8 kHz. Once again, greater amplification can be achieved with higher negative gains, within stability bounds.

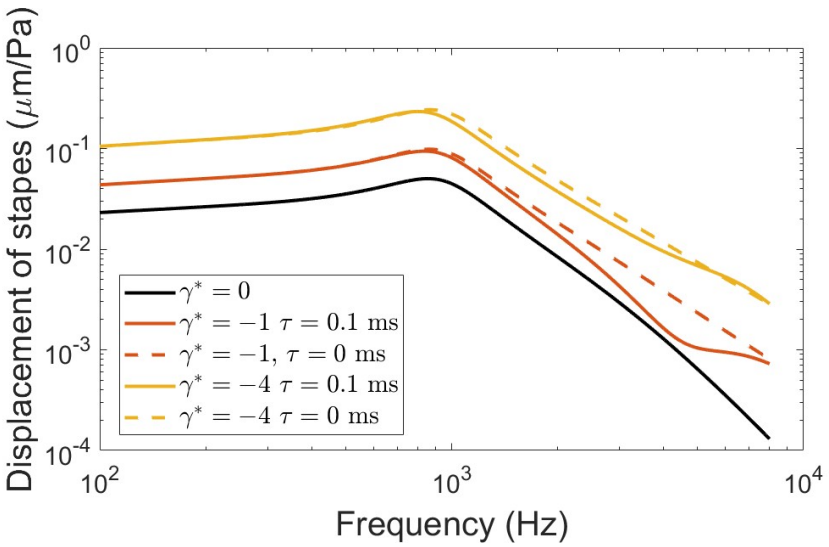

Figure 4.8: Comparing predicted displacements of the stapes normalized to the external pressure. The displacements with delays incorporate feedback, while those without delays assume no feedback.

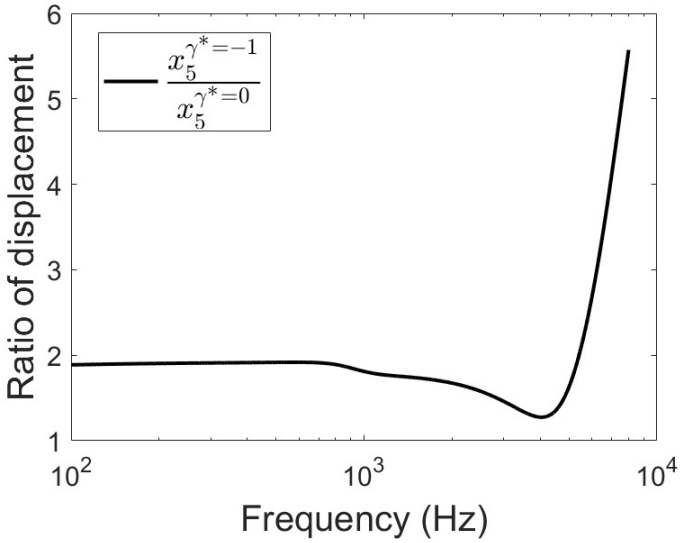

Figure 4.9: Displacement ratio of the stapes. The numerator is the displacement due to an external and internal pressure with $\gamma^* = -1$. The denominator is the displacement only due to an external pressure. We assume there is feedback and a time delay of $\tau = 0.1$ ms.

4.3 Discussion and conclusions

In this chapter, we investigated the feasibility of using an implanted middle ear speaker to amplify the motion of the stapes without any direct mechanical attachments. Using a lumped parameter model to simulate the response of the human ear (Han et al., 2023), we identified that a middle ear speaker can amplify the motion of the stapes as long as the pressure it injects into the middle ear has a negative gain and the ear canal is open to external stimuli. At high frequencies (> 1 kHz), with a gain of $\gamma^* = -1$, and with no feedback or time delay, the amplification can be up to six times compared to the motion of the stapes with no middle ear speaker. Also, even greater amplification can be achieved with more negative γ^*.

The simple stability analysis presented in this chapter shows that if no measures are taken to cancel the feedback pressure signals that leak into the ear canal, then the system can become unstable as γ^* decreases ($\gamma^* \lesssim -4.6$). The time delay, $\tau = 10$ ms, introduced by the gain (e.g., due to processing delays) causes oscillations in the displacement of the stapes (comb-filter effect). Lower time delays, $\tau = 0.1$ ms, can significantly reduce the comb-filter effect, allowing for double to fivefold amplification at high frequencies and with a gain of $\gamma^* = -1$. In addition, if the implanted speaker were used alongside an implantable middle ear sensor, such as the accelerometers presented in Chapter 2, some feedback cancellation would be needed to enhance the gain within stability bounds (Zheng et al., 2023). This feedback cancellation would prevent the sensor from picking up the internal signals emitted from the speaker and only allow for the external stimuli to be sensed. This is an important next step in the design process.

We also acknowledge that the results presented in this work are based on only one lumped parameter model. Further studies could be conducted using other lumped element models, such as those presented in Wils et al. (2023), to investigate the variation in the predicted amplification factor of the stapes' motion. In addition, a finite element model of the human middle ear, such as in Burovikhin et al. (2024), can provide great insight into a similar

investigation. Temporal bone measurements using external and internal pressure excitations would also help verify and validate the findings of this study. Furthermore, as this is an initial analysis of using a middle ear speaker, we do not explore how the speaker will be implanted to inject the internal pressure into the middle ear cavity. One example may be to mount it to the patient's mastoid process by drilling a hole in the skull (Miller, 2004).

In this investigation, we do not include the effect of the Eustachian tube. As we explained in Chapter 1, the Eustachian tube, which connects to the pharynx, briefly opens to keep the air pressure within the middle ear cavity close to ambient pressure (Kanegaonkar and Whittaker, 2015; Møller, 2006). We anticipate that although the implanted speaker may continuously inject the gained internal pressure inside the middle ear, the opening of the Eustachian tube will lead to some leakage. This leakage will result in a lower internal pressure within the cavity and thus, some decrease in the expected amplification at the stapes. The effect of the Eustachian tube in this system should be further investigated.

Overall, the results presented in this chapter provide a new analysis of how an implanted middle ear speaker can drive the motion of the stapes. This study motivates further exploration of this research area, including potential in vivo experiments. By developing new methods of delivering stimuli to the middle ear that could rival the commercial mechanical attachments of current active middle ear implants, we move one step closer to designing a new generation of completely implantable hearing aids.

CHAPTER 5

Conclusions, Contributions, and Future Work

5.1 Conclusions

The main goal of the work presented in this thesis was the design and improvement of sensors and actuators for completely implantable auditory prostheses. In Chapter 1, we introduced the general knowledge and motivation behind implantable prostheses. Mainly, we discussed the significant impact hearing loss has on understanding speech and communicating (Cunningham and Tucci, 2017). With over 5% of the world's population being affected by hearing loss (WHO, 2024), finding a way to address this growing disabling condition has become an imperative task for many researchers and scientists. Hearing aids and cochlear implants are designed to aid people with mild to profound hearing loss (NIDCD, 2024a; NIDCD, 2022), but their limitations, primarily the external components (e.g., microphones), impact their adoption rates. Completely implantable auditory prostheses address some of these barriers by entirely eliminating the external components. However, there is no commercial FDA-approved completely implantable cochlear implant, and of the three FDA-approved hearing aid middle ear implants, only one provides an implantable sensor that replaces the external microphone (Babajanian et al., 2024). In addition, all of the middle ear implants operate by utilizing mechanical attachments to a middle ear feature, such as a transducer on the stapes, to deliver amplified vibrations, with no other alternative approach explored (Banakis Hartl and Jenkins, 2020). In this thesis, we introduced the design

of implantable accelerometers intended to replace the external microphones in all auditory prostheses. We examined various design parameters and metrics, investigating how they can be adjusted to achieve a desired sensor performance. Furthermore, we carried out a new analysis of delivering amplified sound stimuli to the stapes through an implanted speaker, as opposed to a vibrating transducer. In this section, we summarize the conclusions drawn from each chapter.

In Chapter 2, we presented a discretized and exhaustive design optimization approach for multi-bandwidth MEMS accelerometers. Each multi-bandwidth sensor consisted of several sensing elements. The design approach used the operational frequency bandwidth, noise floor, and geometry of each sensing element to answer the question: what is the number of sensing elements that continue to meet the full operational bandwidth (100 Hz-8 kHz) with constant sensitivity and low-noise floor, but will also further minimize the total area of the sensor? Through this study, we identified the unconstrained four-bandwidth design as the smallest accelerometer in the literature that meets all metrics. In addition, we identified three- and four-bandwidth accelerometers with constrained proof mass thicknesses that balance area minimization with ease of manufacturability. The latter designs are still smaller than the previously published dual-bandwidth design (Hake et al., 2023).

In Chapter 3, we investigated the effect of the piezoelectric thickness, $\tan\delta$, and $\tilde{d}_{31}$ on the sensor area of three canonical MEMS cantilever sensors: a sensor under uniform pressure, a sensor with a prescribed displacement at the free end, and an accelerometer with a proof mass at the free end. All three sensor designs have been used in totally implantable prosthesis applications (Bruschini et al., 2009; Hake et al., 2023; Yeiser et al., 2024). Assuming varying $\tan\delta$, and $\tilde{d}_{31}$ (Martin et al., 2004), we identified that for a sensor under uniform pressure, the sensor area remains approximately constant regardless of the piezoelectric thickness. In contrast, for a sensor with a prescribed displacement at the free end and an accelerometer with a proof mass at the free end, the sensor areas decrease with an increasing piezoelectric thickness. However, these results highly depend on $\tan\delta$ and $\tilde{d}_{31}$, and, for the accelerometer

design, also depend on the desired operational bandwidth. Selecting a piezoelectric thickness early in the sensor design process is important, as this step will create significant delays in manufacturing.

In Chapter 4, we investigated the feasibility of using an implanted middle ear speaker to amplify the motion of the stapes without any direct mechanical attachment to middle ear features. Using a lumped parameter model (Han et al., 2023), we identified that a middle ear speaker can amplify the motion if the pressure it injects into the middle ear has a negative gain and the ear canal is unplugged. At high frequencies (> 1 kHz), with a $\gamma^* = -1$, and with no feedback or time delay, the model shows that the amplification can be up to six times compared to when no middle ear speaker is present. Even greater amplification can be achieved using more negative gains. However, it is essential to account for the instability of the system. We performed a simple stability analysis showing that for a time delay of $\tau = 10$ ms, as the gain becomes more negative ($\gamma^* \lesssim -4.6$), the system can become unstable. In addition, high time delays due to the gain introduce oscillations in the displacement of the stapes (comb-filter effect), but low time delays ($\tau = 0.1$ ms) can significantly reduce this effect, allowing for double to fivefold amplification at high frequencies and with a $\gamma^* = -1$.

5.2 Contributions

The contributions of this work are organized by chapter and are presented in two categories: core and additional. The core contributions center on the design of miniature piezoelectric sensors for general and totally implantable auditory protheses, and on the investigation of using a middle ear acoustic receiver to amplify sounds at the stapes. The specific contributions are listed below:

Chapter 2:

Core contributions:

- Developed a discretized and exhaustive design optimization approach to identify multi-bandwidth transducers with N sensing elements that meet the 20-phon noise floor with constant sensitivity over 100 Hz – 8 kHz while maintaining small form factors.

- Identified the unconstrained four-bandwidth design that, to our knowledge, is the smallest accelerometer in the literature that can meet the 20-phon noise floor over the 100 Hz – 8 kHz frequency bandwidth.

- Identified three- and four-bandwidth accelerometers with constrained proof mass thicknesses that balance area minimization with ease of manufacturability and have an 18% and a 23% MEMS die area reduction compared to the previously published dual-bandwidth sensor.

Additional contributions:

- Updated the full analytical model for a piezoelectric cantilever plate tip-loaded by a proof mass to incorporate rotational excitation (when $\theta_{by} \neq 0$).

- Updated the assumed-mode solution to the full analytical model, including identifying errors in the closed-form expressions of sensitivity ($S(f)$) and minimum detectable acceleration (MDA_z) used in all sensor design optimizations.

- Updated the resonant frequency approximation approach, including corrections in the 2×2 matrix and coefficients $\tilde{A}$, $\tilde{B}$, and $\tilde{C}$.

Chapter 3:

Core contributions:

- Developed an approach to investigate the effect of the piezoelectric thickness, $\tan\delta$, and $\tilde{d}_{31}$ on a MEMS canonical cantilever sensor with a prescribed displacement at the free end.

- Developed an approach to investigate the effect of the piezoelectric thickness, $\tan\delta$, and $\tilde{d}_{31}$ on a MEMS accelerometer with a proof mass at the free end.

Additional contributions:

- Updated the investigation of the piezoelectric thickness, $\tan\delta$, and $\tilde{d}_{31}$ on a MEMS sensor under uniform pressure to provide an explicit relation between the sensor area and piezoelectric thickness with constant and varied material properties.

Chapter 4:

Core contributions:

- Carried out a new analysis of how an implanted middle ear speaker can amplify the motion at the stapes. This investigation motivates further research in this field, with possibilities for developing more models, such as other lumped parameter or finite element models. It also motivates conducting temporal bone experiments, taking in vivo measurements, and, in general, designing a new generation of completely implantable hearing aids.

5.3 Future work

Based on the completed work presented in this thesis, we consider the following topics as potentially fruitful future endeavors:

- First, for the multi-bandwidth accelerometer investigation, a topology optimization can better inform the design process, leading to even smaller designs that achieve the same performance. In addition, further research into alternative attachment locations within the middle ear, such as the short process of the incus (Burovikhin et al., 2024), is warranted, as these locations may offer benefits like reduced surgical complexity and decreased risk. Also, once the accelerometer designs are fabricated, benchtop and cadaveric temporal bone experiments would help compare the results from the model and also highlight additional design constraints that may not be considered.

- Second, for the piezoelectric thickness study, a more comprehensive investigation of how $\tan\delta$ and $\tilde{d}_{31}$ depend on the thickness of different piezoelectric materials can help inform the results presented in Chapter 3. It can also help in understanding how these parameters are affected by the fabrication tools, the substrate used, and many other factors.

- Lastly, for the middle ear speaker analysis, a finite element model of the human middle ear may be used to compare with the results presented in this work. Similarly, cadaveric temporal bone measurements will also help verify and validate the findings of this study. In addition, further research is warranted on the feedback control of the system to compensate for time delays that may be experienced and maximize the amplification that can be achieved at any particular gain within stability bounds.

APPENDIX A

Appendix for Chapter 1

A.1 Matrix elements for full analytical model

The following expressions are used in Eq. 2.20 in Section 2.3.3.1:

$$X_1 = (-Y_1 - Y_2)\sin(\gamma L) - Y_3\cos(\gamma L) \qquad X_9 = (Y_4 + Y_5)\cosh(\gamma L) + Y_6\sinh(\gamma L)$$

$$X_2 = (-Y_1 - Y_2)\cos(\gamma L) + Y_3\sin(\gamma L) \qquad X_{10} = (Y_4 + Y_5)\sinh(\gamma L) + Y_6\cosh(\gamma L)$$

$$X_3 = (Y_1 - Y_2)\sinh(\gamma L) - Y_3\cosh(\gamma L) \qquad X_{11} = -(Y_6Y_7)\gamma\cos(\gamma L)$$

$$X_4 = (Y_1 - Y_2)\cosh(\gamma L) - Y_3\sinh(\gamma L) \qquad X_{12} = (Y_6Y_7)\gamma\sin(\gamma L)$$

$$X_5 = -(Y_6Y_7)\sin(\beta L) \qquad X_{13} = -(Y_6Y_7)\gamma\cosh(\gamma L)$$

$$X_6 = -(Y_6Y_7)\cos(\beta L) \qquad X_{14} = -(Y_6Y_7)\gamma\sinh(\gamma L)$$

$$X_7 = (-Y_4 + Y_5)\cos(\gamma L) + Y_6\sin(\gamma L) \qquad X_{15} = Y_8\beta\cos(\beta L) - Y_6\sin(\beta L)$$

$$X_8 = (Y_4 - Y_5)\sin(\gamma L) + Y_6\cos(\gamma L); \qquad X_{16} = -Y_8\beta\sin(\beta L) - Y_6\cos(\beta L)$$

In these expressions, Y_1–Y_8 are defined as follows:

$$Y_1 = \gamma^2 \overline{EI} \qquad Y_5 = Y_2 \gamma$$
$$Y_2 = \frac{1}{2} M L_M \omega^2 \qquad Y_6 = M\omega^2$$
$$Y_3 = I_M \gamma \omega^2 \qquad Y_7 = \frac{1}{2} t_M - t_{piezo}$$
$$Y_4 = Y_1 \gamma \qquad Y_8 = A/\tilde{s}_{11}^E$$

All variables included in these expressions are defined in Section 2.3.3.

A.2 Matrix elements for assumed-mode solution

The following expressions are used in Eq. 2.22 in Section 2.3.4.1:

$$\tilde{X}_1 = \frac{L_M M \omega^2 L^3}{2} + I_M \omega^2 3L^2 - 6L\overline{EI} \qquad \tilde{X}_5 = -M\omega^2 L^3 - \frac{L_M M \omega^2 3L^2}{2} - 6\overline{EI}$$
$$\tilde{X}_2 = \frac{L_M M \omega^2 L^2}{2} + I_M \omega^2 2L - 2\overline{EI} \qquad \tilde{X}_6 = -M\omega^2 L^2 - L_M M \omega^2 L$$
$$\tilde{X}_3 = \frac{L_M M \omega^2 L}{2} + I_M \omega^2 \qquad \tilde{X}_7 = -M\omega^2 L - \frac{L_M M \omega^2}{2}$$
$$\tilde{X}_4 = \frac{L_M M \omega^2}{2} \qquad \tilde{X}_8 = -M\omega^2$$

A.3 Coefficients for resonant frequency calculation

The following coefficients are used in Eq. 2.27 (updated from Hake (2021)):

$$\tilde{A} = (\rho_M b L_M t_M L^2)^2 (-\frac{1}{12} L_M^2 - t_{piezo}^2 + t_{piezo} t_M - \frac{1}{3} t_M^2)$$

$$\tilde{B} = (\rho_M b L_M t_M L)\left[\left(\frac{-\tilde{d}_{31}^2 b t_{piezo}^3 L^2}{2(\tilde{s}_{11}^E)^2 \tilde{\epsilon}_{33}^S}\right) + \overline{EI}(4L^2 + 6L_M L + 4L_M^2 + 12t_{piezo}^2 - 12t_{piezo}t_M + 4t_M^2)\right]$$

$$\tilde{C} = \overline{EI}\left(-12\overline{EI} + \frac{6\tilde{d}_{31}^2 b t_{piezo}^3}{(\tilde{s}_{11}^E)^2 \tilde{\epsilon}_{33}^S}\right)$$

A.4 20-phon contour conversion to umbo acceleration

From Fig. 1.3 and BS ISO 226:2003, we extract the 20-phon sound pressure levels, L_{dB} (dB SPL), and convert them to pressure, $P_{\text{20-phon}}$ (Pa), using the following equation:

$$L_{dB} = 20\log_{10}\left(\frac{P_{\text{20-phon}}}{P_0}\right),$$

where $P_0 = 20$ µPa for air.

Then, we use the umbo displacement data (m) measured at various frequencies with a 30 dB SPL stimulus (6.324×10^{-4} Pa) from Sachse et al. (2013) and Goode et al. (1996). We convert this displacement data to umbo acceleration values in units m/s^2 by multiplying with ω^2. Each ω value corresponds to the measured frequency of each displacement point. We then divide these acceleration values by the input stimulus (6.324×10^{-4} Pa) to normalize by the pressure (m/s^2/Pa).

Next, for each corresponding frequency, we can multiply these acceleration values normalized by the pressure (m/s^2/Pa) with the calculated $P_{\text{20-phon}}$ (Pa). The resulting values are the target 20-phon umbo acceleration values, $MDA_z^{\text{20-phon}}$, in units m/s^2. Recall that BS ISO 226:2003 uses a 1-2 second duration of a tone to investigate the 20-phon contour, which is consistent with our use of a 1 Hz bandwidth for the sensor noise spectral density that is used to calculate the theoretical MDA_z with units of $m/s^2/\sqrt{Hz}$.

A.5 Dual-, three-, five-, and eight-bandwidth sensors

Table A.1: Dual-bandwidth sensor dimensions with constrained proof mass thicknesses. The sensor area is 1.84 $\times$ 10^{-7} m^2, and the estimated MEMS die dimensions are 763 µm $\times$ 1,014 µm with a MEMS die area of 7.74 $\times$ 10^{-7} m^2.

	LFSE	HFSE
t_M (µm)	100	100
L_M (µm)	300	50
L (µm)	52	51
b (µm)	347	614
Sub-Bandwidth Frequencies (kHz)	0.1 - 1.25	1.25 - 8

Table A.2: Three-bandwidth sensor dimensions with unconstrained proof mass thicknesses. The sensor area is 7.19 $\times$ 10^{-8} m^2, and the estimated MEMS die dimensions are 691 µm $\times$ 645 µm with a MEMS die area of 4.46 $\times$ 10^{-7} m^2.

	LFSE	MFSE	HFSE
t_M (µm)	210	110	60
L_M (µm)	290	130	80
L (µm)	51	52	52
b (µm)	90	134	127
Sub-Bandwidth Frequencies (kHz)	0.1 - 0.8	0.8 - 3.15	3.15 - 8

Table A.3: Three-bandwidth sensor dimensions with constrained proof mass thicknesses. The sensor area is 9.93×10^{-8} m^2, and the estimated MEMS die dimensions are 755 µm × 673 µm with a MEMS die area of 5.08×10^{-7} m^2.

	LFSE	MFSE	HFSE
t_M (µm)	100	100	100
L_M (µm)	300	140	50
L (µm)	102	51	51
b (µm)	135	128	204
Sub-Bandwidth Frequencies (kHz)	0.1 - 0.8	0.8 - 3.15	3.15 - 8

Table A.4: Five-bandwidth sensor dimensions with unconstrained proof mass thicknesses. The sensor area is 3.28×10^{-8} m^2, and the estimated MEMS die dimensions are 742 µm × 582 µm with a MEMS die area of 4.32×10^{-7} m^2.

	LFSE	MFSE_1	MFSE_2	MFSE_3	HFSE
t_M (µm)	300	210	170	90	60
L_M (µm)	300	290	220	120	80
L (µm)	92	51	53	52	52
b (µm)	17	21	8	46	67
Sub-Bandwidth Frequencies (kHz)	0.1 - 0.4	0.4 - 0.8	0.8 - 1.25	1.25 - 4	4 - 8

Table A.5: Eight-bandwidth sensor dimensions with unconstrained proof mass thicknesses. The sensor area is 2.55×10^{-8} m^2, and the estimated MEMS die dimensions are 783 µm × 607 µm with a MEMS die area of 4.75×10^{-7} m^2.

	LFSE	$MFSE_1$	$MFSE_2$	$MFSE_3$	$MFSE_4$	$MFSE_5$	$MFSE_6$	HFSE
t_M (µm)	300	300	210	170	110	80	70	60
L_M (µm)	300	300	290	220	130	100	90	80
L (µm)	133	64	51	53	52	55	53	53
b (µm)	10	11	11	8	23	32	11	4
Sub-Bandwidth Frequencies (kHz)	0.1 - 0.315	0.315 - 0.5	0.5 - 0.8	0.8 - 1.25	1.25 - 3.15	3.15 - 5	5 - 6.3	6.3 - 8

A.6 Noise floor of constrained four-bandwidth sensor in dB SPL and dBA

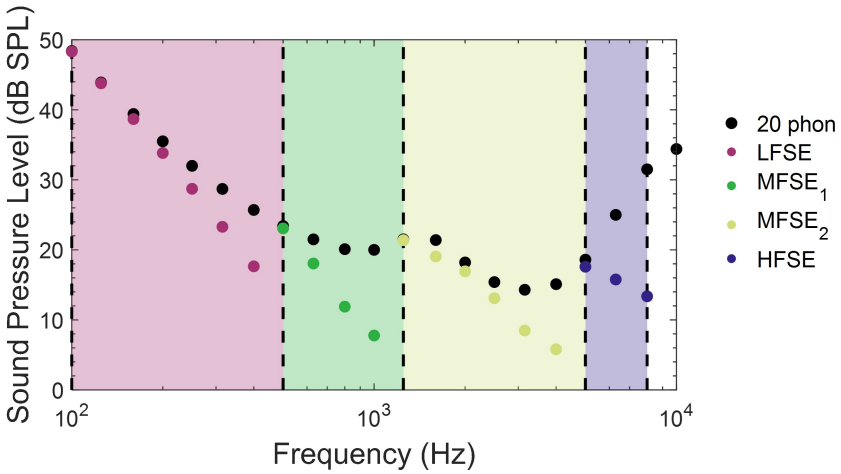

Figure A.1: Noise floor in dB SPL of four-bandwidth sensor with constrained proof mass thicknesses in comparison with the 20-phon equal-loudness-level contour from BS ISO 226:2003.

The graph below compares the noise in dBA of the four-bandwidth sensor with two commercial Knowles® hearing-aid microphones: the EM microphone and the improved EM (IEM) microphone (Knowles, 2025).

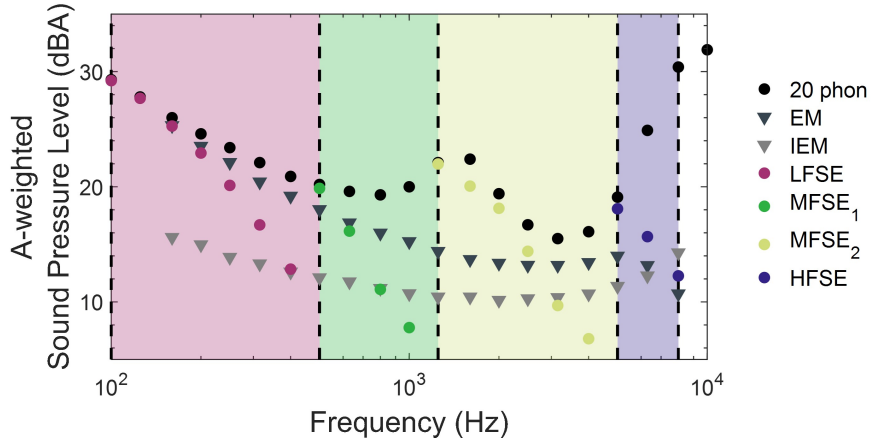

Figure A.2: A-weighted noise floor in dBA of four-bandwidth sensor with constrained proof mass thicknesses in comparison with the 20-phon equal-loudness-level contour from BS ISO 226:2003, and with two Knowles® microphones (Knowles, 2025).

A.7 Closed-circuit sensitivity and noise

In Section 2.3.3.1, we calculated the open-circuit sensitivity where $Q^c = 0$. The open circuit is a Thevenin equivalent circuit where each piezoelectric layer is represented as a parallel resistor-capacitor, and the Johnson noise is given in Eq. 2.24. For the closed-circuit sensitivity, $V_{out} = 0$ and $Q^c = I/\omega$, where I is the current. Thus, Eq. 2.13 is zero and Eq. 2.19 is updated as:

$$Q^c = \frac{\tilde{d}_{31} b t_{piezo}}{\tilde{s}_{11}^E} \left(\frac{dW(L)}{dx} - \frac{dW(0)}{dx} \right)$$

The closed circuit is a Norton equivalent circuit. We can transform a Thevenin equivalent circuit to a Norton equivalent circuit and vice versa by first knowing that the impedance stays the same in both cases (it is in series with the voltage source for the Thevenin equivalent circuit and in parallel with the current source for the Norton equivalent circuit). The current for a Norton equivalent circuit is equal to the Thevenin voltage divided by the impedance:

$$I_{no} = \frac{V_{th}}{Z}$$

where Z is the total impedance of the piezoelectric layer. Thus, the sensor noise spectral density in 1 Hz bandwidths for the closed circuit in units of A^2/Hz is:

$$\overline{i_n^2} = Re\left(\frac{\overline{v_n^2}}{Z^2} \right),$$
$$\overline{i_n^2} = \frac{4 k_B T^*}{R}$$

where R is the parallel resistance, $R = 1/(\omega C \tan\delta)$ (Hake, 2021). The closed-circuit sensitivity is calculated using the current instead of the voltage as $S(f) = Q^c(f)/\ddot{W}_{bz}$ in units of $\mathrm{C}/(\mathrm{m}/\mathrm{s}^2)$:

$$\lim_{\omega \to 0} S(f) = \left| \frac{-3M\tilde{d}_{31}\tilde{\epsilon}_{33}^S \tilde{s}_{11}^E L(L_M + L)}{t_{piezo}^2 (\tilde{d}_{31}^2 + 4\tilde{\epsilon}_{33}^S \tilde{s}_{11}^E)} \right|$$

Then, the closed-circuit MDA is derived from $MDA = |\sqrt{\overline{i_n^2}}/(\omega S(f))|$ with units of $(\mathrm{m/s^2})/\sqrt{\mathrm{Hz}}$:

$$MDA_z = \left| \sqrt{\frac{8k_BT}{9}} \underbrace{\frac{1}{\sqrt{\omega}}}_{\text{Frequency}} \underbrace{\frac{(\tilde{d}_{31}^2 + 4\tilde{\epsilon}_{33}^S \tilde{s}_{11}^E)\sqrt{\tan\delta}}{\tilde{d}_{31}\tilde{s}_{11}^E \rho_M \sqrt{\tilde{\epsilon}_{33}^S}}}_{\text{Material properties}} \underbrace{\frac{\sqrt{t_{piezo}^3}}{L_M t_M \sqrt{bL}(L + L_M)}}_{\text{Sensing plate and proof mass dimensions}} \right|.$$

APPENDIX B

Appendix for Chapter 2

B.1 Extracting material properties

For the work presented in Chapter 3, we adjust the $\tan\delta$ and $\tilde{d}_{31}$ values based on the varied piezoelectric thickness using data presented in Martin et al. (2004). Below are the steps we used to derive the values in this work (Littrell, 2010).

For $\tan\delta$, we simply extracted the values presented in Figure 6 of Martin et al. (2004) and interpolated them using the pchip method in MATLAB®.

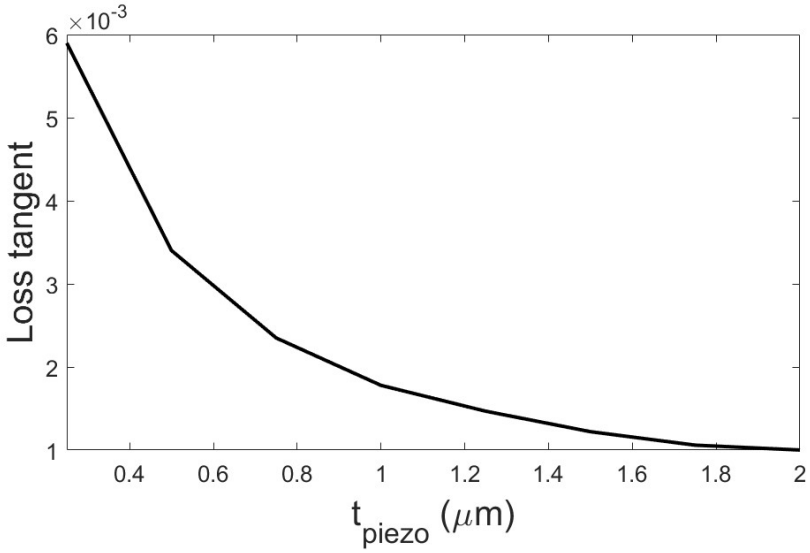

Figure B.1: Loss tangent, $\tan\delta$, as a function of t_{piezo}.

For $\tilde{d}_{31}$, we first extracted the values of $d_{33,f}$ presented in Figure 7(a) of Martin et al. (2004), where $d_{33,f}$ is the effective clamped longitudinal piezoelectric coefficient and d_{31} is the transverse. Then, we used the following equation to calculate d_{31}, assuming that $d_{31} \approx d_{33}/2$ (Olsson et al., 2020):

$$d_{33} = d_{33,f} + \frac{2s_{13}^E}{s_{11}^E s_{12}^E} d_{31}$$

which can be rewritten as:

$$d_{31} = d_{33,f}\left[2 - \frac{2s_{13}^E}{s_{11}^E s_{12}^E}\right]^{-1}$$

where we extracted the values of s_{13}^E, s_{11}^E, and s_{12}^E directly from COMSOL Multiphysics® for AlN. Hence, we can solve for d_{31} and then use the plane-strain equivalent from Section 2.3.3 to obtain $\tilde{d}_{31}$. Recall that d_{31} is normally a negative value (Hake et al., 2023; Zhang et al., 2022; Tsubouchi and Mikoshiba, 1985).

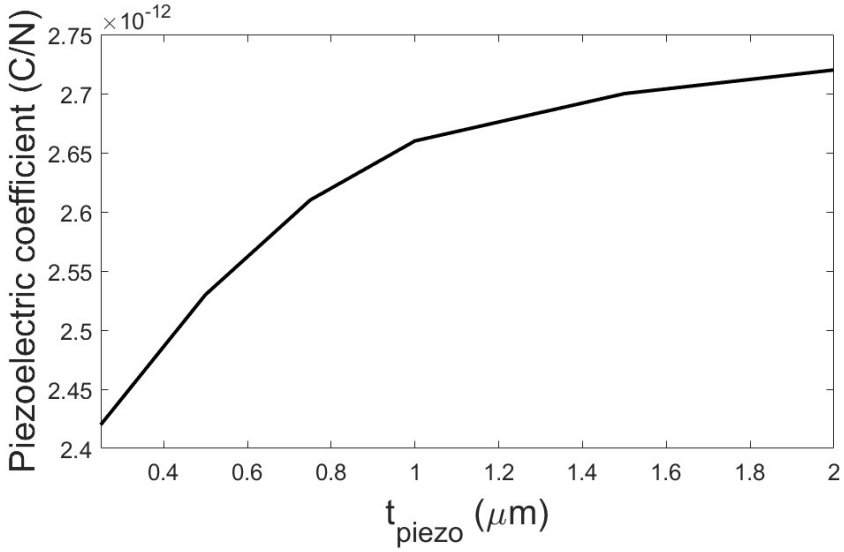

Figure B.2: Piezoelectric coefficient, $|\tilde{d}_{31}|$, as a function of t_{piezo}.

APPENDIX C

Appendix for Chapter 3

C.1 Deriving the third-order Padé approximation

The formula for the Padé approximation is given by (Khodier, 2000):

$$P_{m,n} = \frac{\sum_{i=0}^{m} a_i x^i}{1 + \sum_{k=0}^{n} b_k x^k}$$

where for the third-order it becomes:

$$P_{3,3} = \frac{a_0 + a_1 x + a_2 x^2 + a_3 x^3}{1 + b_1 x + b_2 x^2 + b_3 x^3}$$

To determine the coefficients $a_0 - a_3$ and $b_1 - b_3$, we need to equate the Padé approximation to the Taylor series expansion for e^{-x}. The Taylor series is given by (Alves de Sá and Louro, 2024):

$$e^{-x} = \sum_{j=0}^{\infty} \frac{(-x)^j}{j!}$$

We must expand the Taylor series up to the order of $m + n = 6$. Then, solve for the unknown coefficients in the Padé approximation, ignoring any higher-order variables in the Taylor expansion.

BIBLIOGRAPHY

Aibara, R., J. T. Welsh, S. Puria, and R. L. Goode (2001). Human middle-ear sound transfer function and cochlear input impedance. *Hearing Research 152*(1), 100–109.

Alhabib, S. F., Y. Abdelsamad, R. S. Badghaish, F. Alzhrani, A. Hagr, and F. Almuhawas (2021). Cochlear implant: More hearing better speech performance. *nternational Journal of Pediatric Otorhinolaryngology 150*, 110896.

Alves de Sá, A. and B. Louro (2024). *Sequences and Series* (1st ed.). Springer Cham.

Babajanian, E. E., J. R. Dornhoffer, and C. L. W. Driscoll (2024). Fully implanted cochlear implants. *Current Otorhinolaryngology Reports 12*, 61–65.

Baker, G. A. J. and P. Graves-Morris (1996). *Padé approximants* (2nd ed.). Cambridge University Press.

Banakis Hartl, R. M. and H. A. Jenkins (2020). Implantable hearing aids: Where are we in 2020? *Laryngoscope Investigative Otolaryngology 5*, 1184–1191.

Berlincourt, D. A., D. R. Curran, and H. Jaffe (1964). Piezoelectric and piezomagnetic materials and their function in transducers. In W. P. Mason (Ed.), *Physical Acoustics: Principles and Methods*, Volume 1, Chapter 3, pp. 169–270. Academic Press.

Bramsløw, L. (2010). Preferred signal path delay and high-pass cut-off in open fittings. *International Journal of Audiology 49*(9), 634–644.

Briggs, R. J. S., H. C. Eder, P. M. Seligman, R. S. C. Cowan, K. L. Plant, J. Dalton, D. K. Money, and J. F. Patrick (2008). Initial clinical experience with a totally implantable cochlear implant research device. *Otology & Neurotology 29*(2), 114 – 119.

Bruschini, L., F. Forli, A. Santoro, P. Bruschini, and S. Berrettini (2009). Fully implantable otologics MET carina device for the treatment of sensorineural hearing loss. preliminary surgical and clinical results. *Acta Otorhinolaryngol Ital 29*(2), 79–85.

BS ISO 226:2003 (2003). *Acoustics - Normal equal-loudness-level contours*. BSI: London, UK.

Burovikhin, D., P. Kitsopoulos, M. Lauxmann, and K. Grosh (2024). Optimal position and orientation of an ossicular accelerometer for human auditory prostheses. *Sensors 24*(24), 8084.

Békésy, G. v. (1960). *Experiments in Hearing*, pp. 102. New York: McGraw-Hill.

Calero, D., S. Paul, A. Gesing, F. Alves, and J. A. Cordioli (2018). A technical review and evaluation of implantable sensors for hearing devices. *BioMedical Engineering On-Line 17*(23).

Chen, D. A., D. D. Backous, M. A. Arriaga, R. Garvin, D. Kobylek, T. Littman, S. Walgren, and D. Lura (2004). Phase 1 clinical trial results of the envoy system: A totally implantable middle ear device for sensorineural hearing loss. *Otolaryngology–Head and Neck Surgery 131*(6), 904–916.

Chen, H., T. Okumura, S. Emura, and S. Shoumura (2008). Scanning electron microscopic study of the human auditory ossicles. *Annals of Anatomy - Anatomischer Anzeiger 190*(1), 53–58.

Cleveland Clinic (2023). Hearing Loss. https://my.clevelandclinic.org/health/diseases/17673-hearing-loss. Accessed on Feb. 14 2025.

Cleveland Clinic (2024). Conductive Hearing Loss. https://my.clevelandclinic.org/health/diseases/conductive-hearing-loss. Accessed on Feb. 14 2025.

Cohen, N. L. and J. T. J. Roland (2006). Complications of cochlear implant surgery. In S. B. Waltzman and J. T. J. Roland (Eds.), *Cochlear Implants* (2nd ed.)., Chapter 10, pp. 126–132. Thieme.

Cremer, L. and M. Heckl (1988). *Structure-Borne Sound: Structural Vibrations and Sound Radiation at Audio Frequencies* (2nd ed.). Springer Berlin.

Cunningham, L. L. and D. L. Tucci (2017). Hearing loss in adults. *The New England Journal of Medicine 377*(25), 2465–2473.

Denk, F., S. D. Ewert, and B. Kollmeier (2018). Spectral directional cues captured by hearing device microphones in individual human ears. *J. Acoust. Soc. Am. 144*(4), 2072–2087.

Deo, N. V. (2006). *Micro and macro-mechanics of the mammalian cochlea*. Ph. D. thesis, University of Michigan.

D'Haese, P. (2020). First surgeries ever in Europe with a totally implantable cochlear implant. https://www.medel.com/press-room/press-list/press-details/2020/10/19/first-surgeries-ever-in-europe-with-a-totally-implantable-cochlear-implant. Accessed on Feb. 19 2025.

Envoy Medical (2024). Envoy Medical Receives FDA Approval to Initiate Pivotal Clinical Study for Breakthrough Hearing Device. https://www.envoymedical.com/news/envoy-medical-recieves-fda-approval-to-initiate-pivotal-clinical-study-for-breakthrough-hearing-device. Accessed on Feb. 19 2025.

Fan, Q., Y. Zhai, J. Li, Y. Zhang, J. Ma, W. Wang, and C. Wang (2022). MEMS piezoelectric bionic directional sound sensor based on ZnO thin film. *Sensors and Actuators: A. Physical 347*, 113971.

Feng, B. and R. Z. Gan (2004). Lumped parametric model of the human ear for sound transmission. *Biomechanics and Modeling in Mechanobiology 3*, 33–47.

Ferguson, M. A., P. T. Kitterick, L. Y. Chong, M. Edmondson-Jones, F. Barker, and D. J. Hoare (2017). Hearing aids for mild to moderate hearing loss in adults. *Cochrane Database of Systematic Reviews* (9), CD012023.

Fiedler, H., J. Leveneur, M. Nancarrow, D. R. G. Mitchell, and J. Kennedy (2021). Effect of long-term stability of the aluminium nitride - silicon interface for microwave-frequency electronic devices. *Applied Surface Science 551*, 149461.

Gan, R. Z., T. Cheng, C. Dai, F. Yang, and M. W. Wood (2009). Finite element modeling of sound transmission with perforations of tympanic membrane. *The Journal of the Acoustical Society of America 126*(1), 243–253.

Gan, R. Z., M. W. Wood, and K. J. Dormer (2004). Human middle ear transfer function measured by double laser interferometry system. *Otology & Neurotology 25*(4), 423—435.

Gerard, J. M., M. P. Thill, G. Chantrain, M. Gersdorff, and N. Deggouj (2012). Esteem 2 middle ear implant: Our experience. *Audiology and Neurotology 17*(4), 267–274.

Gere, J. M. and B. J. Goodno (2012). *Mechanics of Materials* (8th ed.). Cengage Learning.

Goode, R., G. Ball, S. Nishihara, and K. Nakamura (1996). Laser doppler vibrometer (ldv)–a new clinical tool for the otologist. *The American Journal of Otology 17*(6), 813–822.

Graf, L., J. Lochner, H. Mojallal, A. Arnold, F. Honegger, and C. Stieger (2022). Comparison between incus short process and long process coupling of the vibrant soundbridge in human temporal bones. *International Journal of Audiology 62*(2), 192–198.

Graff, K. F. (1975). Flexural waves in thin rods. In *Wave Motion in Elastic Solids*, pp. 140–212. Dover Publications, Inc.

Grégoire, A., J.-P. Van Damme, C. Gilain, B. Bihin, and P. Garin (2018). Our auditory results using the Vibrant Soundbridge on the long process of the incus: 20 years of data. *Auris Nasus Larynx 45*, 66–72.

Haile, L. M., K. Kamenov, P. S. Briant, A. U. Orji, J. D. Steinmetz, A. Abdoli, (...), and S. Chadha (2021). Hearing loss prevalence and years lived with disability, 1990-2019: findings from the global burden of disease study 2019. *The Lancet 397*(10278), 996–1009.

Hake, A. E. (2021). *Piezoelectric MEMS Accelerometers for Sensing Ossicular Vibration*. Ph. D. thesis, University of Michigan.

Hake, A. E., P. Kitsopoulos, and K. Grosh (2023). Design of piezoelectric dual-bandwidth accelerometers for completely implantable auditory prostheses. *IEEE Sensors Journal 23*(13), 13957–13965.

Hake, A. E., C. Zhao, W.-K. Sung, and K. Grosh (2021). Design and experimental assessment of low-noise piezoelectric microelectromechanical systems vibration sensors. *IEEE Sensors Journal 21*(16), 17703–17711.

Han, H., L. Wang, Y. Zhu, Z. Liu, Y. Sun, J. Wang, L. Wang, S. Xiang, H. Shi, and Q. Ding (2023). Finite element analysis of conductive hearing loss caused by fixation and detachment of ligament and tendon in the middle ear. *Computer Methods and Programs in Biomedicine 236*(107540).

Hawkins, J. E. (2024). Human Ear. https://www.britannica.com/science/ear. Accessed on Dec. 26, 2024.

Holder, J. T. and R. Gifford (2021). Effect of increased daily cochlear implant use on auditory perception in adults. *Journal of Speech, Language, and Hearing Research 64*(10), 4022–4055.

Holder, J. T., L. S. Mayberry, and R. Gifford (2022). The cochlear implant use questionnaire: Assessing habits and barriers to use. *Otology & Neurotology 43*(1), e23–e29.

Jamal, A., A. Alsabea, and T. M. (2022). Effect of ear infections on hearing ability: A narrative review on the complications of otitis media. *Cureus 14*(7), e27400.

Jia, X.-H., N. Gao, X.-d. Xu, Y.-Z. Wu, H.-Y. Kang, and F.-L. Chi (2016). A new floating piezoelectric microphone for the implantable middle ear microphone in experimental studies. *Acta Oto-Laryngologica 136*(12), 1248–1254.

Johns Hopkins Medicine (2025). Types of Hearing Loss. https://www.hopkinsmedicine.org/health/conditions-and-diseases/hearing-loss/types-of-hearing-loss. Accessed on Feb. 14 2025.

Kanegaonkar, R. G. and M. Whittaker (2015). The anatomy of hearing. In *Hearing: An Introduction & Practical Guide* (1st ed.)., Chapter 1, pp. 3–11. CRC Press.

Kanno, I., J. Ouyang, J. Akedo, T. Yoshimura, B. Malič, and P. Muralt (2023). Piezoelectric thin films for MEMS. *Applied Physics Letters 122*, 090401.

Katz, R. N., G. Wechsler, H. Toutanji, D. Friel, G. L. Leatherman, T. Elkorchi, and W. Rafaniello (1993). Room temperature tensile strength of AlN. In J. B. W. Jr. (Ed.), *Ceramic Engineering and Science Proceedings*, Volume 14, Chapter 30, pp. 282 – 291. The American Ceramic Society.

Khodier, A. M. M. (2000). Perturbed padé approximation. *International Journal of Computer Mathematics 74*(2), 247–253.

Knowles Electronics Inc. (2025). Improved EM microphone, TB-25. Accessed on Mar. 27 2024.

Krommer, M. (2001). On the correction of the Bernoulli-Euler beam theory for smart piezoelectric beams. *Smart Materials and Structures 10*(4), 668–680.

Kumar, A., A. Varghese, A. Sharma, M. Prasad, V. Janyani, R. Yadav, and K. Elgaid (2022). Recent development and futuristic applications of MEMS based piezoelectric microphones. *Sensors and Actuators A: Physical 347*, 113887.

Labassi, S., M. Beliaeff, V. Péan, and P. V. de Heyning (2017). The Vibrant Soundbridge® middle ear implant: A historical overview. *Cochlear Implants International 18*(6), 314–323.

Lelic, D., G. Stiefenhofer, E. Lundorff, and T. Neher (2022). Hearing aid delay in open-fit devices: Preferred sound quality in listeners with normal and impaired hearing. *JASA Express Letters 2*(10), 104803.

Li, C.-M., X. Zhang, H. J. Hoffman, M. F. Cotch, C. L. Themann, and M. R. Wilson (2014). Hearing Impairment Associated With Depression in US Adults, National Health and Nutrition Examination Survey 2005-2010. *JAMA Otolaryngology–Head & Neck Surgery 140*(4), 293–302.

Lin, F. R., K. Yaffe, J. Xia, Q.-L. Xue, T. B. Harris, E. Purchase-Helzner, S. Satterfield, H. N. Ayonayon, L. Ferrucci, and E. M. Simonsick (2013). Hearing Loss and Cognitive Decline in Older Adults. *JAMA Internal Medicine 173*(4), 293–299.

Littrell, R. and K. Grosh (2012). Modeling and characterization of cantilever-based MEMS piezoelectric sensors and actuators. *Journal of Microelectromechanical Systems 21*(2), 406–413.

Littrell, R. J. (2010). *High Performance Piezoelectric MEMS Microphones*. Ph. D. thesis, University of Michigan.

Liu, C. (2012). *Foundations of MEMS* (2nd ed.). Prentice Hall.

Livingston, G., A. Sommerlad, V. Orgeta, S. G. Costafreda, J. Huntley, D. Ames, C. Ballard, S. Banerjee, A. Burns, J. Cohen-Mansfield, C. Cooper, N. Fox, L. N. Gitlin, R. Howard, H. C. Kales, E. B. Larson, K. Ritchie, K. Rockwood, E. L. Sampson, Q. Samus, L. S. Schneider, G. Selbæk, L. Teri, and N. Mukadam (2017). Dementia prevention, intervention, and care. *The Lancet 390*(10113), 2673–2734.

LNF University of Michigan Wiki (2025). Endeavor M1 AlN sputter tool. https://lnf-wiki.eecs.umich.edu/wiki/Endeavor_M1_AlN_Sputter_Tool. Accessed on Mar. 25 2025.

Lou, L., H. Yu, M. T. X. Haw, S. Zhang, and Y. A. Gu (2016). Comparative characterization of bimorph and unimorph AlN piezoelectric micro-machined ultrasonic transducers. *2016 IEEE 29th International Conference on Micro Electro Mechanical Systems (MEMS)*, 1090–1093.

Lurie Nanofabrication Facility (2025). LNF Fees and Rates. https://lnf.engin.umich.edu/lnf-fees-and-rates/. Accessed on Mar. 25 2025.

Mankekar, G. (Ed.) (2014). *Implantable Hearing Devices other than Cochlear Implants* (1st ed.). Springer.

Martin, F., P. Muralt, M.-A. Dubois, and A. Pezous (2004). Thickness dependence of the properties of highly c-axis textured AlN thin films. *Journal of Vacuum Science & Technology A 22*(2), 361–365.

Marzo, S. J., J. M. Sappington, and J. A. Shohet (2014). The envoy esteem implantable hearing system. *Otolaryngologic Clinics of North America 47*(6), 941–952.

McKinnon, B. J. (2010). Vibrant soundbridge implantation: the transmastoid/posterior tympanotomy and transcanal approaches. *Operative Techniques in Otolaryngology-Head and Neck Surgery 21*(3), 189–193.

McRackan, T. R., W. B. Clinkscales, J. B. Ahlstrom, S. A. Nguyen, and J. R. Dubno (2018). Factors associated with benefit of active middle ear implants compared to conventional hearing aids. *The Laryngoscope 128*(9), 2133–2138.

Miller, S. A. (2004). Hearing aid with internal acoustic middle ear transducer. U.S. Patent 6726618B2.

Mlynski, R., E. Dalhoff, A. Heyd, D. Wildenstein, K. Rak, A. Radeloff, R. Hagen, A. W. Gummer, and S. P. Schraven (2015). Standardized active middle-ear implant coupling to the short incus process. *Otology & Neurotology 36*(8), 1390–1398.

Monini, S., A. Bianchi, R. Talamonti, F. Atturo, C. Filippi, and M. Barbara (2016). Patient satisfaction after auditory implant surgery: ten-year experience from a single implanting unit center. *Acta Oto-Laryngologica 137*(4), 389–397.

Mueller, H. G., T. Ricketts, and R. Bentler (2014). *Modern Hearing Aids: Pre-Fitting Testing and Selection Considerations* (1st ed.). Plural Publishing, Inc.

Møller, A. R. (2006). *Hearing: Anatomy, Physiology, and Disorders of the Auditory System* (2nd ed.). Academic Press.

Nachtegaal, J., J. Festen, and S. Kramer (2011). Hearing ability and its relationship with psychosocial health, work-related variables, and health care use: the national longitudinal study on hearing. *Audiology Research 1*(1), e9.

Narayanan, D. A., R. Raman, and A. W. Chong (2019). The role of occlusion of the external ear canal in hearing loss. *Turk Arch Otorhinolaryngol 57*(3), 122–126.

Nassiri, A. M., D. L. Sorkin, and M. L. Carlson (2022). Current estimates of cochlear implant utilization in the united states. *Otology & Neurotology 43*(5), e558–e562.

National Academies of Sciences, Engineering, and Medicine (2016). *Hearing Health Care for Adults: Priorities for Improving Access and Affordability*. Washington, DC: The National Academies Press.

National Institute on Deafness and Other Communication Disorders (NIDCD) (2022). Hearing Aids. https://www.nidcd.nih.gov/health/hearing-aids. Accessed on Feb. 17 2025.

National Institute on Deafness and Other Communication Disorders (NIDCD) (2024a). Cochlear Implants. https://www.nidcd.nih.gov/health/cochlear-implants. Accessed on Feb. 18 2025.

National Institute on Deafness and Other Communication Disorders (NIDCD) (2024b). Quick Statistics About Hearing, Balance, & Dizziness. https://www.nidcd.nih.gov/health/statistics/quick-statistics-hearing. Accessed on Feb. 17 2025.

Nocedal, J. and S. J. Wright (2006). *Numerical Optimization* (2nd ed.). Springer, NY.

Noussios, G., P. Chouridis, L. Kostretzis, and K. Natsis (2016). Morphological and morphometrical study of the human ossicular chain: A review of the literature and a meta-analysis of experience over 50 years. *Journal of Clinical Medicine Research 8*(2), 76–83.

Olsson, R. H., Z. Tang, and M. D'Agati (2020). Doping of aluminum nitride and the impact on thin film piezoelectric and ferroelectric device performance. In *2020 IEEE Custom Integrated Circuits Conference (CICC)*, pp. 1–6.

O'Connor, K. N. and S. Puria (2006). Middle ear cavity and ear canal pressure-driven stapes velocity responses in human cadaveric temporal bones. *The Journal of the Acoustical Society of America 120*(3), 1517–1528.

PCB Universe (2024). Printed Circuit Boards, Rigid PCBs. https://www.pcbuniverse.com/pcbu-products.php. Accessed on Apr. 22 2024.

Pelosi, S., M. L. Carlson, and M. E. Glasscock (2014). The Ototronix MAXUM system: Indications, techniques, and outcomes. *Operative Techniques in Otolaryngology-Head and Neck Surgery 25*(4), 338–343.

Pulcherio, J. O. B., A. G. Bittencourt, P. R. Burke, R. d. C. Monsanto, R. de Brito, R. K. Tsuji, and R. F. Bento (2014). Carina® and Esteem®: A systematic review of fully implantable hearing devices. *PLoS One 9*(10), e110636.

Puria, S. (2013). Middle ear hearing devices. In S. Puria, R. R. Fay, and A. N. Popper (Eds.), *The Middle Ear Science, Otosurgery, and Technology*, pp. 273–308. Springer.

Puria, S., W. T. Peake, and J. J. Rosowski (1997). Sound-pressure measurements in the cochlear vestibule of human-cadaver ears. *The Journal of the Acoustical Society of America 101*(5), 2754–2770.

Sachse, M., W. Hortschitz, M. Stifter, H. Steiner, and T. Sauter (2013). Design of an implantable seismic sensor placed on the ossicular chain. *Medical Engineering & Physics 35*(10), 1399–1405.

Salmon, M. K., J. Brant, M. H. Hohman, and D. Leibowitz (2023). Audiogram Interpretation. https://www.ncbi.nlm.nih.gov/books/NBK578179/. Accessed on Feb. 14 2025.

Samco Inc. (2024). Introduction to Si-DRIE (Silicon Deep Reactive Ion Etching). https://www.samcointl.com/opto/introduction-to-si-drie-silicon-deep-reactive-ion-etching/. Accessed on Dec. 26 2024.

Sanna, M., P. Merkus, R. Free, and M. Falcioni (2016). Cochlear implantation. In *Surgery for Cochlear and Other Auditory Implants* (1st ed.)., Chapter 5, pp. 66–89. Thieme.

Sanna, M., H. Sunose, F. Mancini, A. Russo, A. Taibah, and M. Falcioni (2012a). Cochlear implantation. In *Middle Ear and Mastoid Microsurgery* (2nd ed.)., Chapter 19, pp. 549–584. Thieme.

Sanna, M., H. Sunose, F. Mancini, A. Russo, A. Taibah, and M. Falcioni (2012b). Simple mastoidectomy. In *Middle Ear and Mastoid Microsurgery* (2nd ed.)., Chapter 12, pp. 245–247. Thieme.

Schraven, S. P., R. Mlynski, E. Dalhoff, A. Heyd, D. Wildenstein, K. Rak, A. Radeloff, R. Hagen, and A. W. Gummer (2016). Coupling of an active middle-ear implant to the long process of the incus using an elastic clip attachment. *Hearing Research 340*, 179–184.

Schuster-Bruce, J. and E. Gosnell (2022). Conventional Hearing Aid Indications and Selection. https://www.ncbi.nlm.nih.gov/books/NBK567712/. Accessed on Feb. 17 2025.

Sim, J. and S. Puria (2008). Soft tissue morphometry of the malleus–incus complex from micro-ct imaging. *Journal of the Association for Research in Otolaryngology 9*, 5–21.

Stenfelt, S. (2006). Middle ear ossicles motion at hearing thresholds with air conduction and bone conduction stimulation. *The Journal of the Acoustical Society of America 119*(5), 2848–2858.

Stenfelt, S. and R. L. Goode (2005). Bone-conducted sound: physiological and clinical aspects. *Otology & Neurotology 26*(6), 1245–1261.

Stiefenhofer, G. (2023). Hearing aid delay in open-fit devices – coloration-pitch discrimination in normal-hearing and hearing-impaired. *International Journal of Audiology 62*(5), 424–432.

Stieger, C., D. Djeric, M. Kompis, L. Remonda, and R. Häusler (2006). Anatomical study of the human middle ear for the design of implantable hearing aids. *Auris Nasus Larynx 33*(4), 375–380.

Sutton, A. E., R. J. Krogmann, and Y. A. Khalili (2025). Cochlear Implants. https://www.ncbi.nlm.nih.gov/books/NBK544280/. Accessed on Feb. 18 2025.

Tadigadapa, S. and F. Lärmer (2011). Dry etching for micromachining applications. In R. Ghodssi and P. Lin (Eds.), *MEMS Materials and Processes Handbook*, Volume 1, pp. 403–456. Springer.

Tanna, R. J., J. W. Lin, and O. D. Jesus (2023). Sensorineural Hearing Loss. https://www.ncbi.nlm.nih.gov/books/NBK565860/. Accessed on Feb. 14 2025.

Trudel, M. and D. P. Morris (2022). The remaining obstacles for a totally implantable cochlear implant. *Current opinion in Otolaryngology & Head and Neck Surgery 30*(5), 298–302.

Tsubouchi, K. and N. Mikoshiba (1985). Zero-temperature-coefficient SAW devices on AlN epitaxial films. *IEEE Transactions on Sonics and Ultrasonics 32*(5), 634–644.

Udagatti, V. D. and R. Dinesh Kumar (2016). Endoscopic ear surgery: Critical review of anatomy and physiology of normal and reconstructive middle ear. *Indian Journal of Otolaryngology and Head & Neck Surgery 68*, 157–162.

Walker, J. J., L. M. Cleveland, J. L. Davis, and J. S. Seales (2013). Audiometry screening and interpretation. *American family physician 87*(1), 41–47.

Wang, Q.-M. and L. E. Cross (1998). Performance analysis of piezoelectric cantilever bending actuators. *Ferroelectrics 215*(1), 187–213.

Wang, Q.-M., Z. Yang, F. Li, and P. Smolinski (2004). Analysis of thin film piezoelectric microaccelerometer using analytical and finite element modeling. *Sensors and Actuators: A. Physical 113*, 1–11.

Wever, E. G. and M. Lawrence (1954). *Physiological Acoustics*, pp. 113. New Jersey: Princeton University Press.

Wils, I., A. Geerardyn, T. Putzeys, K. Denis, and N. Verhaert (2023). Lumped element models of sound conduction in the human ear: A systematic review. *The Journal of the Acoustical Society of America 154*(3), 1696–1709.

World Health Organization (WHO) (2024). Deafness and hearing loss. https://www.who.int/news-room/fact-sheets/detail/deafness-and-hearing-loss. Accessed on Dec. 26 2024.

Yeiser, A. J., E. F. Wawrzynek, J. Z. Zhang, L. Graf, C. I. McHugh, I. Kymissis, E. S. Olson, J. H. Lang, and H. H. Nakajima (2024). The UmboMic: a PVDF cantilever microphone. *Journal of Micromechanics and Microengineering 34*(085010).

Yip, M., R. Jin, H. H. Nakajima, K. M. Stankovic, and A. P. Chandrakasan (2015). A fully-implantable cochlear implant SoC with piezoelectric middle-ear sensor and arbitrary waveform neural stimulation. *IEEE Journal of Solid-State Circuits 50*(1), 214–229.

Yost, W. A. (2000). *Fundamentals of Hearing: An Introduction* (4th ed.). Academic Press.

Zeng, F.-G., S. Rebscher, W. Harrison, X. Sun, and H. Feng (2008). Cochlear implants: System design, integration, and evaluation. *IEEE Reviews in Biomedical Engineering 1*, 115–142.

Zhang, H., Y. Wang, L. Wang, Y. Liu, H. Chen, and Z. Wu (2022). Process control monitor (PCM) for simultaneous determination of the piezoelectric coefficients d_{31} and d_{33} of AlN and AlScN thin films. *Micromachines 13*(4), 581.

Zhao, F., T. Koike, J. Wang, H. Sienz, and R. Meredith (2009). Finite element analysis of the middle ear transfer functions and related pathologies. *Medical Engineering & Physics 31*(8), 907–916.

Zhao, J., Y. Huang, X. Wen, S. Zhang, and P. Liu (2020). Identification of geometric parameters influencing the impedance sensitivity of piezoelectric mass sensors. *IEEE Sensors Journal 20*(24), 14740–14746.

Zheng, C., C. Xu, M. Wang, X. Li, and B. C. J. Moore (2023). Evaluation of deep marginal feedback cancellation for hearing aids using speech and music. *Trends in Hearing 27*.

Zheng, Z., C. Wang, L. Wang, Z. Ji, X. Song, P.-I. Mak, H. Liu, and Y. Wang (2024). Micro-electro-mechanical systems microphones: A brief review emphasizing recent advances in audible spectrum applications. *Micromachines 15*(3), 352.

Zilberman, Y. and J. H. Schulman (2003). Hearing aid system including speaker implanted in middle ear. U.S. Patent 6648813B2.

İlik, B., A. Koyuncuoğlu, O. Şardan Sukas, and H. Külah (2018). Thin film piezoelectric acoustic transducer for fully implantable cochlear implants. *Sensors and Actuators A: Physical 280*, 38–46.